ABSTRACT

Title of dissertation : SHADOW MOIRÉ USING NON-ZERO TALBOT DISTANCE AND APPLICATION OF DIFFRACTION THEORY TO MOIRÉ INTERFEROMETRY

Chang Woon Han, Doctor of Philosophy, 2005

Dissertation directed by: Associate Professor Bongtae Han

Department of Mechanical Engineering

When shadow moiré is practiced in industry for the warpage of microelectronic devices, the required high basic measurement sensitivity limits a dynamic range due to the diffraction effect of the reference grating. An extensive understanding of the contrast and intensity of shadow moiré fringes is required to achieve optical configurations for the measurements. In Part I, an exact mathematical description for the contrast and intensity of shadow moiré fringe is developed using a diffraction theory for a monochromatic light source first. The analysis is extended to study the effect of a broad spectrum light source on the contrast and intensity of shadow moiré fringes. The effect of an aperture on the fringe contrast is defined to propose a complete expression for the contrast of shadow moiré fringe. The mathematical

analysis is exploited to define the systematic error from the non-sinusoidal intensity distribution of shadow moiré fringe when the displacement resolution is enhanced using the phase-shifting technique. The results of the mathematical analysis provide a guideline for optimum optical configurations for the required basic measurement sensitivity, which results in a novel technique, called *high sensitivity shadow moiré using non-zero Talbot distance* (SM-NT). The SM-NT increases the dynamic range substantially and allows the warpage measurements of high-end microelectronics devices, which is not possible with the conventional shadow moiré using the zero Talbot distance.

In an achromatic moiré interferometry system, a compensator grating is translated to achieve phase-shifting. The phase-shifting in the achromatic system cannot be explained by the existing theories of moiré interferometry based on the concept of optical path length. In Part II, a diffraction theory is used to explain the phase shifting in the achromatic system. The results reveal that the amount of translation of the compensator grating is proportional to the diffraction order and the frequency of the compensator grating. The diffraction theory based the mathematical description is extended further to define the mini-order diffractions associated with a general deformations. The discrete Fourier transform is employed to characterize the mini-order from a generally deformed grating. The results explain that the magnitude of strain is only parameter to control the angle of mini-order.

SHADOW MOIRÉ USING NON-ZERO TALBOT DISTANCE AND APPLICATION OF DIFFRACTION THEORY TO MOIRÉ INTERFEROMETRY

By

Chang Woon Han

Dissertation submitted to the Faculty of the Graduate School of the
University of Maryland, College Park, in partial fulfillment
of the requirements for the degree of
Doctor of Philosophy
2005

Advisory Committee:
Associate Professor Bongtae Han, Chair
Professor Donald Barker
Professor Abhijit Dasgupta
Associate Professor Hugh Bruck
Associate Professor Georg Dolzmann

Dedication

This dissertation is gratefully dedicated to

my wife, Soojung,

without whose love, support, and patience, not a word would have been written.

Acknowledgements

First of all, I would like to express my sincere thanks to my advisor, Professor Bongtae Han, who accepted me as his Ph.D. student and offered me unlimited advice during the course of my Ph.D. The knowledge I have gained from him is invaluable and I could not have finished my dissertation successfully without his help. I would also like to extend my sincere appreciation to Professor Daniel Post of Virginia Tech for his inspirations to the problems I challenged in my thesis.

The members of my dissertation committee, Professors Donald B. Barker, Hugh Bruck, Abhijit Dasgupta, and Georg Dolzmann, have spared their time generously to help me improve the quality of my thesis. I thank them for their dedicated support.

My school years at University of Maryland cannot be a truly pleasant and memorable without all my friends here. I would like to convey my heartfelt thanks to them, although I can only mention a few here. Among them are Ari, Austin, Chris, Hongbo, John, Samson, Seungmin, Steve, Yang, and Yuri.

Table of Contents

List of Figures

Part I: Shadow Moiré Using Non-zero Talbot Distance

Chapter 1. Background and Motivation

1.1 Principle of Shadow Moiré

Since Meadows et al. and Takasaki proposed the moiré topography technique in 1970 [Meadows 1970, Takasaki 1970], shadow moiré has evolved as the moiré method most widely chosen for out-of-plane displacement measurements in the field of solid mechanics.

In the method, an amplitude-type reference grating is located in front of a specimen. The amplitude grating is comprised of linear opaque and transparent bars on a flat glass plate. As a light source illuminates the grating, the shadow of the reference grating behaves as a grating on the specimen. The observer sees the shadow grating and the superimposed reference grating, which interact to form moiré fringes.

Figure 1.1 illustrates the concept. A linear reference grating of pitch, g, is placed adjacent to a specimen surface. A light source illuminates the grating and the specimen at an angle α, and a camera receives light at an angle β, which is scattered in its direction by the specimen surface. The specimen surface is usually prepared by spraying it with a thin film of matte white paint for uniform diffusion.

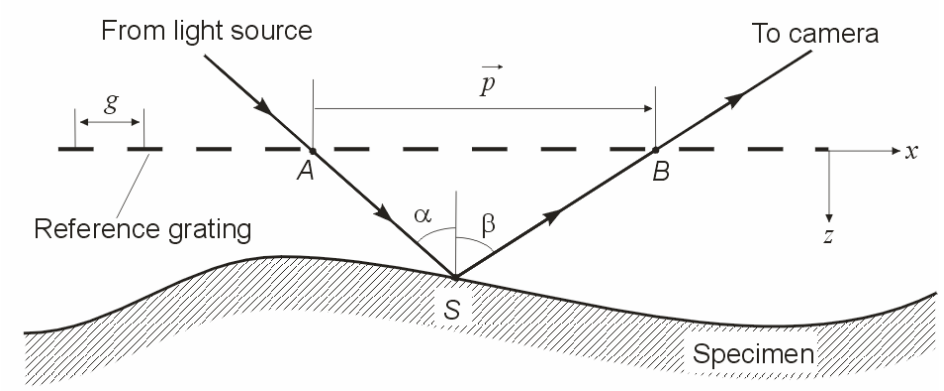

Figure 1.1 Illustration of rectilinear propagation of light in shadow moiré.

Referring to Fig. 1.1, a position vector $\vec{p}$ can be expressed as

$$\begin{aligned}\vec{p} &= \overrightarrow{AS} + \overrightarrow{SB} \\ &= \left[\left(z\tan\alpha\right)\vec{e_x} + z\vec{e_z}\right] + \left[\left(z\tan\beta\right)\vec{e_x} - z\vec{e_z}\right] \\ &= z\left(\tan\alpha + \tan\beta\right)\vec{e_x}\end{aligned} \tag{1.1}$$

where z is the variable gap between the grating and the specimen, $\vec{e_x}$ and $\vec{e_z}$ are the unit vectors in the x and z directions, respectively. The shadow image interacts with the reference grating to form the moiré pattern viewed by the camera. The fringe order N can be determined [Shield 1991] from the scalar product of the reference grating vector $\vec{G} = \frac{1}{g}\vec{e_x}$ and the position vector $\vec{p}$, which yields

$$N = \vec{G} \bullet \vec{p} = \frac{z}{g}\left(\tan\alpha + \tan\beta\right) \tag{1.2}$$

Equation 1.2 provides the relationship between z and fringe order N as

$$z(x,y) = \frac{g}{\tan\alpha + \tan\beta} N(x,y) \tag{1.3}$$

where z and N apply to each x, y point in the field.

Eq. 1.3 can provide constant sensitivity if $\tan\alpha + \tan\beta$ is constant. A shadow moiré scheme in Figure 1.2(a) achieves constant sensitivity by placing the light source and the observer at the same distance (L) away from the plane of the reference grating [Post 1994]. With this constraint,

$$\tan\alpha + \tan\beta = \frac{D}{L+z} \approx \frac{D}{L} = \text{constant} \tag{1.4}$$

Thus, the displacement is directly proportional to the moiré fringe order within the small displacement range.

The most practical configuration is shown in Fig. 1.2(b). An especially desirable feature of this configuration is normal viewing, which results in a distortion-free-view of the specimen. In the normal viewing, the governing equation of the shadow moiré is

$$z = \frac{g}{\tan\alpha} N \tag{1.5}$$

It should be noted that the governing equations of shadow moiré, or Eqs. 1.3 and 1.5, are based on an assumption of rectilinear propagation of light. The assumption is

reasonable only when the gap between the grating and the specimen is relatively small compared to the Talbot distance [Chiang 1989, Post 1994, Post 2000].

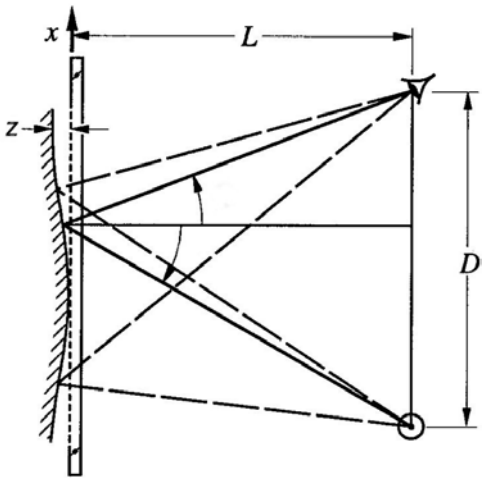

(a)

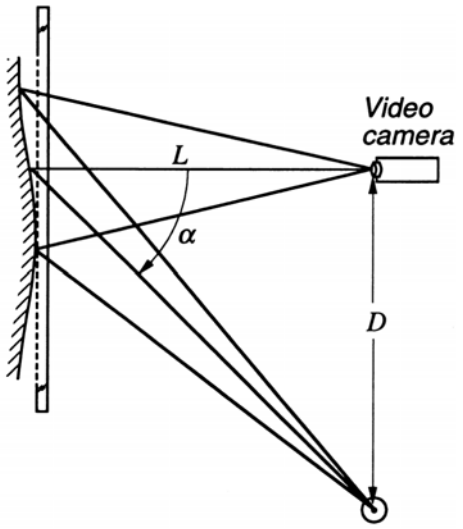

(b)

Figure 1.2 Shadow moiré arrangements in which $\tan\alpha + \tan\beta = \text{constant}$ [Post 1994].

1.2 Talbot Distance

Governing equations based on geometric optics, or Eqs. 1.3 and 1.5, imply that shadow moiré fringes are formed for any value of z. In fact, the contrast of the moiré fringe pattern varies with z, such that the pattern disappears and reappears cyclically as z increases. This is caused by the phenomenon known as the Talbot effect, also know as the grating self-imaging effect. The Talbot effect is a consequence of diffraction from a periodic structure. When an amplitude grating is illuminated by a monochromatic collimated light, the grating divides the light into a multiplicity of diffracted beams. At preferred distances from the grating, the interference of the diffracted beams produces alternating dark and bright bars, repeating with the same frequency as the grating. Talbot first observed this phenomenon, and the virtual grating was given a name, "Talbot images" [Talbot 1836].

Rayleigh derived the mathematical formula expressing the distance between the Talbot images of a linear grating in the case of a monochromatic plane wave normal illumination [Rayleigh 1881]. Consider a grating of pitch g illuminated by a monochromatic collimated light of wavelength λ. The Talbot, or self-imaging, distance at normal incidence D_T^0 is

$$D_T^0 = \frac{2g^2}{\lambda} \tag{1.6}$$

The intensity distribution of the shadow grating at planes located at the Talbot distance and the successive multiple of the Talbot distance is a duplicate of the intensity distribution of the reference grating, as illustrated in Figure 1.3. The intensity distributions at planes that lie at distance other than the Talbot distance are not identical to those of the reference grating.

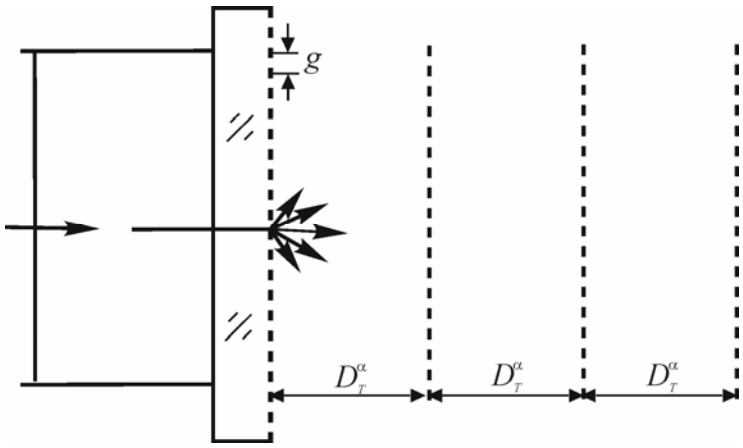

Figure 1.3 Illustration of virtual images being produced at Talbot distance and its multiple distances from a grating that is normally illuminated by a collimated beam of light [Post 1994].

It was also known [Post 1994] that the complementary image of the grating appears at a half distance of the Talbot distance and the images of the grating disappear at a quarter and three quarters of the Talbot distance. Figure 1.4 [Ackerman 2000] shows experimentally obtained Talbot images. The images were obtained for a linear grating, also known as Ronchi ruling, from a normal illumination with a light source of λ = 661 nm and the pitch of the grating was 0.1 mm. Figure 1.4(a) was captured on the surface of the grating glass. Figures 1.4(b) and (d) represent the images at

planes $D_T^0/4$ and $3D_T^0/4$, where the bright and dark bars of the projected grating disappeared. Figure 1.4(e) shows the image of the grating at the 1st Talbot plane. Figure 1.4 (c) represents the complimentary grating image located midway between Talbot planes.

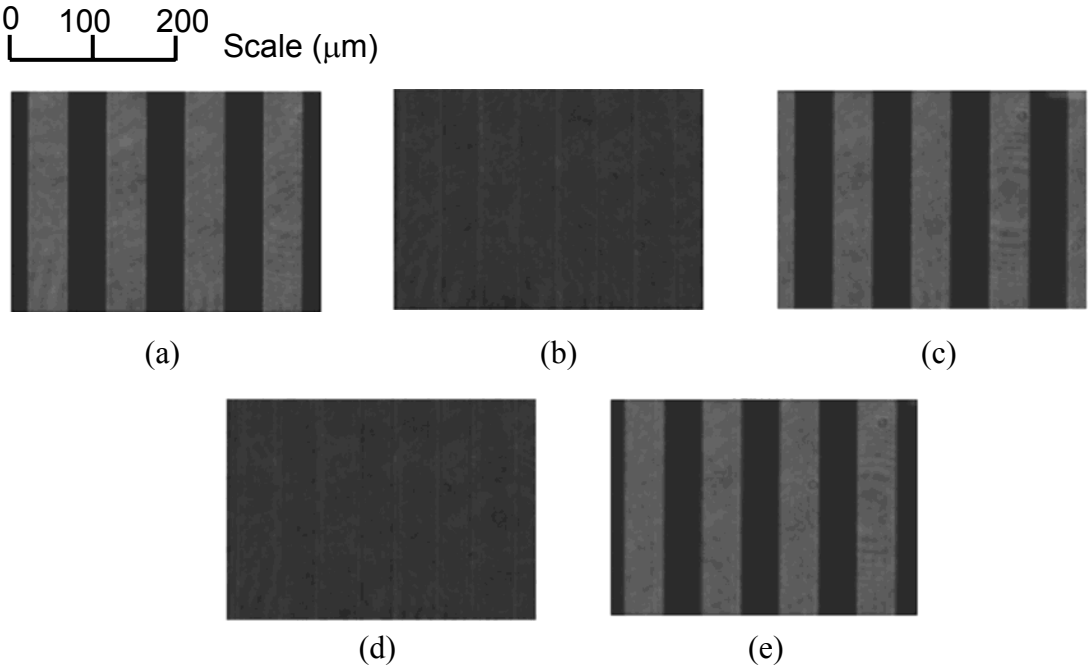

Figure 1.4 Talbot images of a Ronchi ruling for a normal illumination at z = (a) $0\,D_T^0$, (b) $1/4\,D_T^0$, (c) $1/2\,D_T^0$, (d) $3/4\,D_T^0$, and (e) $1\,D_T^0$ [Ackerman 2000].

Shadow moiré uses an oblique illumination instead of the normal illumination. The Talbot distance for the oblique illumination was determined by Testorf [Testorf 1996] and later verified experimentally by Ackerman [Ackerman 2000] as

$$D_T^{\alpha} = \frac{2g^2}{\lambda}\cos^3\alpha \tag{1.7}$$

when a grating is illuminated at incident angle α by a monochromatic collimated beam of wavelength λ, as illustrated in Fig. 1.5. In the same way of the normal illumination, the intensity at multiples of Talbot distance is a duplicate of the intensity distribution of the reference grating but shifted with amount of $\delta_x = z\tan\alpha$ in x-direction. The complimentary image of the grating appears at multiples of half the Talbot distance and the image of the grating disappear at a quarter and three quarters of the Talbot distance.

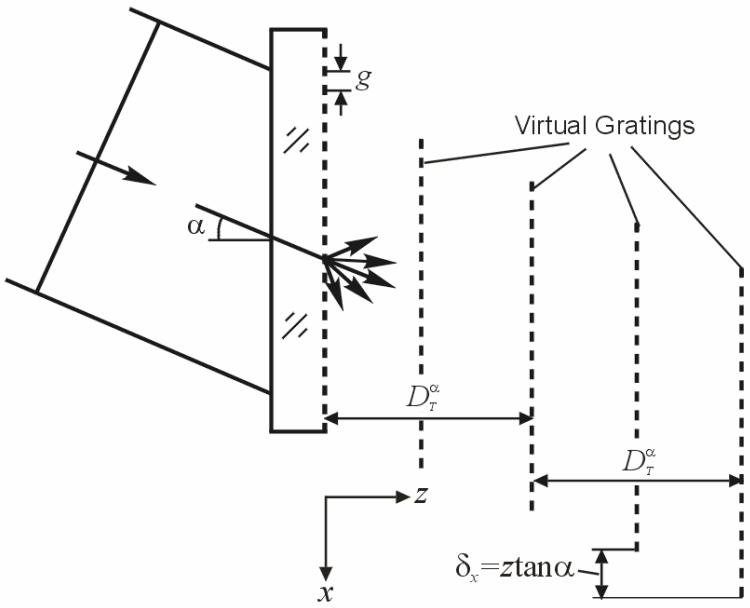

Figure 1.5 Illustration of Talbot distance for an oblique illumination and virtual gratings of optimum contrast formed at preferred distances.

1.3 Motivation

1.3.1 Conventional Application of Shadow Moiré

Conventional applications of shadow moiré include measurement of surface topography [Meadows 1970, Takasaki 1970, Yoshizawa 1993, Mauvosin 1994, Jin 2000], structure deformation from mechanical loading [Hahn 1992, Tuttle 1997 and 1999, Maji 2000], road inspection [Guralnick 1996], impact deformation [Kokidko 1997], and vibration mode [Hung 1977, Fujimoto 1982, Quan 2004, Tay 2004].

In the conventional practice of shadow moiré, relatively coarse gratings have been used. The pitch of grating used in those applications ranges from 0.5 to 2.0 mm and the corresponding Talbot distances, D_T^{α} , are 300 to 5000 mm. With these configurations, a specimen can be positioned readily within a small fraction of Talbot distance from the reference grating. Within the region, the assumption of rectilinear propagation of light is reasonable, and the virtual gratings and the corresponding shadow moiré fringes have reasonably high contrast. Some examples of the case are shown in Fig. 1.6. Fig. 1.6 (a) shows the shadow moiré fringe of a mannequin topography with the setup of a grating pitch of 1 mm and a contour interval of 4 mm per fringe, Fig. 1.6 (b) is for a scaled airplane model with the setup of a grating pitch of 1 mm and a contour interval of 5 mm per fringe, and Fig. 1.6 (c) shows the fringe of a buckled corrugated panel due to a mechanical loading with the setup of a grating pitch of 1.8 mm and a contour interval of 1 mm per fringe. In the figures, the dynamic range, which is defined as maximum deformation that shadow moiré can

measure with good contrast of fringe, varies from 10 to 120 mm. Generally, shadow moiré has a sufficient dynamic range in the conventional application.

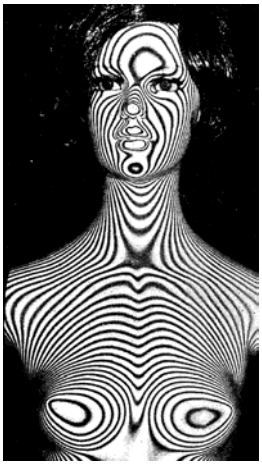

(a)

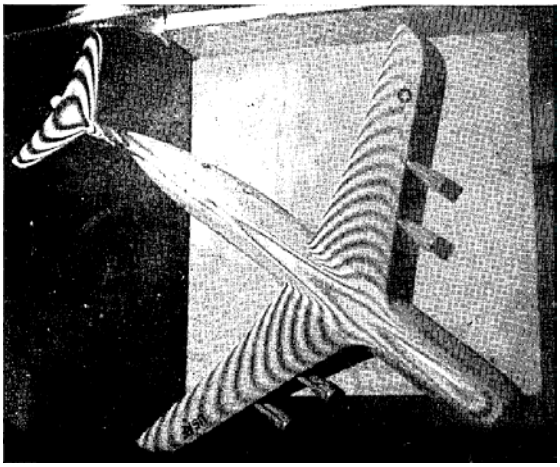

(b)

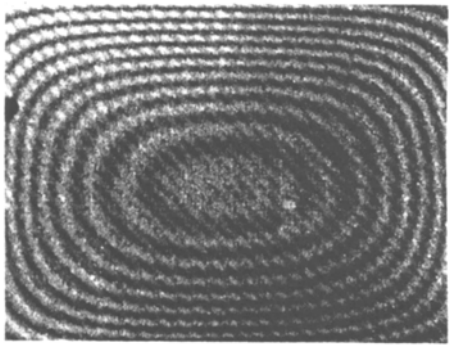

(c)

Figure 1.6 Examples of conventional application of shadow moiré; (a) topography of a mannequin [Takasaki 1990], (b) scaled airplane model [Meadows 1990], and (c) buckling of corrugated panel [Hahn 1992].

1.3.2 High Sensitivity Shadow Moiré and Limited Dynamic Range

Shadow moiré has been also employed widely for the measurement of warpage of microelectronic devices under thermal or mechanical loading [Yeh 1991 and 1993, Han 1993 a, Guo 1995, Stiteler 1996, Wang 1997, Rao 1997, Verma 1998, 1999, and 2001, Sutherlin 1998, Wu 1999, Petriccione 1999, Polsky 2000, Dang 2000, Dunne 2002, Vrinceanu 2002, Zhang 2003, Chen 2004, Zwemer 2004].

When shadow moiré is practiced in industry for the warpage of microelectronic devices, higher sensitivity is required because of its smaller deformation. For the higher sensitivity of shadow moiré, the reference grating with a finer pitch (25 μm to 200 μm) is employed. Because the Talbot distance is proportional to square of the grating pitch, as expressed in Eq. 1.7, the Talbot distance for the high sensitivity shadow moiré becomes much smaller than those used in the conventional applications. For example, for a shadow moiré setup with a contour interval of 50 μm per fringe, desirable parameters for normal viewing ($\beta = 0$) are g = 0.1 mm, tan $\alpha = 2$ (or $\alpha = 63.4°$) and $\lambda = 661$ nm, whereby Talbot distance is only 2.7 mm.

In such a case, it is difficult to have a sufficient dynamic range within a small fraction of Talbot distance from the reference grating. This condition becomes exacerbated when the method is employed to document thermally or mechanically induced warpage because a gap between the reference grating and the specimen should be provided to accommodate the deformations. Some examples of high sensitivity shadow moiré shown in Fig. 1.7 demonstrate the effect of the limited dynamic range

clearly. Figure 1.7 (a) shows the fringe pattern of a deformed plastic ball grid array (PBGA) package with the setup of a grating pitch of 40 μm and a contour interval of 40 μm per fringe and Fig. 1.7 (b) shows the fringe pattern of a deformed flip chip PBGA package with the setup of a grating pitch of 100 μm and a contour interval 50 μm per fringe. In the figures, the fringe disappears in some region due to the limited dynamic range of the high sensitivity shadow moiré caused by the Talbot effect. A new approach is required to obtain a sufficient dynamic range of high sensitivity shadow moiré.

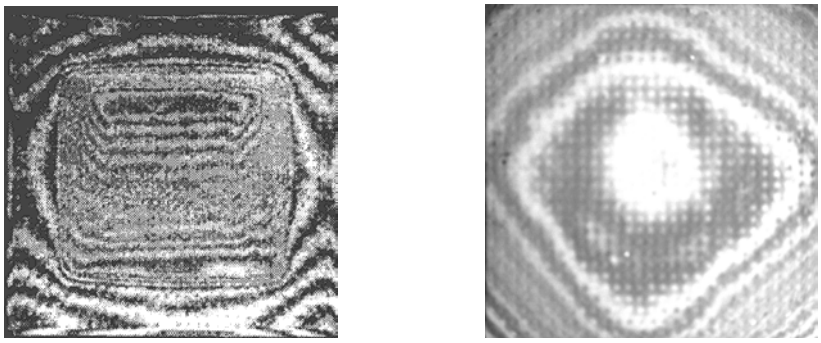

(a) (b)

Figure 1.7 Examples of high sensitivity shadow moiré on electronic packaging; (a) warpage of PBGA with g = 40 μm and Γ = 40 μm/fringe [Rao 1997] and (b) warpage of FC-PBGA with g = 100 μm and Γ = 50 μm/fringe.

1.3.3 Sensitivity Enhancement by Phase-shifting and Systematic Error

Phase-shifting technique is one of the most important techniques in interferometry. The method utilizes a series of phase-shifted patterns to determine fractional fringe orders. The method is based on harmonic representation of the intensity of fringe patterns [Creath 1988]. The harmonic intensity distribution can be defined as

$$I(x,y) = I_m(x,y) + I_a(x,y)\cos\left[\phi(x,y)\right] \tag{1.8}$$

where

$I_m(x,y)$: the mean intensity

$I_a(x,y)$: the modulation of interference fringe

$\phi(x,y)$: the angular phase information of the fringe pattern, and (x,y) represents all the points in the x-y plane of the object and the pattern; ϕ represents the fringe order N at each point of the pattern by $\phi(x,y) = 2\pi N(x,y)$ where N is a fringe order.

There are three unknowns in Eq. 1.8, namely I_m, I_a, ϕ. Three simultaneous equations are needed to evaluate the unknowns. Experimentally, the three equations can be obtained by recording a series of intensity distributions with a known amount of a uniform change of phase or fringe order. The three equations can be expressed as

$$
\begin{aligned}
I_1(x,y) &= I_m(x,y) + I_a(x,y)\cos\left[\phi(x,y) - \delta\right] \\
I_2(x,y) &= I_m(x,y) + I_a(x,y)\cos\left[\phi(x,y)\right] \\
I_3(x,y) &= I_m(x,y) + I_a(x,y)\cos\left[\phi(x,y) + \delta\right]
\end{aligned}
\tag{1.9}
$$

where I_i is the intensity distribution recorded with a phase change of $-\delta$, 0 , $+\delta$. Then the phase $\phi(x, y)$ can be determined as

$$
\phi(x,y) = \arctan\left[\frac{1-\cos\delta}{\sin\delta}\cdot\frac{I_1(x,y) - I_3(x,y)}{2I_2(x,y) - I_1(x,y) - I_3(x,y)}\right] \tag{1.10}
$$

For a more accurate phase calculation, other algorithms using more than three phase-shifted images have been developed. The most widely used algorithm uses four phase-shifted images [Wang 2003]. The set of four images are

$$
\begin{aligned}
I_1(x,y) &= I_m(x,y) + I_a(x,y)\cos\left[\phi(x,y)\right] \\
I_2(x,y) &= I_m(x,y) + I_a(x,y)\cos\left[\phi(x,y) + \pi/2\right] \\
I_3(x,y) &= I_m(x,y) + I_a(x,y)\cos\left[\phi(x,y) + \pi\right] \\
I_4(x,y) &= I_m(x,y) + I_a(x,y)\cos\left[\phi(x,y) + 3\pi/2\right]
\end{aligned}
\tag{1.11}
$$

The phase at each point can be expressed in a simpler form as

$$
\phi(x,y) = \arctan\left[\frac{I_4(x,y) - I_2(x,y)}{I_1(x,y) - I_3(x,y)}\right] \tag{1.12}
$$

The phase-shifting method has been applied to shadow moiré to increase its sensitivity by numerous researchers [Liao 1993, Wang 1997, Petriccione 1999, Wu 1999, Polsky 2000, Dang 2000, Dunne 2002, Vrinceanu 2002, Zhang 2003, Chen 2004, Zwemer 2004]. Although it was realized that shadow moiré fringes have a complex intensity distribution, it was assumed in all the studies that shadow moiré fringes have a sinusoidal intensity distribution. This assumption was inevitable to employ the existing phase-shifting algorithms. The theoretical enhancement of measurement sensitivity was reported but a true net gain in measurement sensitivity was not discussed. The errors induced by the sinusoidal assumption can be substantial and can offset the sensitivity enhancement offered by the phase-shifting technique.

The systematic error associated with the non-sinusoidal intensity distribution is demonstrated with two different basic measurement sensitivities. The specimen was a 25 mm circular plano-convex lens with a focal length of 750 mm. The concave surface was painted with a white matt paint and the surface was measured by shadow moiré. The results are shown in Figs. 1.8 and 1.9 for the contour intervals of 100 and 500 μm per fringe, respectively. The four phase-shifted patterns are shown in (a)-(d) and the measured displacements are compared with the exact values of the lens geometry along the horizontal center line (AA') in (e).

For the case of the higher measurement sensitivity (Fig. 1.8), the measured values mach well with the exact values. When a much lower measurement sensitivity is used (Fig. 1.9), however, a significant error is produced; the amount of the error is

approximately 10 μm. The error was caused by the non-sinusoidal intensity distribution and it would depend on the configuration of shadow moiré.

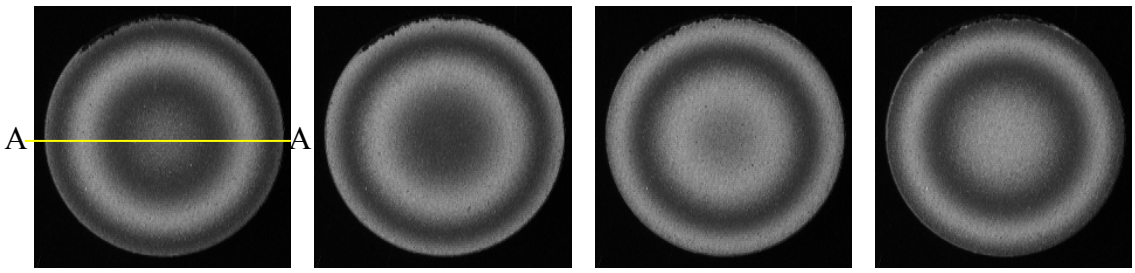

(a) (b) (c) (d)

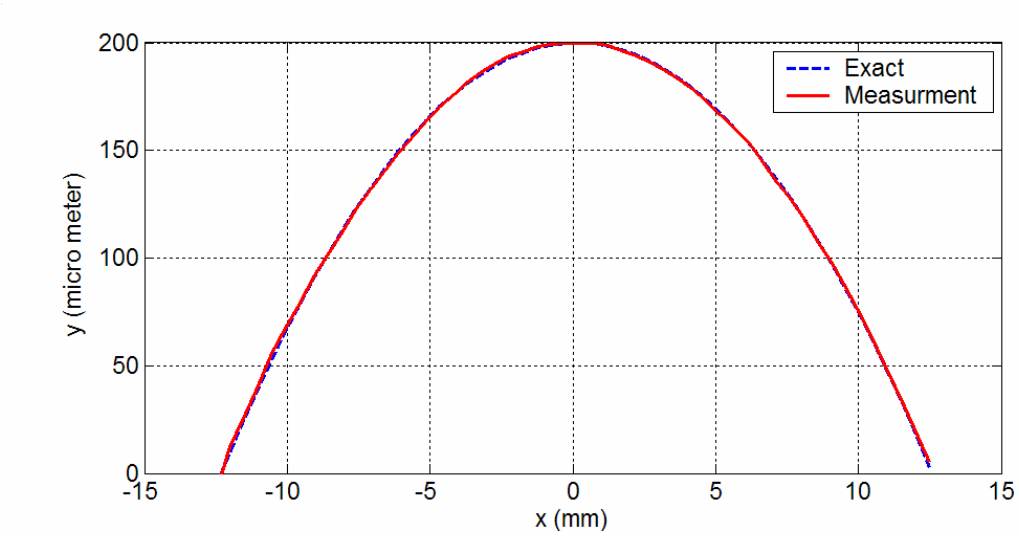

(e)

Figure 1.8 Result of phase-shifting shadow moiré with a high measurement sensitivity (Γ = 100 μm /fringe); fringe patterns with phase-shifting amount of (a) 0, (b) $\pi/4$, (c) $\pi/2$, (d) $3\pi/4$, and (e) the results are compared with the exact geometry.

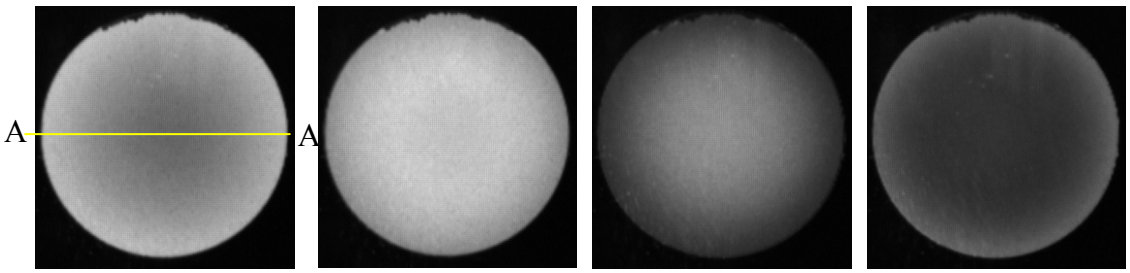

(a) (b) (c) (d)

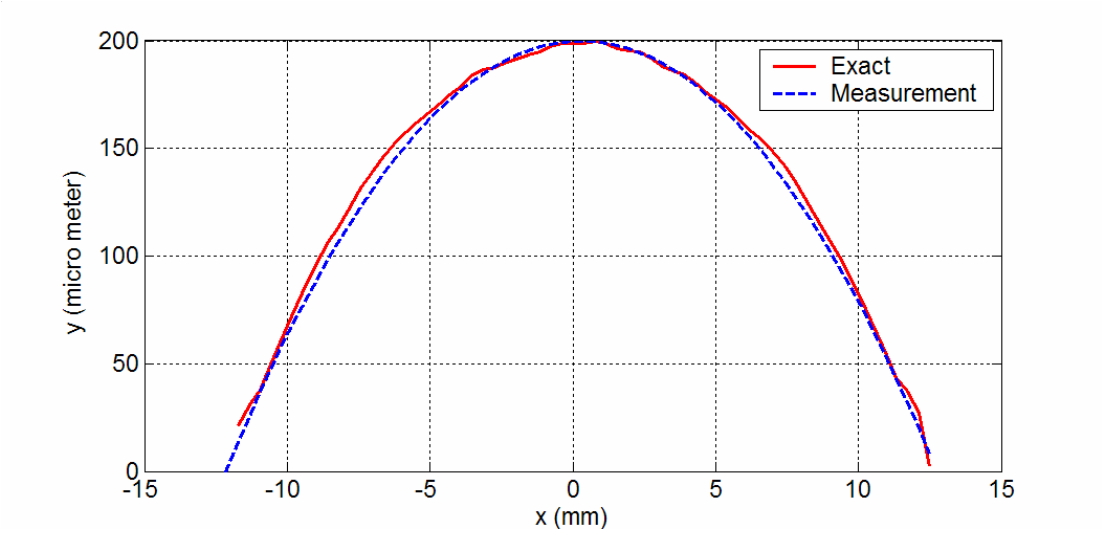

(e)

Figure 1.9 Result of phase-shifting shadow moiré with a low measurement sensitivity (Γ = 500 μm /fringe); fringe patterns with phase-shifting amount of (a) 0, (b) $\pi/4$, (c) $\pi/2$, (d) $3\pi/4$, and (e) the results are compared with the exact geometry.

The enhancement of measurement sensitivity by combining the phase-shifting with shadow moiré requires the extensive analysis for the fringe intensity distribution of shadow moiré. Arai et al. [Arai 1999] attempted to negate the effect of the sinusoidal assumption by considering the first and second order harmonic functions obtained

form the experimental results. The results cannot be generalized for shadow moiré since the intensity distribution is a function of several experimental parameters. Asundi et al. [Asundi 1994] also attempted to calculate the errors associated the sinusoidal assumption using triangular, square and step-triangular wave intensity profiles. The intensity profiles do not represent the true shadow moiré fringes and the results can be misleading.

1.3.4 Problem Statement

High measurement sensitivity is required for the application of shadow moiré to warpage measurement of microelectronic devices. It can be achieved by either increasing the basic measurement sensitivity or employing the phase-shifting technique. However, the upper limit of the basic sensitivity is limited by the diffraction effect and the phase-shifting technique is limited by the non-sinusoidal intensity distribution of shadow moiré fringes.

In this study, I propose to utilize the non-zero Talbot distance to achieve the large dynamic range as well as high precision. An attempt to measure warpage using the Talbot effect in shadow moiré was reported in the literature [Wei 1998], but the effect of inclined illumination and diffraction was not realized correctly and the suggested optical configuration was misleading. The design of experiments for effective measurements at the non-zero Talbot distance requires detailed knowledge of fringe intensity and contrast as a function of the distance between the specimen and the reference grating. Understanding the diffraction effect in shadow moiré becomes

essential for developing the fringe intensity function and optimizing the experimental results.

The objective of part I is to provide a theoretical framework for shadow moiré with non-zero Talbot distance, to suggest a high sensitivity shadow moiré with non-zero Talbot distance, and to propose an optimal optical configurations of the system for the best fringe contrast. The specific scope includes:

1) Study the effect of diffraction on the intensity distribution and contrast of shadow moiré fringe for a monochromatic light source.
2) Develop a complete expression for the contrast of shadow moiré fringes including the geometrical effect.
3) Investigate the effect of a broad spectrum light source on the intensity distribution and contrast of shadow moiré fringes.
4) Investigate the effect of non-sinusoidal shadow moiré fringe on the result of phase-shifting.
5) Suggest and implement the shadow moiré using non-zero Talbot distance.
6) Propose optical configurations for optimum fringe contrast for a given basic measurement sensitivity.

Chapter 2. Diffraction Effect on Shadow Moiré Fringe

2.1 Governing Equation of Shadow Moiré from Diffraction Theory

Using the approach of angular spectrum of plane waves [Edgar 1969], the complex field, E, of the light at a distance z from the grating can be expressed as [Patroski 1989]

$$E(x,z) = \sum_{n=-\infty}^{\infty} a_n \exp\left\{ i \frac{2\pi}{\lambda} \left[x \sin\theta_n + z \cos\theta_n \right] \right\} \tag{2.1}$$

where $\sin\theta_n = n\frac{\lambda}{g} + \sin\alpha$, and n is diffraction order 0, 1, 2, 3, ---. (2.2)

Using the following parabolic approximation which is prevalent in the literature [Testorf 1996, Edgar 1969, Patroski 1989, Keren 1985]

$$\cos\theta_{\mathrm{n}} \approx \cos\alpha \left[1 - \frac{1}{2} \left\{ \left(\frac{\mathrm{n}\lambda}{\mathrm{g}\cos\alpha} \right)^2 + 2 \frac{\mathrm{n}\lambda}{\mathrm{g}} \frac{\sin\alpha}{\cos^2\alpha} \right\} \right] \tag{2.3}$$

the approximated complex field E_p can be expressed in terms of the Talbot distance (Eq. 1.7) as

$$E(x,z) \approx E_p(x,z) = \exp\left\{ i\frac{2\pi}{\lambda}\left(x\sin\alpha + z\cos\alpha\right)\right\} * \sum_{n=-\infty}^{\infty} a_n \exp\left\{ i2\pi\left(\frac{n}{g}x - \frac{n}{g}z\tan\alpha - \frac{n^2}{D_T^{\alpha}}z\right)\right\} \tag{2.4}$$

The corresponding intensity distribution of the Talbot image I_p can be expressed as

$$I_p(x,z) = E_p(x,z)\cdot\overline{E_p(x,z)} = \sum_{n=-\infty}^{\infty}\sum_{m=-\infty}^{\infty} a_n a_m \exp\left\{ i2\pi(n-m)\frac{x - z\tan\alpha}{g}\right\}\exp\left\{ i2\pi\left(\frac{m^2-n^2}{D_T^{\alpha}}z\right)\right\} \tag{2.5}$$

It is worth noting that the intensity distribution of the Talbot image consists of two terms: for a given α, g and λ, the first term $\left(\frac{x - z\tan\alpha}{g}\right)$ (referred to as the "rectilinear term") is a function of x and z, while the second term $\left(\frac{m^2-n^2}{D_T^{\alpha}}z\right)$ (referred to as the "diffraction term") is a function of only z. The rectilinear term defines the measurement sensitivity while the diffraction term controls the fringe contrast. Equation 2.5 was evaluated numerically for an amplitude grating with the equal widths of bars and spaces. The results are plotted in Fig. 2.1a. The rectilinear term in Eq. 2.5 was also calculated and the results are plotted in Fig. 2.1b. As the gap z increases, the Talbot image of the grating (i. e., the shadow of the grating) translates in the x direction by $z\tan\alpha$ due to the rectilinear term; if z increases by a fraction of $\frac{g}{\tan\alpha}$, the Talbot image translates by the same fraction of g. The diffraction term does not contribute to the translation of the Talbot image. Instead, it distorts the

intensity distribution of the Talbot image, which alters the intensity distribution of shadow moiré fringes. It is to be noted that the complimentary image in Fig. 1.4 (c) is not a shifted image by the rectilinear term. Instead, it is an image altered by the diffraction term.

Referring again to Fig. 1.1, the specimen surface scatters light in all directions but only light that propagates rectilinearly can enter the camera. An additional lateral shift of the Talbot image caused by the oblique viewing is $z\tan\beta$. The total lateral shift of the Talbot image that is seen by an observer then becomes $z\left(\tan\alpha+\tan\beta\right)$. The total lateral shift is directly related to the fringe order *N* by

$$z(x,y)\left(\tan\alpha\ +\ \tan\beta\right)=gN(x,y) \tag{2.6}$$

, which is identical to the governing equation based on rectilinear propagation of light (Eq. 1.3).

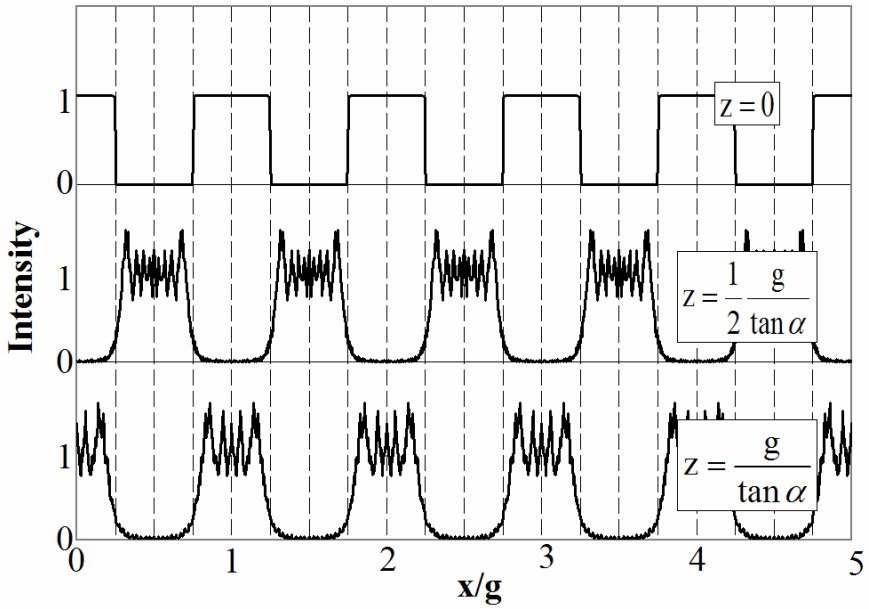

(a)

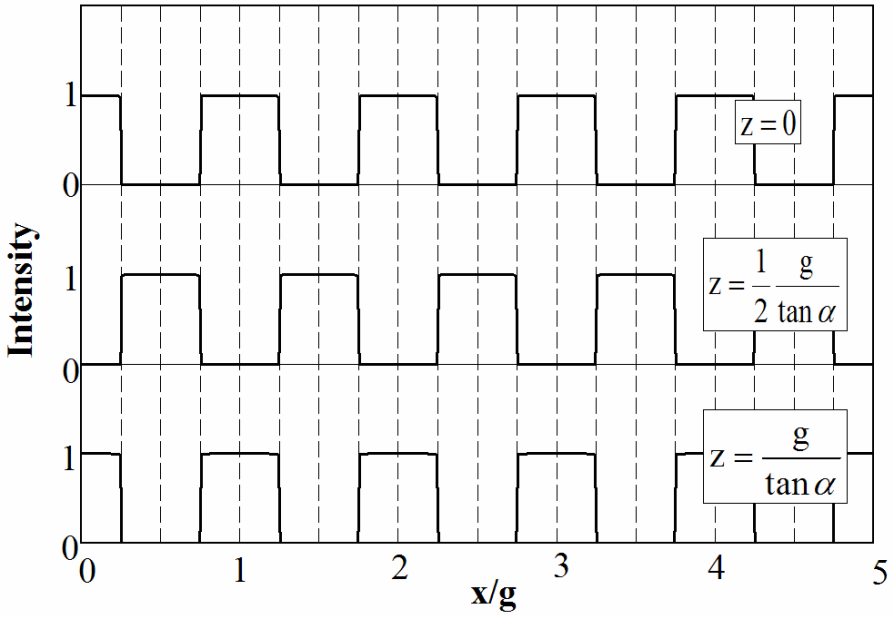

(b)

Figure 2.1 Intensity distribution of self-image of grating obtained from Eq. 2.5; (a) rectilinear and diffraction term, (b) rectilinear term only.

2.2 Intensity Distribution of Shadow Moiré Fringe

In the previous section, a parabolic approximation (Eq. 2.3) was used to derive the intensity distribution of Talbot images (Eq. 2.5). Although it offers a physical insight for shadow moiré based on the diffraction theory, the aberration of the intensity distribution is not negligible for large incident angles[*]. The exact intensity distribution $I(x,z)$ of a Talbot image is required for an accurate expression of fringe contrast.

From Eq. 2.1, the exact complex field can be written as

$$\begin{aligned} E(x,z) &= \sum_n a_n \exp\left(i\frac{2\pi}{\lambda} x \sin\theta_n \right) \exp\left(i\frac{2\pi}{\lambda} z \cos\theta_n \right) \\ &= \sum_n a_n \exp\left\{ i\frac{2\pi}{\lambda} x \left(\frac{n\lambda}{g} + \sin\alpha \right) \right\} \times \\ &\qquad \exp\left\{ i\frac{2\pi}{\lambda} z \cos\alpha \sqrt{1 - 2\frac{n\lambda}{g}\frac{\sin\alpha}{\cos^2\alpha} - \left(\frac{n\lambda}{g}\right)^2 \frac{1}{\cos^2\alpha}} \right\} \end{aligned} \tag{2.7}$$

and the exact intensity distribution of a Talbot image can be expressed as

[*] The effect of parabolic approximation in inclined illumination will be discussed in a later section.

$$
\begin{aligned}
I(x,z) &= E(x,z)\cdot\overline{E(x,z)} \\
&= \sum_n\sum_m a_n a_m \exp\left(i\frac{2\pi}{\lambda}x\left(\sin\theta_n-\sin\theta_m\right)\right)\exp\left(i\frac{2\pi}{\lambda}z\left(\cos\theta_n-\cos\theta_m\right)\right) \\
&= \sum_n\sum_m a_n a_m \exp\left\{i\frac{2\pi}{g}x\left(n-m\right)\right\}\times \\
&\qquad \exp\left\{i\frac{2\pi}{\lambda}z\cos\alpha\sqrt{1-2\frac{n\lambda}{g}\frac{\sin\alpha}{\cos^2\alpha}-\left(\frac{n\lambda}{g}\right)^2\frac{1}{\cos^2\alpha}}\right. \\
&\qquad \left.-\sqrt{1-2\frac{m\lambda}{g}\frac{\sin\alpha}{\cos^2\alpha}-\left(\frac{m\lambda}{g}\right)^2\frac{1}{\cos^2\alpha}}\right\}
\end{aligned}
\tag{2.8}
$$

The self-image described by Eq. 2.8 interacts with the reference grating to form shadow moiré fringes. Because of the diffraction term, the intensity distribution of shadow moiré does not produce the usual triangular distribution of geometric moiré fringes. The following analysis is given to determine the intensity distribution of shadow moiré fringes.

Assuming an imaging system with an extremely tiny aperture[*], the intensity distribution of shadow moiré fringes, I_s, can be determined by superposing a Talbot image on a reference grating; mathematically, using Eq. 2.8, I_s can be expressed as [Keren 1985]

[*] A finite aperture alters the contrast of shadow moiré fringes significantly and this effect will be addressed in a later chapter.

$$I_s(z) = \frac{1}{g}\int_{-g/2}^{g/2} \{I(x,0)I(x,z)\}dx \tag{2.9}$$

The intensity distributions for a normalized gap with Talbot distance are plotted in Fig. 2.2, where α is 45° and g is (a) 0.1 mm, (b) 0.05 mm and (c) 0.025 mm, respectively. As expected from Fig. 1.4, the intensity becomes zero at $z = D_T^{\alpha}/4$ and it returns to its maximum value at $z = D_T^{\alpha}/2$. The intensity distribution will repeat as z increases.

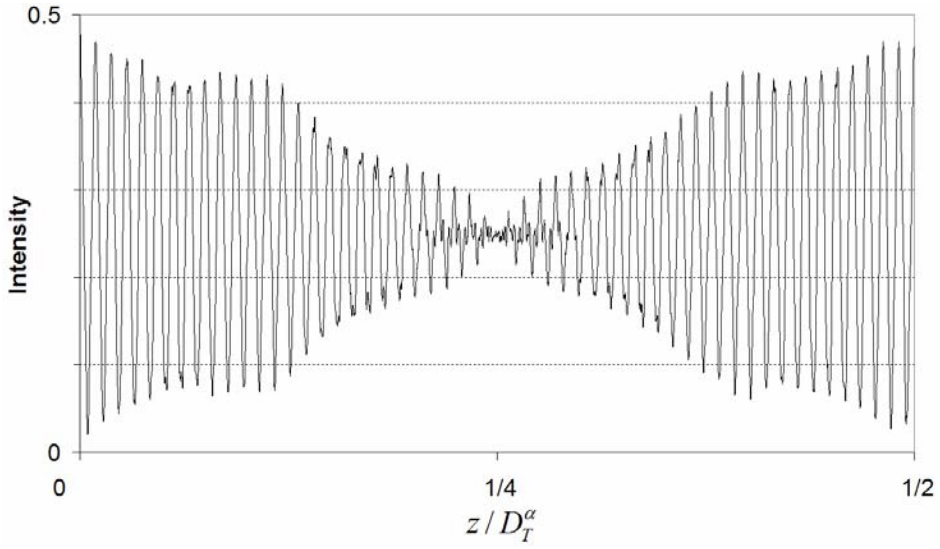

(a)

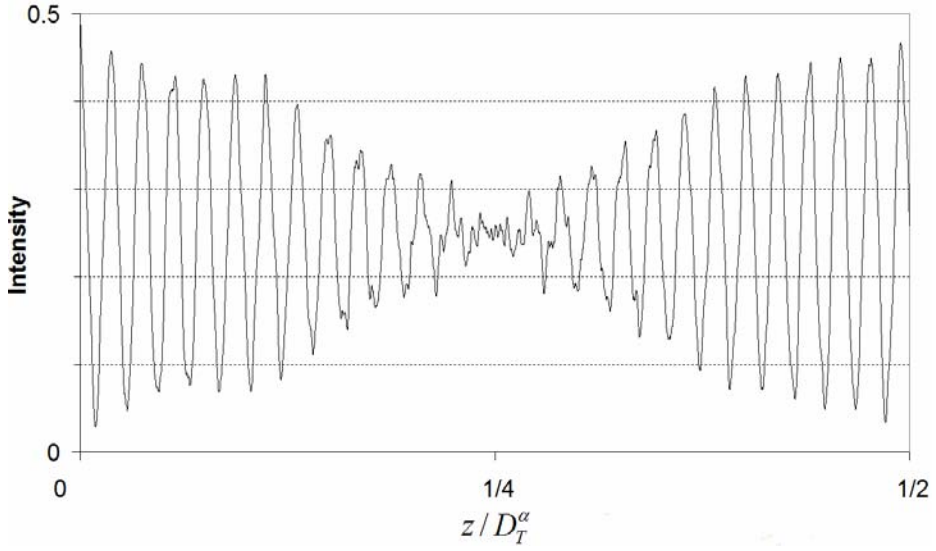

(b)

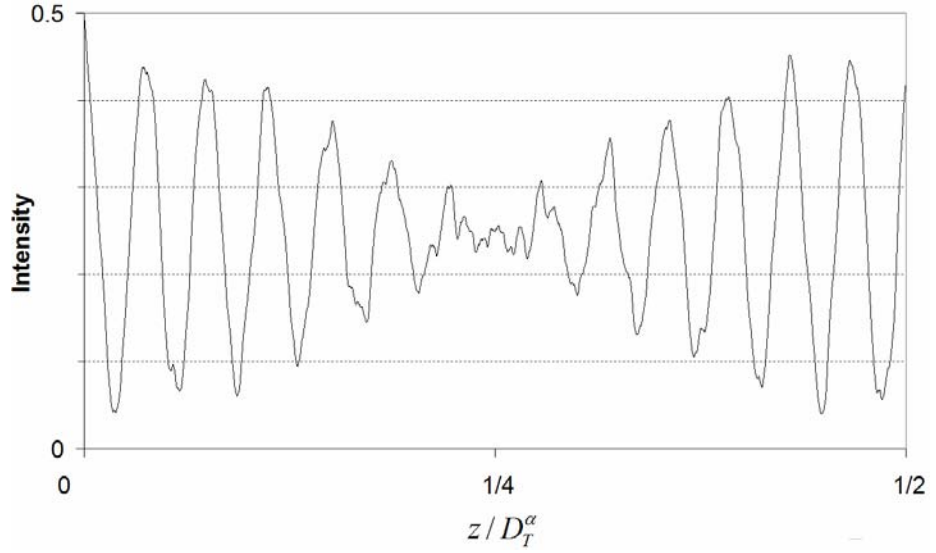

(c)

Figure 2.2 Theoretical intensity distributions of shadow moiré fringes with $\alpha = 45°$, λ = 661 nm, and g = (a) 0.1mm, (b) 0.05 mm, and (c) 0.025 mm.

2.3 Diffraction Effect on Fringe Contrast

The contrast cannot be determined directly from Fig. 2.2 because the intensity changes continuously with z. The maximum intensity and the minimum intensity of a shadow moiré fringe at a given distance z can be calculated numerically by altering Eq. 2.9. Considering that the Talbot image translates by $z\tan\alpha$, the maximum and minimum intensity at z can be expressed as

$$\begin{aligned} I_s^{\max}(z) &= \frac{1}{g}\int_{-g/2}^{g/2}\left\{I(x,0)I(x+z\tan\alpha,z)\right\}dx \\ I_s^{\min}(z) &= \frac{1}{g}\int_{-g/2}^{g/2}\left\{I(x,0)I(x+z\tan\alpha+\frac{g}{2},z)\right\}dx \end{aligned} \tag{2.10}$$

Then the contrast due to the Talbot effect C_T, which will be referred to as *Talbot contrast*, can be defined as

$$C_T(z) = \frac{I_s^{\max}(z) - I_s^{\min}(z)}{I_s^{\max}(z) + I_s^{\min}(z)} \tag{2.11}$$

Figure 2.3 shows the theoretical contrast in case of g = 0.1, 0.05, and 0.025 mm with α = 45° and λ = 661 nm. The contrast changes periodically with the normalized Talbot distance. The distribution also changes with the pitch of the grating. It is important to note that the contrast at multiples of half the Talbot distance does not return to its maximum value of "1". This is distinctively different from the results obtained for normal illumination, where the contrast at multiples of half the Talbot distance always has its maximum value of "1" regardless of z [Keren 1985].

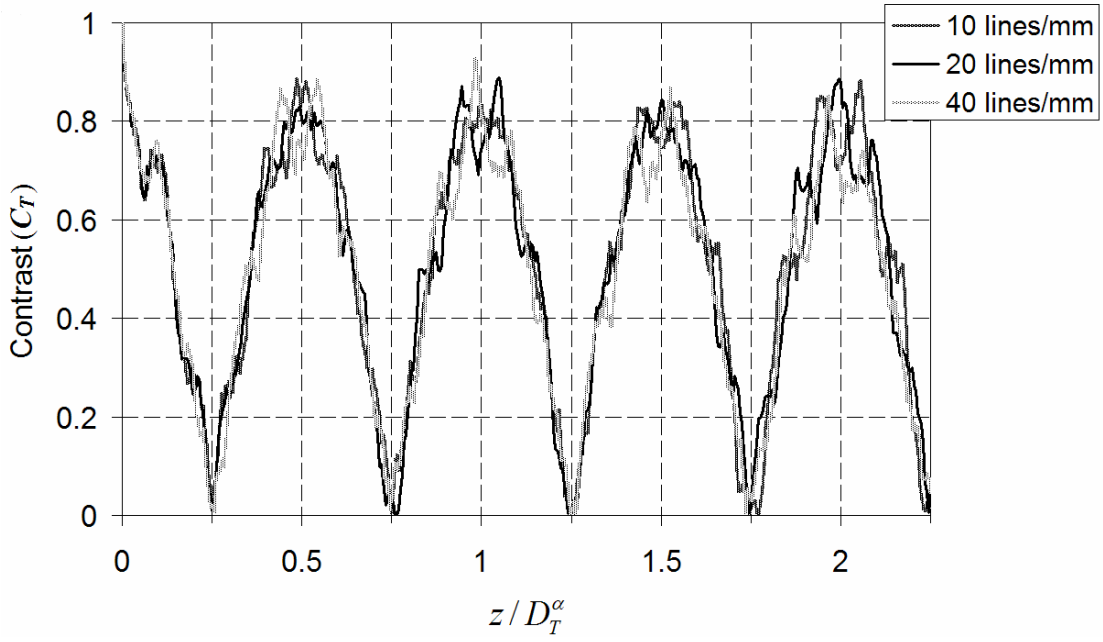

Figure 2.3 Talbot contrast of shadow moiré fringe; $\alpha = 45°$ and $\lambda = 661$ nm.

2.4 Experiment Validation of Talbot Contrast

An experiment was conducted to verify the validity of Eq. 2.11. The experimental setup is illustrated schematically in Fig. 2.3. A light source of laser diode (λ = 661 nm) was employed as a light source. The angle of incidence was 45° and the reference grating (Grating 1) was a Ronchi grating with pitch of 0.1 mm.

In the setup, another Ronchi grating with the same pitch referred to as Grating 2 was inserted parallel to Grating 1. A ground glass was attached to Grating 2 for viewing in such a way that the ground surface was in contact with the grating plane of Grating 2. The camera was focused on the contact plane, where the Talbot image of Grating 1 and Grating 2 form a fringe pattern. The distance between two gratings was adjusted by using a micrometer stage.

If Gratings 1 and 2 were exactly parallel to each other, the intensity seen by the camera would be uniform. Grating 2 was rotated slightly with respect to the z axis to produce a fringe pattern with rotational mismatch. Then fringe patterns were recorded at discrete intervals of z.

This setup offers two important features. First, the setup negates the effect of aperture completely so that only the Talbot effect can be documented. This is critical to a direct comparison of the experimental results with the theoretical prediction that assumes a theoretical pinhole aperture. Another important feature is that the fringes, equivalent to shadow moiré fringes, can be formed by rotational mismatch.

Consequently, the maximum and minimum intensity can be determined simultaneously at a given distance z, which makes the contrast calculation easier and more accurate. Representative fringe patterns obtained from the setup are shown in Fig. 2.5. The maximum and minimum intensities were determined digitally from the patterns and the contrast was calculated using Eq. 2.11.

The experimental results are plotted in Fig. 2.6, where the contrasts obtained from the experiment are compared with the theoretical (or predicted) values. It is to be noted that the contrast near $z = 0$ could not be measured because of the finite thickness of Grating 2. The experimental data match the predicted values extremely well, which corroborates the validity the theoretical relationships.

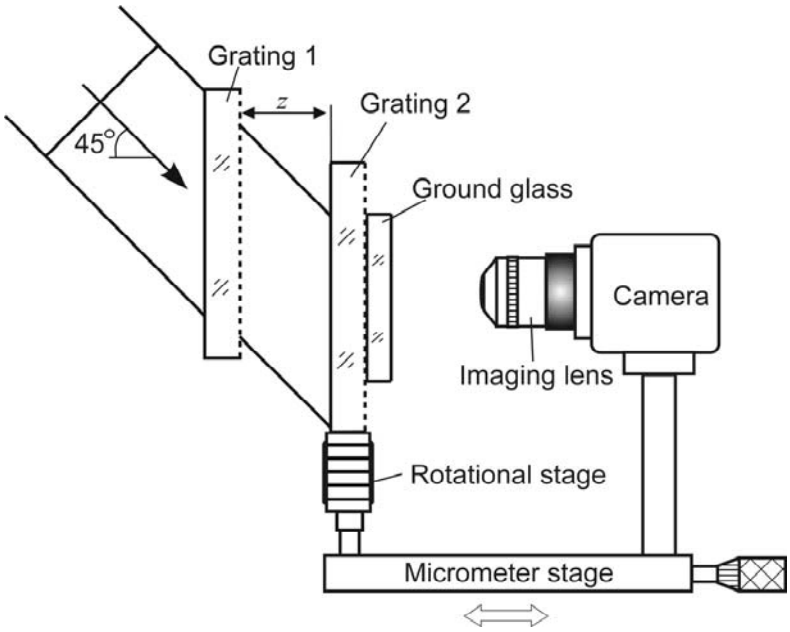

Figure 2.4 Experimental setup to measure the Talbot contrast of shadow moiré fringes.

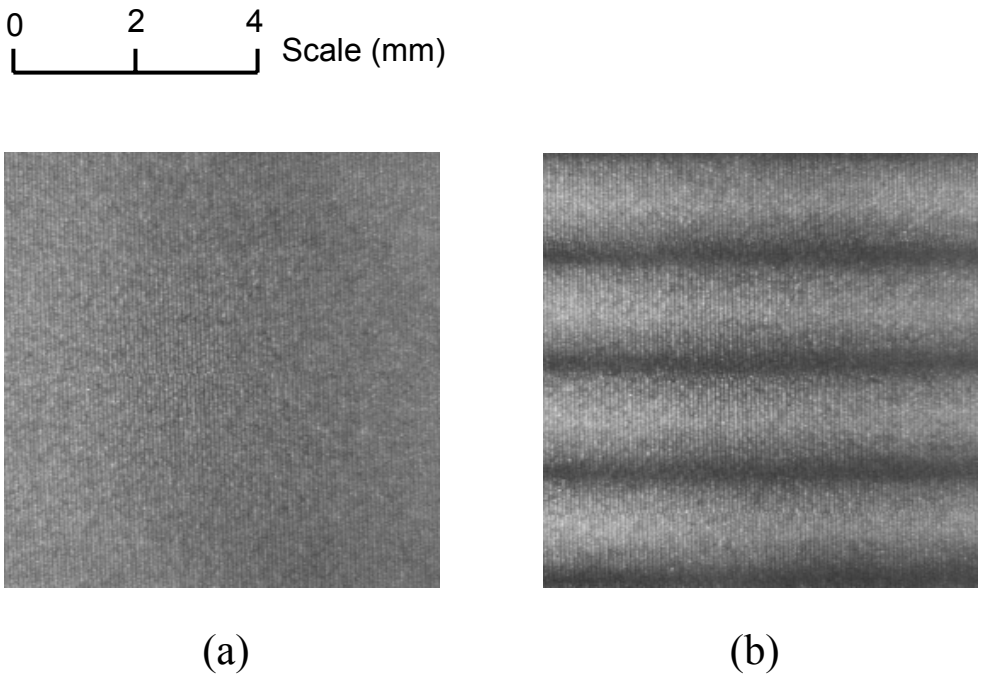

Figure 2.5 Fringe patterns with rotational mismatch at (a) $z = 0.25D_T^{\alpha}$ and (b) $z = 0.5D_T^{\alpha}$.

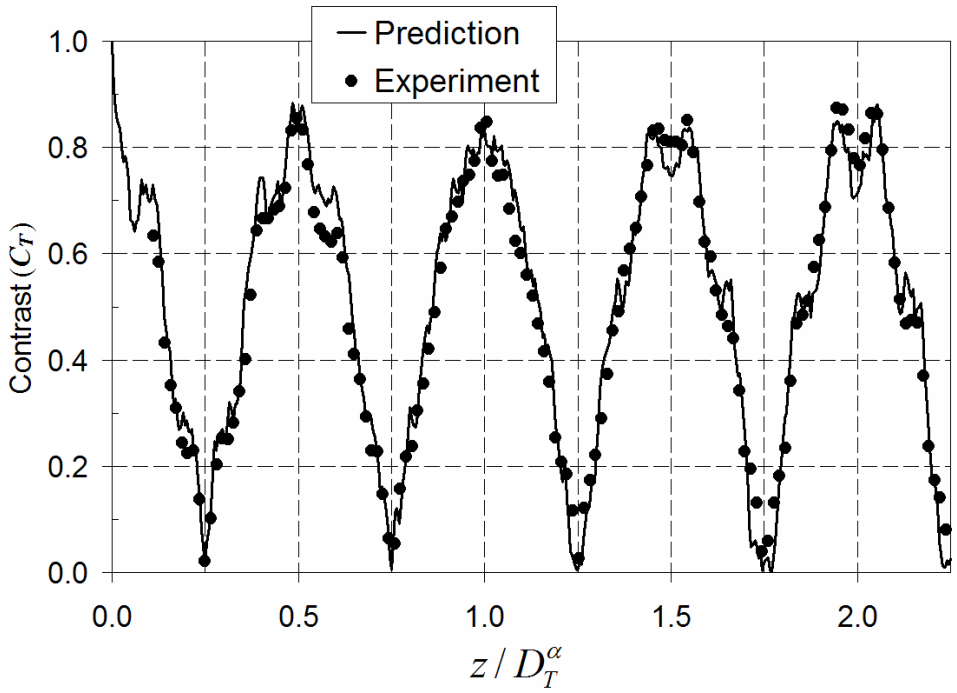

Figure 2.6 Experimental results of the Talbot contrast are compared with theoretical prediction.

2.5 Effect of Parabolic Approximation on the Contrast

The parabolic approximation used to derive Eq. 2.3 is reasonable when the angle of incidence is small. The amount of aberration becomes significant as the angle increases. The large aberration can alter the contrast significantly.

The contrast of shadow moiré fringes was calculated by Eq. 2.11 using the approximated intensity (Eq. 2.5) first and it was compared with a subsequent calculation using the exact intensity (Eq. 2.8). The contrast for incident angles of 0° (normal incidence) and 45° are plotted in Fig. 2.7, where the results obtained from Eqs. 2.5 and 2.8 are denoted by *approx.* and *exact*, respectively. Other parameters used in the calculation are $g = 0.1$ mm and $\lambda = 661$ nm.

For normal illumination, the approximated contrast is nearly identical to the exact contrast (Fig. 2.7 (a)); aberrations from the parabolic approximation are negligible. However, for the inclined illumination ($\alpha = 45°$), the eact contrast is distinctively different from the approximated contrast (Fig. 2.7 (b)). The shape and maximum value of the exact contrast for inclined illumination change as z increases. More important, the exact contrast for inclined illumination at multiples of half the Talbot distance does not return to its maximum value attained at $z = 0$.

The intensity distribution of Talbot images explains the discrepancy. Figure 2.8 shows the intensity distributions at the half and full Talbot distances for inclined illumination ($\alpha = 45°$). Solid lines and dashed lines in the figure are calculated from

Eqs. 2.8 and 2.5, respectively. The intensity distribution obtained from the parabolic approximation (Eq. 2.5) is identical to the intensity distribution of the reference grating. However, the exact intensity distributions obtained from Eq. 2.8 are irregular. The non-zero intensity in dark bars (x/g = 0 to 0.5) contributes to a decrease in the maximum contrast at multiples of half the Talbot distance.

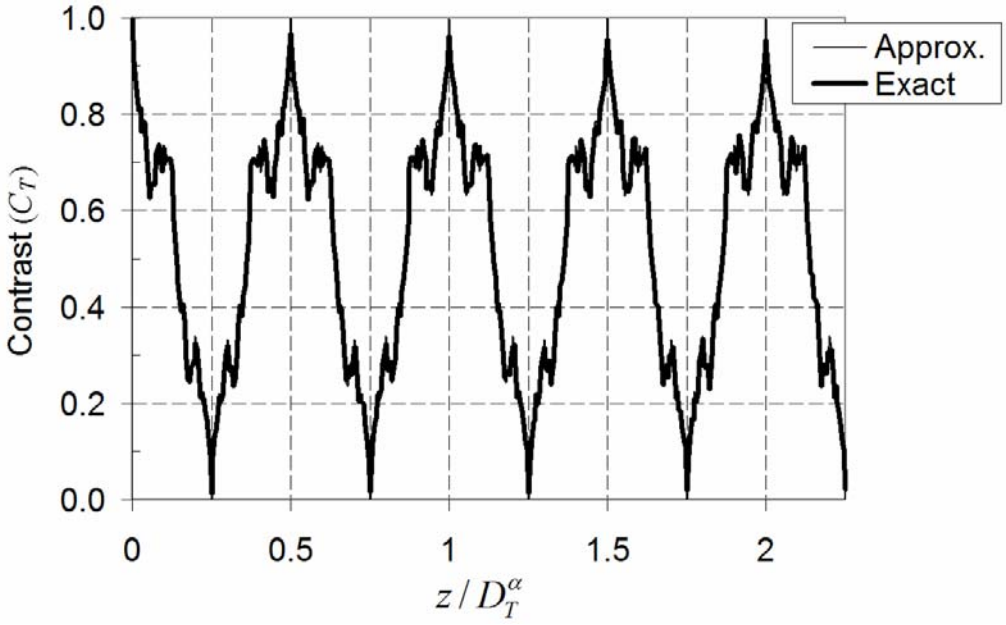

(a)

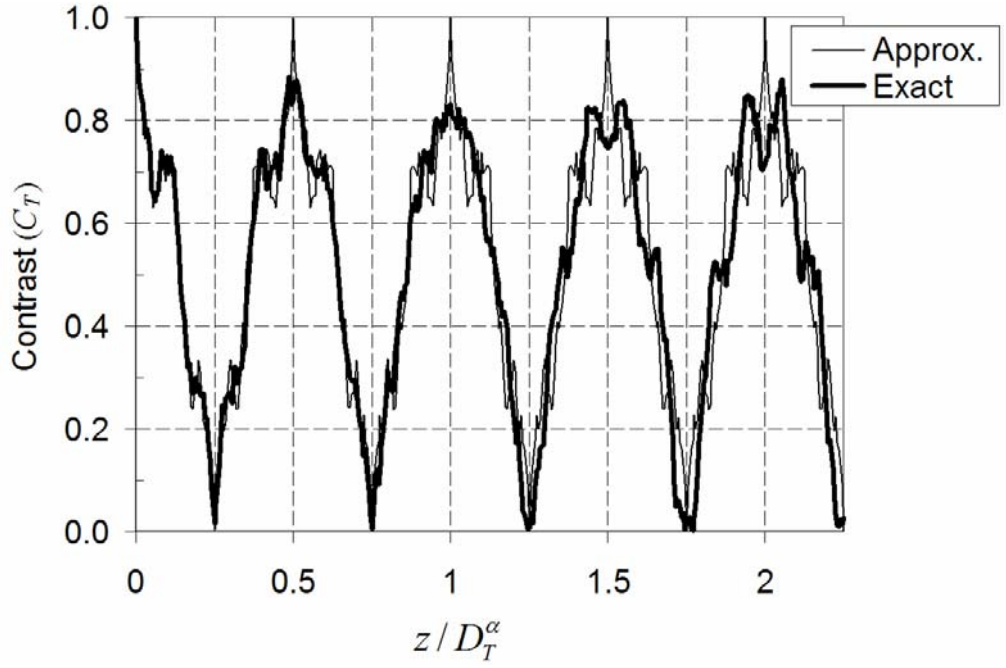

(b)

Figure 2.7 Talbot contrast of shadow moiré fringes with and without parabolic approximation; (a) $\alpha = 0°$ and (b) $\alpha = 45°$.

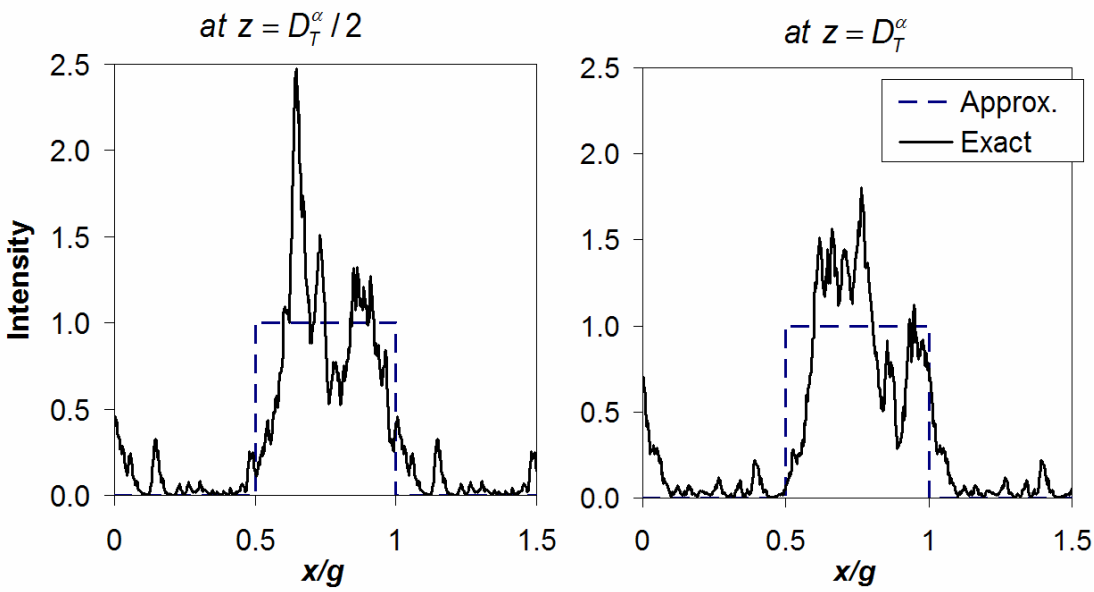

Figure 2.8 Intensity distributions of Talbot images at the half and full Talbot distances when $\alpha = 45°$, $g = 0.1$, and $\lambda = 661$ nm.

Chapter 3. Combined Contrast of Shadow Moiré Fringe

3.1 Aperture Effect on Fringe Contrast of Shadow Moiré

The contrast shown in Fig. 2.6 is valid only when a pinhole aperture is used. In practice, however, the aperture of an imaging system has a finite width. Figure 3.1 illustrates the influence of the aperture on the contrast of shadow moiré fringes, first treated by Kafri and Keren [Kafri 1981] and later by Jassens [Jassens1985].

In Fig. 3.1, the lateral shift of the shadow grating is half the pitch of the reference grating, which is supposed to produce a dark fringe. With the configuration shown in Fig. 3.1 (a) where the aperture is reduced to a point ($d \approx 0$), the light from bright bars cannot enter the camera regardless of the values of z; a uniformly dark fringe is produced. For the case of the aperture shown in Fig. 3.1 (b), however, some of light scattered from bright bars can enter the camera. More light can enter the camera as z increases. The result is an increase of the intensity of dark fringes and thus a decrease in the contrast of moiré fringes.

For the case of a circular aperture, the maximum intensity $\left(I_A^{\max}\right)$ and minimum intensity $\left(I_A^{\min}\right)$ of the shadow moiré fringes can be determined by a geometric analysis as [Kafri 1981] and they can be expressed mathematically as

$$I_A^{\max}(z) = I_0\left(\frac{1}{2} - \frac{2d_e z}{3\pi g}\right)$$
$$I_A^{\min}(z) = I_0\left(\frac{2d_e z}{3\pi g}\right) \tag{3.1}$$

where I_0 is the intensity of a light source and d_e is an *effective aperture* defined as the ratio between the diameter of the aperture d and the distance of the aperture L, i.e., $\frac{d}{L}$. As a geometric analysis based on rectilinear propagation of light was used to derive Eq. 3.1, the aperture effect is valid regardless of the Talbot distance.

When z increases, the difference $I_{max} - I_{min}$ decreases. The contrast becomes zero when $I_{max} = I_{min}$. The condition for complete washout of the fringe pattern $D_{w,}$ or *washout distance*, can be expressed as

$$D_w = \frac{3\pi g}{8d_e} \tag{3.2}$$

Then the contrast attributed to the aperture effect C_A, which will be referred to as *aperture contrast*, can be expressed as

$$C_A(z) = \frac{I_A^{\max}(z) - I_A^{\min}(z)}{I_A^{\max}(z) + I_A^{\min}(z)} = 1 - \frac{8d_e z}{3\pi g} = 1 - \frac{z}{D_w} \quad \text{for } 0 \le z \le \frac{3\pi g}{8d_e} \tag{3.3}$$

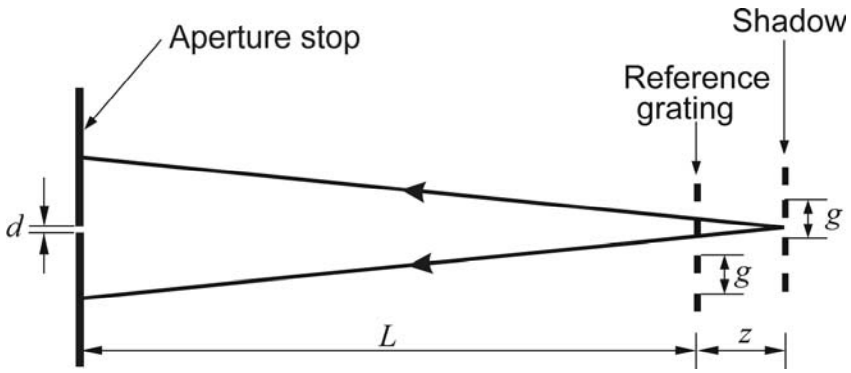

(a)

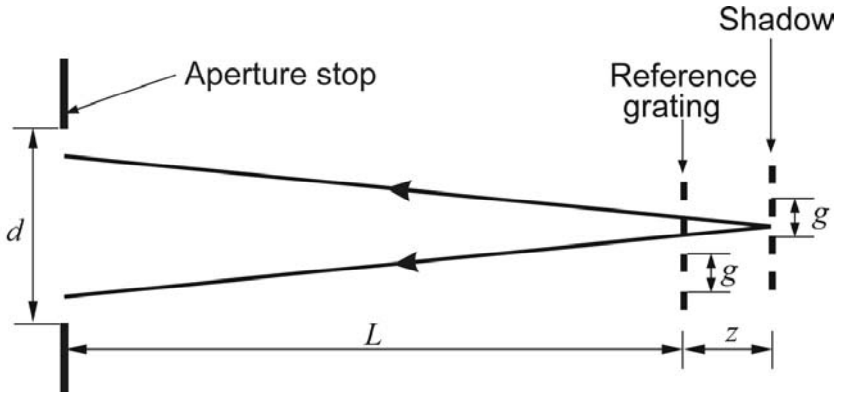

(b)

Figure 3.1 Illustration of the effect of aperture on the contrast of shadow moiré fringes; (a) pin-hole aperture and (b) finite aperture.

3.2 Combined Effect on Fringe Contrast of Shadow Moiré

By combining Talbot contrast (Eq. 2.11) and aperture contrast (Eq. 3.3), the contrast of shadow moiré fringes is defined as

$$C(z) = C_T(z) \times C_A(z) \quad \text{for } 0 \le z \le \frac{3\pi g}{8d_e} \tag{3.4}$$

Equation 3.4 provides a complete expression for the contrast of shadow moiré fringes, considering the combined effect of the diffraction phenomenon and the effective aperture. A practical shadow moiré setup was used to validate the combined effect experimentally.

As illustrated in Fig. 3.2 (a), the specimen was illuminated obliquely at $\alpha = 63.4°$ by a laser diode (λ = 661 nm); the source width was essentially zero. The camera was positioned for normal viewing ($\beta = 0$). The pitch of the reference grating was 0.2 mm. The effective aperture d_e was 0.0245 and the Talbot distance was 10.8 mm. With this arrangement, the contour interval for out-of-plane displacement measurements was 0.1 mm per fringe.

The specimen was a 12 mm square flat glass plate coated with white paint, and it was mounted on a micrometer stage. The specimen was tilted approximately by 1°, which produced two uniformly spaced fringes on the specimen. Numerous fringe patterns were recorded, each for slightly different values of z. Representative fringe patterns obtained at z = 0, $1/8D_T^\alpha$, $1/4D_T^\alpha$, $3/8D_T^\alpha$, $1/4D_T^\alpha$, and $5/8D_T^\alpha$ are shown in Fig. 3.2,

where the white curves represent the intensity distribution averaged along lines parallel to the fringes.

Since a diverging beam was used in the setup, the illumination angle varied across the specimen. However, with the source to specimen distance of 570 mm, the illumination angle varied only 0.3° across the one fringe interval, which had a negligible effect on the Talbot distance calculation.

The contrasts calculated from the experimental data are plotted in Fig. 3.3 together with the theoretical predictions; the solid circles represent the contrasts obtained from the fringe patterns in Fig. 3.2. The experimental results corroborate the validity of combined contrast defined by Eq. 3.4. Note, too, that the maximum local fringe contrast occurs when the gap is slightly less than $D_T^{\alpha}/2$ for these experimental conditions.

Obviously, greater fringe contrast will be achieved with smaller effective apertures. Figure 3.3 (b) shows the theoretical results for the same experimental parameters, except $d_e = 0.005$.

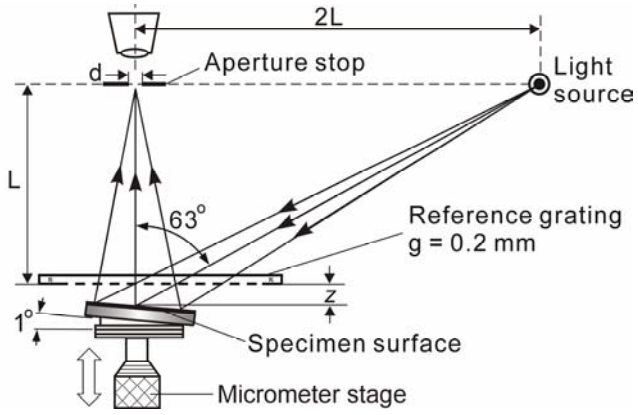

(a)

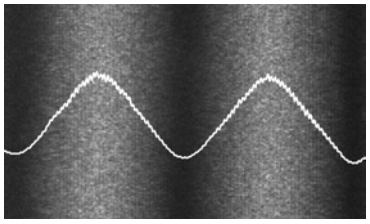

(b)

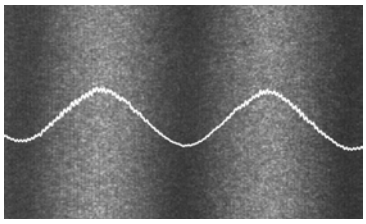

(c)

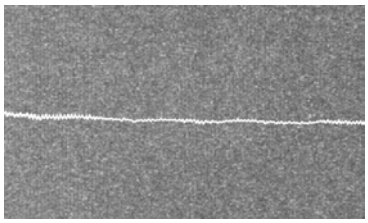

(d)

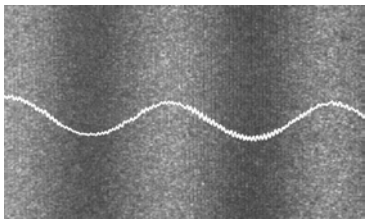

(e)

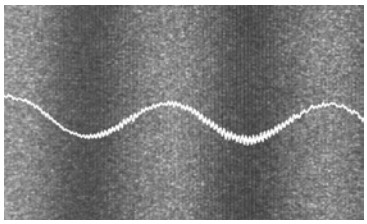

(f)

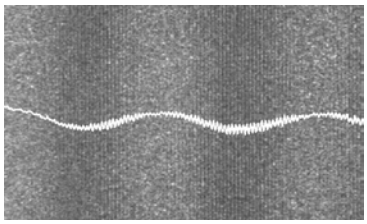

(g)

Figure 3.2 (a) Experimental setup to measure the contrast of shadow moiré fringes, and fringe pattern obtained as z = (b) 0, (c) 1/8 D_T^{α} , (d) 1/4 D_T^{α} , (e) 3/8 D_T^{α} , (f) 1/2 D_T^{α} , and (g) 5/8 D_T^{α} .

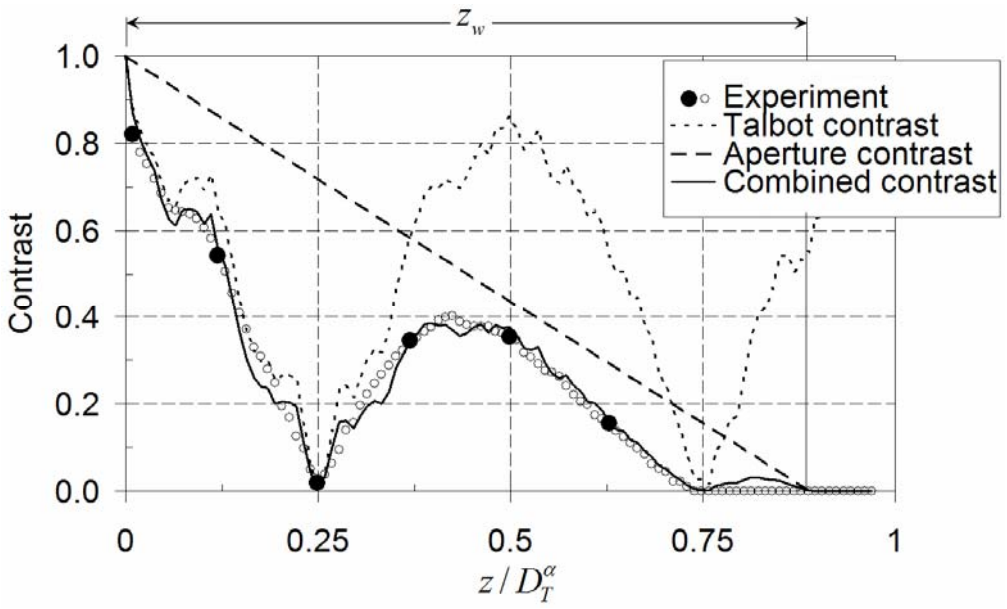

(a)

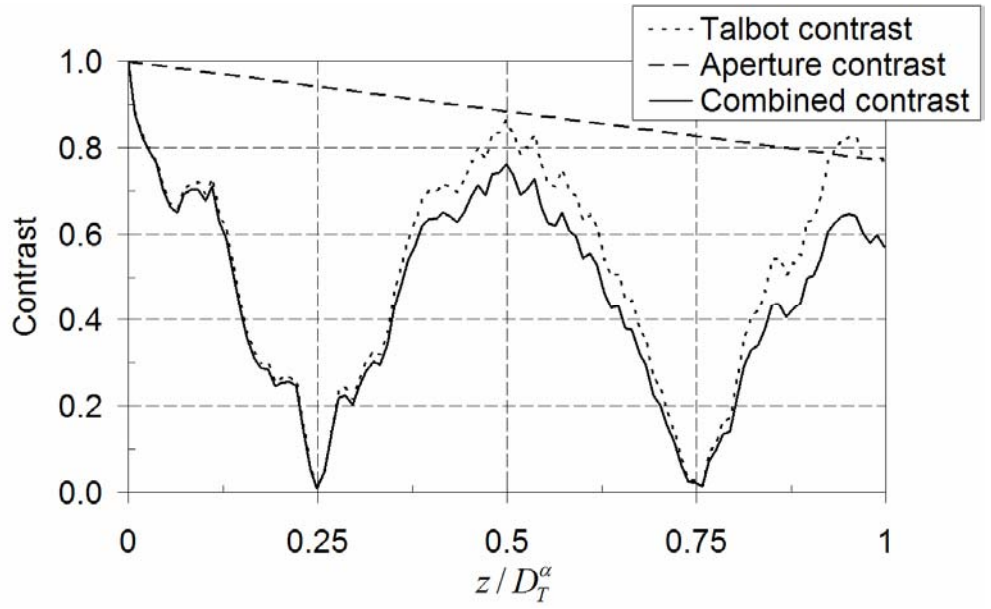

(b)

Figure 3.3 Combined contrast of shadow moiré fringe and its experimental verification with optical parameters $\alpha = 63.4°$, $\lambda = 661$ nm, $g = 0.2$ mm, and (a) $d_e = 0.0245$, (b) $d_e = 0.005$.

Chapter 4. Effect of Broad Spectrum Light on Shadow Moiré Fringe

4.1 Introduction

In the previous chapters, monochromatic light is assumed to derive the contrast and intensity function of shadow moiré fringe. Shadow moiré is basically a geometric moiré and it does not require a monochromatic light source. In fact, white light is preferred in practice to avoid noise caused by a coherent light source such as speckle and multiple reflections. In this chapter, the effect of a broad spectrum light source on the shadow moiré fringe will be investigated.

4.2 Effect of Parabolic Approximation on the Talbot Contrast

The intensity of broad spectrum light can be determined by superposing the intensity of each wavelength [Post 1994]. The intensity of shadow images of Ronchi ruling then can be expressed as

$$I_{\lambda_{12}} = \frac{1}{\lambda_2 - \lambda_1} \int_{\lambda_1}^{\lambda_2} I(x,z;\lambda) d\lambda \tag{4.1}$$

where $I(x,z;\lambda)$ is the intensity distribution of the Talbot image defined by Eq. 2.8, λ_1 and λ_2 are the smallest and largest wavelength of the light source, respectively.

Equations 4.1 can be evaluated numerically by

$$I_{\lambda_{12}} \cong \frac{1}{\Delta\lambda} \sum_{k=0}^{k=N} I(x, z; \lambda\big|_k)\delta\lambda \tag{4.1b}$$

where $\Delta\lambda = \lambda_2 - \lambda_1$, $\lambda\big|_k = \lambda_1 + k\delta\lambda$, $\delta\lambda = (\lambda_2 - \lambda_1)/N$, and $k = 0, 1, 2, 3, \ldots N$.

Similar to the interference with a broad spectrum light [Post, 1994], it is expected that the high frequency peaks shown in the intensity distribution obtained by the exact solution (Fig. 2.7) will diminish as the spectral band width $(\Delta\lambda)$ of the light source increases. Consequently, the effect of the parabolic approximation would also decrease as $\Delta\lambda$ increases. This speculation is verified numerically.

The intensity distributions using the parabolic approximation, corresponding to Eqs. 4.1 and 4.1b, can be expressed as

$$I_{p\lambda_{12}} = \frac{1}{\Delta\lambda} \int_{\lambda_1}^{\lambda_2} I_P(x, z; \lambda) d\lambda \tag{4.2}$$

$$I_{p\lambda_{12}} \cong \frac{1}{\Delta\lambda} \sum_{k=0}^{k=N} I_p(x, z; \lambda\big|_k)\delta\lambda \tag{4.2b}$$

where $I_p(x, z; \lambda)$ is the approximated intensity function defined at Eq. 2.5.

Equations 4.1b and 4.2b were evaluated numerically using $\delta\lambda$ of 0.1 nm. The value of $\delta\lambda$ was chosen after a series of calculations with different values of $\delta\lambda$ to check the convergence; the numerical results remained virtually unchanged with $\delta\lambda$ smaller

than 0.1 nm. The intensity distributions at half the Talbot distance and the full Talbot distance were calculated for the configuration used to produce Fig. 2.8 (g = 0.1 mm and α = 45°). The results are shown in Fig. 4.1, where the central wavelength $\left(\lambda_c = \frac{\lambda_2 + \lambda_1}{2} \right)$ was 550 nm and $\Delta\lambda$ was (a) 0 nm (monochromatic light), (b) 50 nm, (c) 100 nm and (d) 300 nm (white light). Note that the Talbot distance was calculated using λ_c.

The results indicate the effect of broad spectrum clearly; as the spectral band width increases, the difference between two intensity distributions diminishes. The intensity distributions become virtually identical to each other when a white light source is used. To assure the implications from the numerical analysis, numerous cases with different geometrical parameters were calculated. Figures 4.2 and 4.3 show the selected results from the calculations, where g = 0.1 mm and α = 63°, and g = 0.2 mm and α = 63°, respectively. Again two intensity distributions are virtually the same at multiples of half the Talbot distance.

The above numerical analysis provides a theoretical justification for using the parabolic approximation when a broad spectrum light source is used; the effect of parabolic approximation is negligible if $\Delta\lambda > 100\,\text{nm}$. Consequently, the approximated intensity of Eq. 4.2 will be used in the following analysis using a broad spectrum light.

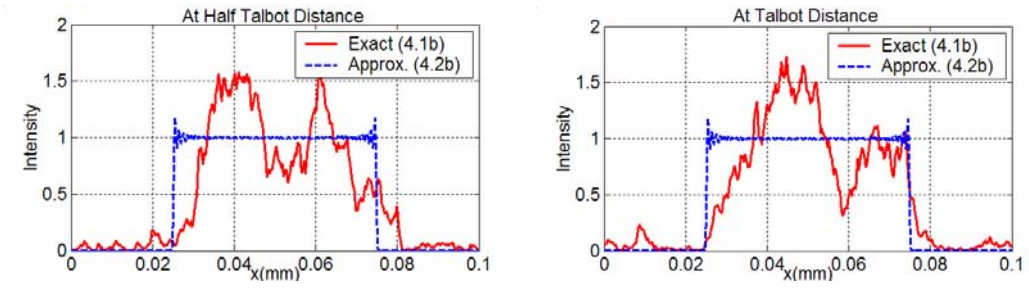

(a)

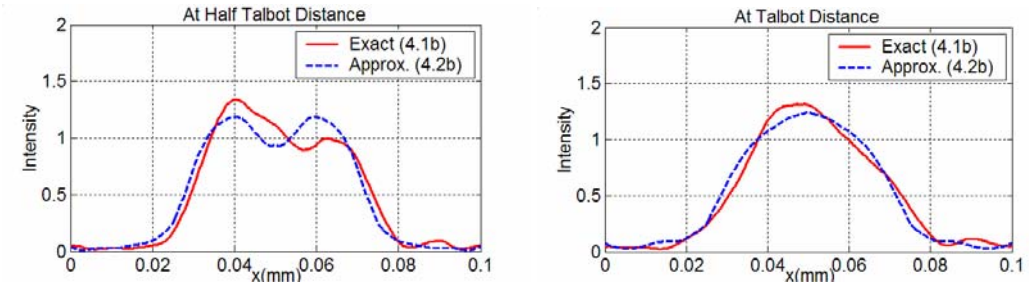

(b)

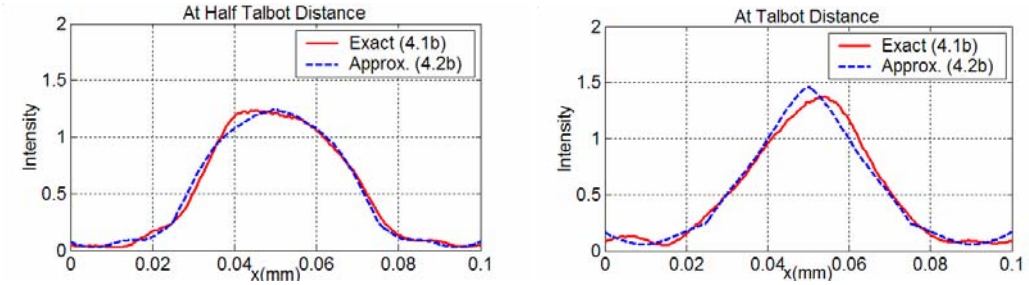

(c)

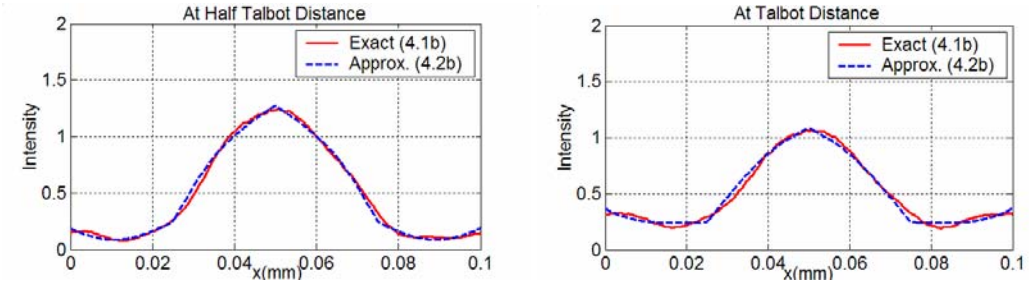

(d)

Figure 4.1 Shape of intensities of g = 0.1 mm and α =45° at half Talbot distance and full Talbot distance with wavelength of (a) 550 nm, (b) 525 – 575 nm, (c) 500 – 600 nm, and (d) 400 – 700 nm.

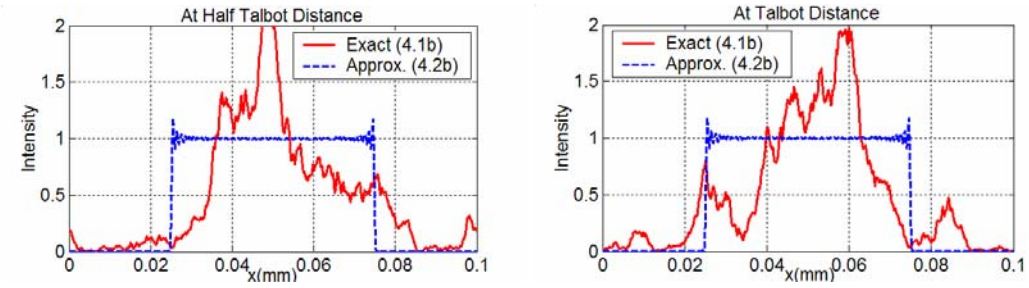

(a)

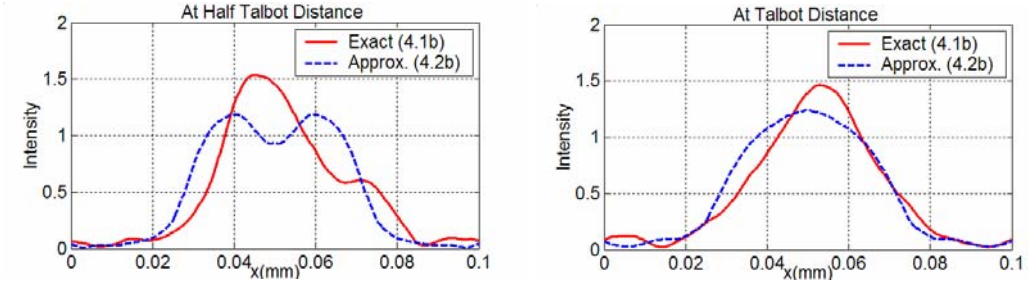

(b)

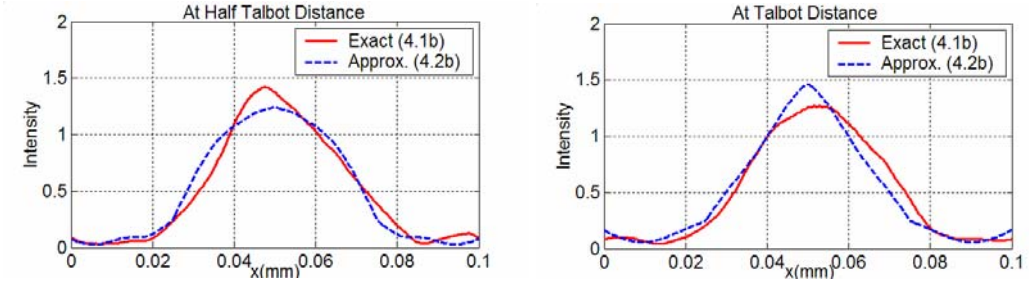

(c)

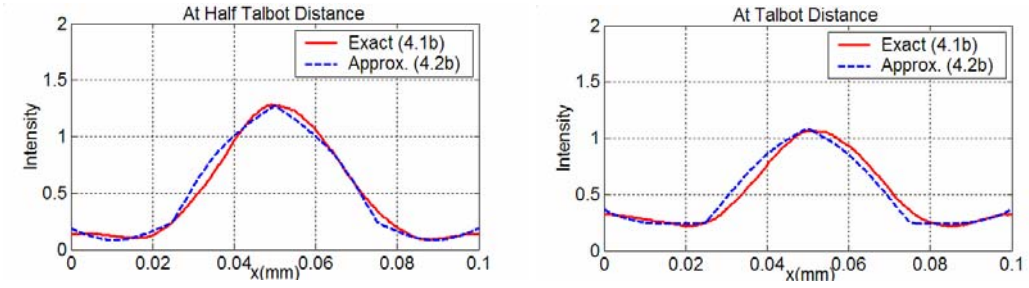

(d)

Figure 4.2 Shape of intensities of g = 0.1 mm and α =63° at half Talbot distance and full Talbot distance with wavelength of (a) 550 nm, (b) 525 – 575 nm, (c) 500 – 600 nm, and (d) 400 – 700 nm.

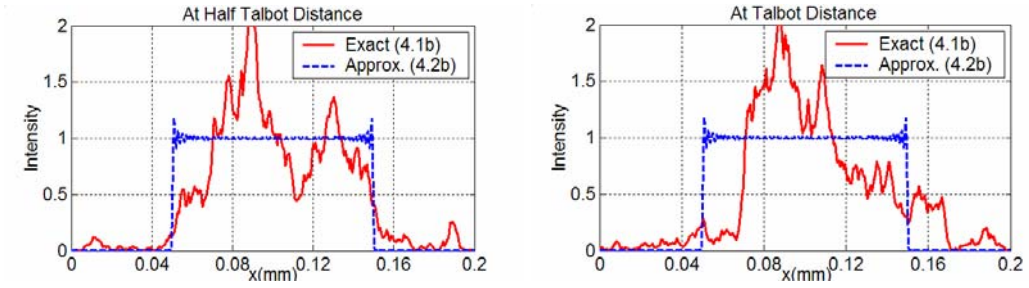

(a)

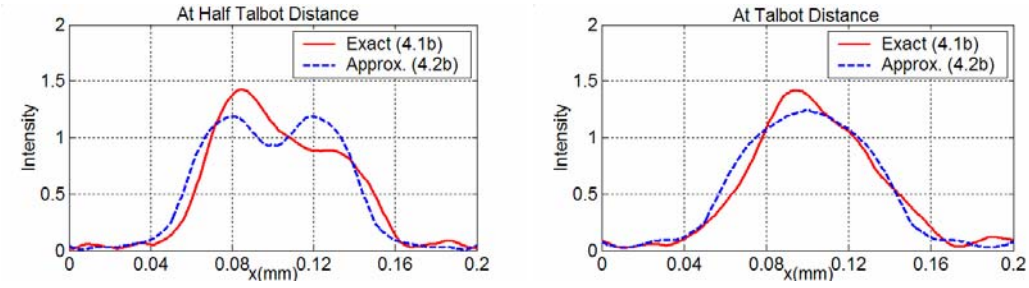

(b)

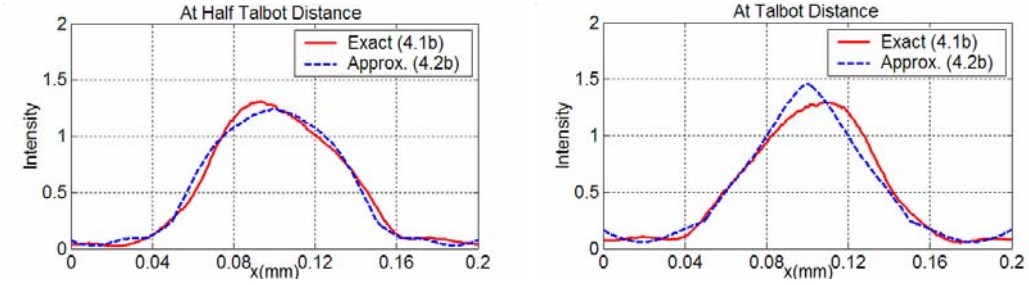

(c)

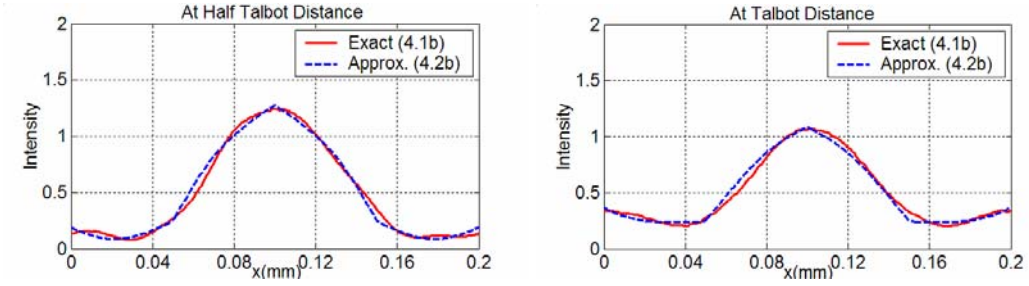

(d)

Figure 4.3 Shape of intensities of g = 0.2 mm and α =63° at half Talbot distance and full Talbot distance with wavelength of (a) 550 nm, (b) 525 – 575 nm, (c) 500 – 600 nm, and (d) 400 – 700 nm.

4.3 Intensity Distribution of Shadow Moiré Fringes Produced by Broad Spectrum Light Source

From Eqs. 4.2b and 2.5, the intensity of Talbot image formed by a broad spectrum light source can be written as

$$I_{p\lambda_{12}} = \frac{1}{\Delta\lambda}\int_{\lambda_1}^{\lambda_2} I_P(x,z;\lambda)d\lambda$$

$$= \frac{1}{\Delta\lambda}\int_{\lambda_1}^{\lambda_2}\left[\sum_{n=-\infty}^{\infty}\sum_{m=-\infty}^{\infty} a_n a_m \exp\left\{i2\pi(n-m)\frac{x-z\tan\alpha}{g}\right\}\exp\left\{i\pi\left(\frac{m^2-n^2}{g^2\cos^3\alpha}z\right)\lambda\right\}\right] \tag{4.3}$$

$$= \frac{1}{\Delta\lambda}\sum_{n=-\infty}^{\infty}\sum_{m=-\infty}^{\infty} a_n a_m \exp\left\{i2\pi(n-m)\frac{x-z\tan\alpha}{g}\right\}\int_{\lambda_1}^{\lambda_2}\exp\left\{i\pi\left(\frac{m^2-n^2}{g^2\cos^3\alpha}z\right)\lambda\right\}d\lambda$$

The intensity distribution of shadow moiré fringes formed by a broad spectrum light, $I_s(z)$, can be expressed as

$$I_s(z) = \frac{1}{g}\int_{-g/2}^{g/2}\left\{I(x,0)I_{p\lambda_{12}}(x,z)\right\}dx \tag{4.4}$$

By substituting Eq. 4.3 into Eq. 4.4,

$$I_s(z) = \frac{1}{g}\int_{-g/2}^{g/2}\left[I(x,0)\right]\left[\frac{1}{\Delta\lambda}\sum_{n=-\infty}^{\infty}\sum_{m=-\infty}^{\infty} a_n a_m \exp\left\{i2\pi(n-m)\left(\frac{x - z\tan\alpha}{g}\right)\right\}\right.$$
$$\left.\times\int_{\lambda_1}^{\lambda_2}\exp\left\{i\pi\left(\frac{m^2-n^2}{g^2\cos^3\alpha}z\right)\lambda\right\}d\lambda\right]dx$$
$$= \frac{1}{\Delta\lambda}\sum_{n=-\infty}^{\infty}\sum_{m=-\infty}^{\infty} a_n a_m \exp\left\{i2\pi(n-m)\left(\frac{-z\tan\alpha}{g}\right)\right\}$$
$$\times\frac{1}{g}\int_{-g/2}^{g/2} I(x,0)\exp\left\{i2\pi(n-m)\left(\frac{x}{g}\right)\right\}dx$$
$$\times\int_{\lambda_1}^{\lambda_2}\exp\left\{i\pi\left(\frac{m^2-n^2}{g^2\cos^3\alpha}z\right)\lambda\right\}d\lambda \tag{4.5}$$

For the Ronchi ruling,

$$a_n = \begin{cases} (-1)^{(n-1)/2}/\pi n & \text{if } n = \text{odd} \\ 1/2 & \text{if } n = 0 \\ 0 & \text{if } n = \text{even} \end{cases} \tag{4.6a}$$

$$\frac{1}{g}\int_{-g/2}^{g/2} I(x,0)\exp\left\{i2\pi(n-m)\left(\frac{x}{g}\right)\right\}dx$$
$$= \frac{1}{g}\int_{-g/4}^{g/4}\exp\left\{i2\pi(n-m)\left(\frac{x}{g}\right)\right\}dx \tag{4.6b}$$
$$= \begin{cases} 0 & \text{if } n-m = \text{even}(\neq 0) \\ \dfrac{(-1)^{(n-m-1)/2}}{\pi(n-m)} & \text{if } n-m = \text{odd} \\ 1/2 & \text{if } n-m = 0 \end{cases}$$

$$\int_{\lambda_1}^{\lambda_2} \exp\left\{ i\pi \left(\frac{m^2 - n^2}{g^2 \cos^3 \alpha} z \right) \lambda \right\} d\lambda$$

$$= \begin{cases} \dfrac{g^2 \cos^3 \alpha}{i\pi \left(m^2 - n^2 \right) z} \exp\left[i \dfrac{\pi \left(m^2 - n^2 \right) z}{g^2 \cos^3 \alpha} \lambda \right]_{\lambda_1}^{\lambda_2} & \text{if } m^2 \neq n^2 \text{ and } z \neq 0 \\ \lambda_2 - \lambda & \text{if } m^2 = n^2 \text{ or } z = 0 \end{cases} \tag{4.6c}$$

Using Eq. 4.6, Eq. 4.5 can be written as

$$I_s(z) = \begin{cases} \dfrac{1}{8} & (n = m = 0) \\ \displaystyle\sum_{n=-\infty}^{\infty} \frac{1}{\pi^2 n^2} \frac{1}{2} = \frac{1}{8} & (n = m, \ not \ \ 0) \\ \dfrac{1}{\Delta\lambda} \displaystyle\sum_{m'=-\infty}^{\infty} \frac{1}{2\pi^2 (2m' - 1)^2} \frac{g^2 \cos^3 \alpha}{i\pi (2m' - 1)^2} \exp\left\{ i2\pi (2m' - 1) \left(\frac{z \tan \alpha}{g} \right) \right\} & \\ \quad \times \dfrac{1}{z} \left[\exp\left\{ i \dfrac{\pi (2m' - 1)^2 z}{g^2 \cos^3 \alpha} \lambda_2 \right\} - \exp\left\{ i \dfrac{\pi (2m' - 1)^2 z}{g^2 \cos^3 \alpha} \lambda_1 \right\} \right] & (n = 0, m = 2m' - 1) \\ \dfrac{1}{\Delta\lambda} \displaystyle\sum_{n'=-\infty}^{\infty} \frac{1}{2\pi^2 (2n' - 1)^2} \frac{g^2 \cos^3 \alpha}{i\pi (-(2n' - 1)^2)} \exp\left\{ i2\pi (2n' - 1) \left(\frac{-z \tan \alpha}{g} \right) \right\} & \\ \quad \times \dfrac{1}{z} \left[\exp\left\{ -i \dfrac{\pi (2n' - 1)^2 z}{g^2 \cos^3 \alpha} \lambda_2 \right\} - \exp\left\{ -i \dfrac{\pi (2n' - 1)^2 z}{g^2 \cos^3 \alpha} \lambda_1 \right\} \right] & (m = 0, n = 2n' - 1) \end{cases} \tag{4.7}$$

(where $z \neq 0$)

By adding up each term of Eq. 4.7,

$$I_s(z)=\frac{1}{4}+\frac{1}{\Delta\lambda}\sum_{n=-\infty}^{\infty}\frac{g^2\cos^3\alpha}{\pi^3(2n-1)^4}\frac{1}{z}\left[\sin\left\{\frac{\pi(2n-1)^2 z}{g^2\cos^3\alpha}\lambda_2+\frac{2\pi(2n-1)z}{g/\tan\alpha}\right\}-\sin\left\{\frac{\pi(2n-1)^2 z}{g^2\cos^3\alpha}\lambda_1+\frac{2\pi(2n-1)z}{g/\tan\alpha}\right\}\right] \tag{4.8}$$

(where $z \neq 0$)

The sinusoidal term in Eq. 4.8 can be converted into

$$\begin{aligned}
&\sin\left\{\frac{\pi(2n-1)^2 z}{g^2\cos^3\alpha}\lambda_2+\frac{2\pi(2n-1)z}{g/\tan\alpha}\right\}-\sin\left\{\frac{\pi(2n-1)^2 z}{g^2\cos^3\alpha}\lambda_1+\frac{2\pi(2n-1)z}{g/\tan\alpha}\right\}\\
&=2\cos\left\{\frac{\pi(2n-1)^2 z\left(\lambda_2+\lambda_1\right)}{2g^2\cos^3\alpha}+\frac{2\pi(2n-1)z}{g/\tan\alpha}\right\}\sin\left\{\frac{\pi(2n-1)^2 z\left(\lambda_2-\lambda_1\right)}{2g^2\cos^3\alpha}\right\}\\
&=2\cos\left\{2\pi(2n-1)^2\frac{z}{\frac{2g^2\cos^3\alpha}{\left(\lambda_2+\lambda_1\right)/2}}+\frac{2\pi(2n-1)z}{g/\tan\alpha}\right\}\sin\left\{2\pi(2n-1)^2\frac{z}{\frac{2g^2\cos^3\alpha}{\left(\lambda_2-\lambda_1\right)/2}}\right\}\\
&=2\cos\left\{2\pi(2n-1)^2\frac{z}{D_T^{\alpha}}+\frac{2\pi(2n-1)z}{g/\tan\alpha}\right\}\sin\left\{2\pi(2n-1)^2\frac{z}{D_{T,secondary}^{\alpha}}\right\}
\end{aligned} \tag{4.9}$$

where "Talbot distance" and "secondary Talbot distance" are defined, respectively, as

$$D_T^{\alpha}=\frac{2g^2\cos^3\alpha}{\left(\lambda_1+\lambda_2\right)/2}=\frac{2g^2\cos^3\alpha}{\lambda_c} \quad \text{and} \quad D_{T,secondary}^{\alpha}=\frac{2g^2\cos^3\alpha}{\left(\lambda_1-\lambda_2\right)/2}=\frac{2g^2\cos^3\alpha}{\Delta\lambda/2}$$

Using the relation of Eq. 4.9, Eq. 4.8 can be written as

$$I_s(z)=\frac{1}{4}+\sum_{n=-\infty}^{\infty}\frac{1}{\pi^2(2n-1)^2}\cos\left\{2\pi z\left(\frac{(2n-1)^2}{D_T^{\alpha}}+\frac{(2n-1)}{g/\tan\alpha}\right)\right\}\operatorname{sinc}\left\{2z\frac{(2n-1)^2}{D_{T,secondary}^{\alpha}}\right\} \tag{4.10}$$

where

$$\mathrm{sinc}(x) = \frac{\sin(\pi x)}{(\pi x)}$$

The second term in sum of Eq. 4.10 can be extended as

$$\begin{aligned}\cos\left\{2\pi z\left(\frac{(2n-1)^2}{D^{\alpha}_{T,primary}}+\frac{(2n-1)}{g/\tan\alpha}\right)\right\} = &\cos\left\{2\pi z\left(\frac{(2n-1)^2}{D^{\alpha}_{T}}\right)\right\}\cos\left\{2\pi z\left(\frac{(2n-1)}{g/\tan\alpha}\right)\right\} \\ &-\sin\left\{2\pi z\left(\frac{(2n-1)^2}{D^{\alpha}_{T}}\right)\right\}\sin\left\{2\pi z\left(\frac{(2n-1)}{g/\tan\alpha}\right)\right\}\end{aligned} \tag{4.11}$$

Finally, Eq. 4.10 can be written as

$$I_s(z) = \frac{1}{4}+\sum_{n=1}^{\infty}\frac{2}{\pi^2(2n-1)^2}\cos\left\{\frac{2\pi z(2n-1)^2}{D^{\alpha}_{T}}\right\}\cos\left\{\frac{2\pi z(2n-1)}{g/\tan\alpha}\right\}\mathrm{sinc}\left\{\frac{2z(2n-1)^2}{D^{\alpha}_{T,secondary}}\right\} \tag{4.12}$$

Equation 4.12 expresses the intensity distribution of shadow moiré fringe formed by a broad spectrum light source. In the equation, the first *cosine* term represents the effect of diffraction, the second term is similar to the rectilinear term in Eq. 2.5, and the third term of the *sinc* function shows the effect of the broad spectrum.

4.4 Talbot Contrast for Broad Spectrum Light Source

The mathematical procedure used in Section 2.3 is repeated to determine the Talbot contrast of shadow moiré fringes produced by a broad spectrum light source. Using Eq. 2.10, the maximum and minimum intensity can be expressed as

$$\begin{aligned} I_s^{\max}(z) &= \frac{1}{g}\int_{-g/2}^{g/2}\left\{I(x,0)I_{p\lambda_{12}}(x+z\tan\alpha,z)\right\}dx \\ I_s^{\min}(z) &= \frac{1}{g}\int_{-g/2}^{g/2}\left\{I(x,0)I_{p\lambda_{12}}(x+z\tan\alpha+g/2,z)\right\}dx \end{aligned} \tag{4.13}$$

The Talbot contrast can be expressed as

$$\begin{aligned} \text{Contrast} &= \left|\frac{I_s^{\max}(z)-I_s^{\min}(z)}{I_s^{\max}(z)+I_s^{\min}(z)}\right| \\ &= \left|\frac{4}{\Delta\lambda}\sum_{n=-\infty}^{\infty}\frac{g^2\cos^3\alpha}{\pi^3(2n-1)^4}\frac{1}{z}\left[\sin\left\{\frac{\pi(2n-1)^2 z}{g^2\cos^3\alpha}\lambda_2\right\}-\sin\left\{\frac{\pi(2n-1)^2 z}{g^2\cos^3\alpha}\lambda_1\right\}\right]\right| \end{aligned} \tag{4.14}$$

(where $z \neq 0$)

Sinusoidal term in the Eq. 4.14 can be converted into

$$\begin{aligned} &\sin\left\{\frac{\pi(2n-1)^2 z\lambda_2}{g^2\cos^3\alpha}\right\}-\sin\left\{\frac{\pi(2n-1)^2 z\lambda_1}{g^2\cos^3\alpha}\right\} \\ &= 2\cos\left\{\frac{\pi(2n-1)^2 z(\lambda_2+\lambda_1)}{2g^2\cos^3\alpha}\right\}\sin\left\{\frac{\pi(2n-1)^2 z(\lambda_2-\lambda_1)}{2g^2\cos^3\alpha}\right\} \\ &= 2\cos\left\{2\pi(2n-1)^2\frac{z}{\frac{2g^2\cos^3\alpha}{\lambda_c}}\right\}\sin\left\{2\pi(2n-1)^2\frac{z}{\frac{2g^2\cos^3\alpha}{\Delta\lambda/2}}\right\} \\ &= 2\cos\left\{2\pi(2n-1)^2\frac{z}{D_T^{\alpha}}\right\}\sin\left\{2\pi(2n-1)^2\frac{z}{D_{T,secondary}^{\alpha}}\right\} \end{aligned} \tag{4.15}$$

Finally, the Talbot contrast can be written as

$$\begin{aligned}
\text{Contrast} &= \left| \sum_{n=-\infty}^{\infty} \frac{2}{\pi^3 (2n-1)^4} \frac{D_{T,secondary}^{\alpha}}{z} \cos\left\{ 2\pi (2n-1)^2 \frac{z}{D_T^{\alpha}} \right\} \sin\left\{ 2\pi (2n-1)^2 \frac{z}{D_{T,secondary}^{\alpha}} \right\} \right| \\
&= \left| \sum_{n=-\infty}^{\infty} \frac{4}{\pi^2 (2n-1)^2} \frac{D_{T,secondary}^{\alpha}}{2\pi (2n-1)^2 z} \cos\left\{ 2\pi (2n-1)^2 \frac{z}{D_T^{\alpha}} \right\} \sin\left\{ 2\pi (2n-1)^2 \frac{z}{D_{T,secondary}^{\alpha}} \right\} \right| \\
&= \left| \sum_{n=-\infty}^{\infty} \frac{4}{\pi^2 (2n-1)^2} \cos\left\{ 2\pi (2n-1)^2 \frac{z}{D_T^{\alpha}} \right\} \text{sinc}\left\{ 2(2n-1)^2 \frac{z}{D_{T,secondary}^{\alpha}} \right\} \right| \\
&= \left| \sum_{n=1}^{\infty} \frac{8}{\pi^2 (2n-1)^2} \cos\left\{ 2\pi (2n-1)^2 \frac{z}{D_T^{\alpha}} \right\} \text{sinc}\left\{ 2(2n-1)^2 \frac{z}{D_{T,secondary}^{\alpha}} \right\} \right|
\end{aligned} \tag{4.16}$$

4.5 Experimental Validation of Talbot Contrast for Broad Spectrum Light Source

An experiment was conducted to verify the validity of Eq. 4.16. The test setup shown in Fig. 2.4 was used with a 250 W white light illuminator (Fiberoptic Systems, Inc. Model 1060-250). The light source is coupled to a bundle of optical fiber, which forms a linear light source.

Fringe patterns were obtained over several Talbot distances while moving the micrometer stage. Representative fringe patterns obtained at quarter and half the first Talbot distance are shown in Fig. 4.4. The maximum and minimum intensities were determined digitally from the patterns and the contrast was determined using Eq. 4.16. The experimental results are plotted in Fig. 4.5, where the contrasts obtained from the experiment are compared with the theoretical values (Eq. 4.16). The results confirm that Eq. 4.16 faithfully defines the Talbot contrast with a broad spectrum light source.

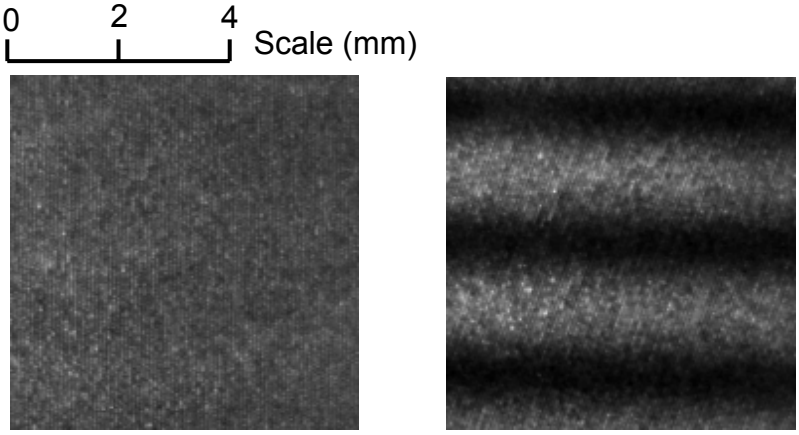

(a) (b)

Figure 4.4 Fringe pattern with white light at

(a) $z = 0.25 D_T^{\alpha}$ and (b) $z = 0.5\, D_T^{\alpha}$.

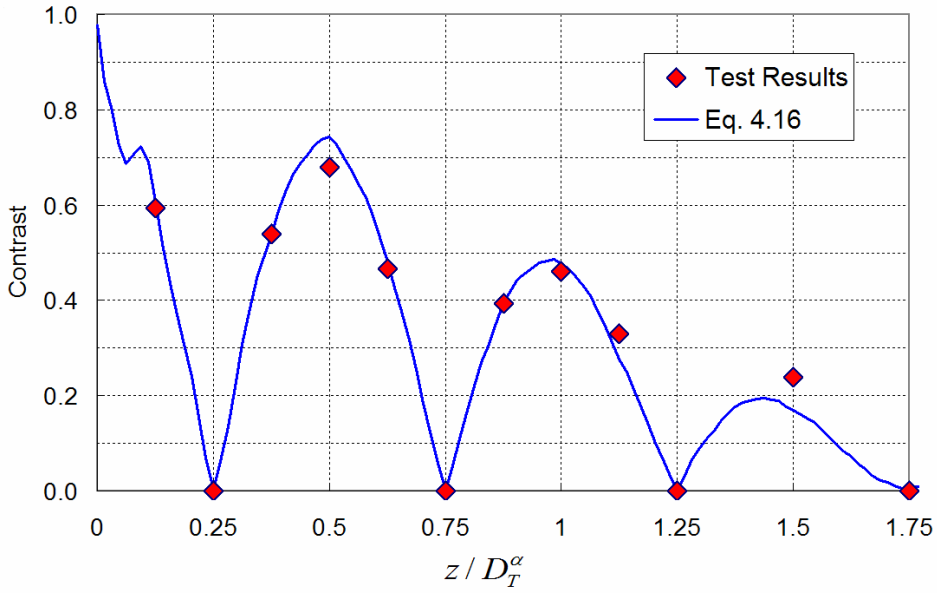

Figure 4.5 Experimental results of Talbot contrast with white light are compared with theoretical prediction.

4.6 Analysis of Talbot Contrast with Broad Spectrum Light Source

It has been proven that Eq. 4.16 is valid if $\Delta\lambda > 100$ nm. It is to be noted that the Talbot contrast is a function of only three parameter; z (the distance between the grating and the specimen surface), D_T^{α} (Talbot distance), and $D_{T,secondary}^{\alpha}$ (secondary Talbot distance).

The secondary Talbot distance can be written as

$$D_{T,secondary}^{\alpha} = D_T^{\alpha} \frac{\lambda_2 + \lambda_1}{\lambda_2 - \lambda_1} = D_T^{\alpha} \frac{\lambda_c}{2\Delta\lambda} \tag{4.17}$$

As can be seen from Eq. 4.17, the secondary Talbot distance increases as the spectral band width, $\Delta\lambda$, decreases for a given central wavelength, λ_c; $D_{T,secondary}^{\alpha}$ approaches infinity when a monochromatic light $(\Delta\lambda = 0)$ is used.

Figure 4.6 illustrates the effect of the secondary Talbot distance on the Talbot contrast. The Talbot contrast for a monochromatic light of λ = 550 nm (Eq. 2.11) is plotted in Fig. 4.6 (a), where g = 0.1 mm and α = 63°. The corresponding Talbot contrast for a white light $(\lambda_c = 550$ nm and $\Delta\lambda = 300$ nm$)$ is plotted in Fig. 4.6 (b) together with the absolute value of the *sinc* function (dotted line in the figure). It is interesting to note that the final Talbot contrast for a white light is basically the Talbot contrast for a monochromatic light modulated by the *sinc* function. The period of the *sinc* function

is secondary Talbot distance, $D_{T,secondary}^{\alpha}$. Consequently, the smaller $D_{T,secondary}^{\alpha}$ is, the more rapidly the Talbot contrast decreases at higher Talbot distances.

Figure 4.7 illustrates the effect of $\Delta\lambda$ on $D_{T,secondary}^{\alpha}$ and thus the Talbot contrast. In Fig. 4.7 (a), the absolute values of the *sinc* functions are plotted for three different values of $\Delta\lambda$ (100, 200 and 300 nm). The corresponding Talbot contrast is plotted in Fig. 4.7 (b). The plots clearly indicate the decrease in the secondary Talbot distance and the subsequent reduction of the Talbot contrast with the larger values of $\Delta\lambda$. It is important to note that the Talbot contrast at half the Talbot distance remains virtually unchanged regardless of the value of $\Delta\lambda$; the spectral band width of a light source does not affect the Talbot contrast significantly as long as the zero or half the Talbot distance is used in shadow moiré. The above analysis provides a theoretical rationale for the optimum optical configurations of shadow moiré using non-zero Talbot distance proposed in a later chapter.

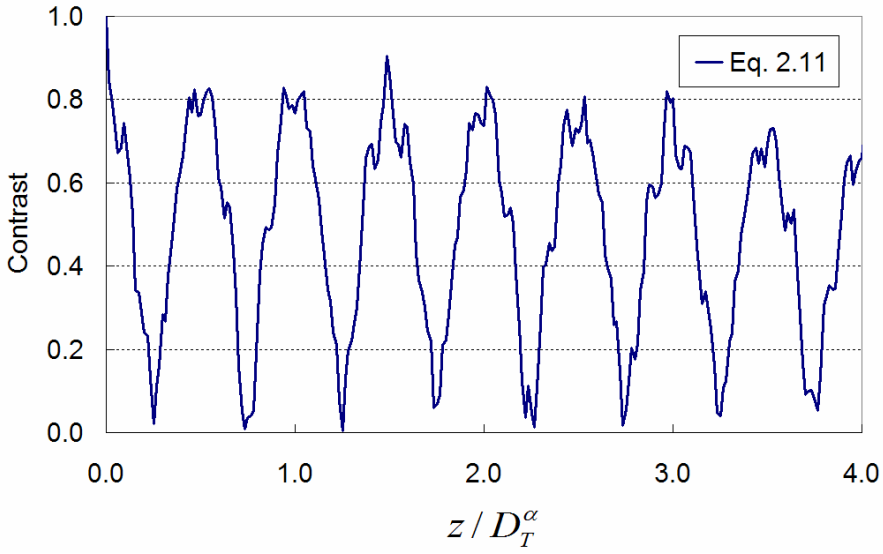

(a)

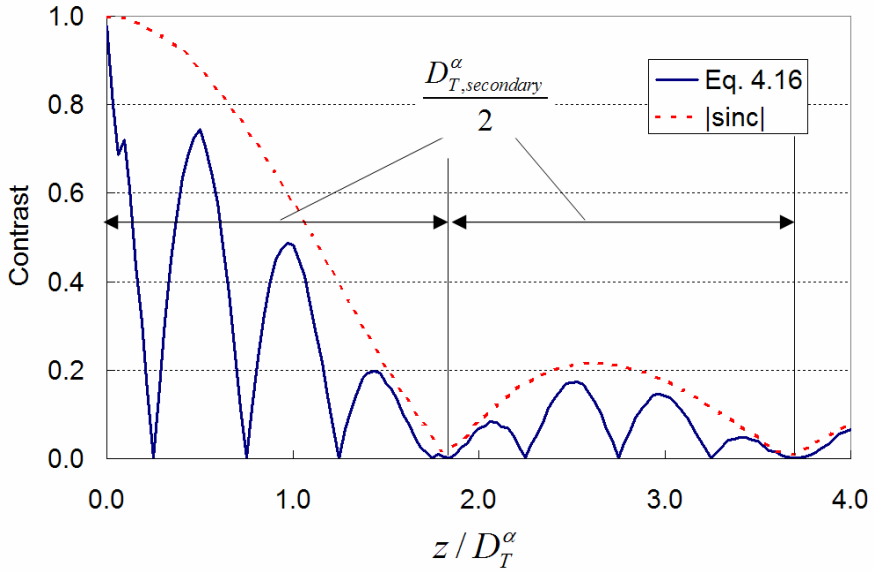

(b)

Figure 4.6 Illustration of broad spectrum effect on the Talbot contrast of shadow moiré with 10 lines/mm and 63° illuminations; (a) monochromatic light (550 nm) vs (b) white light (400 – 700 nm).

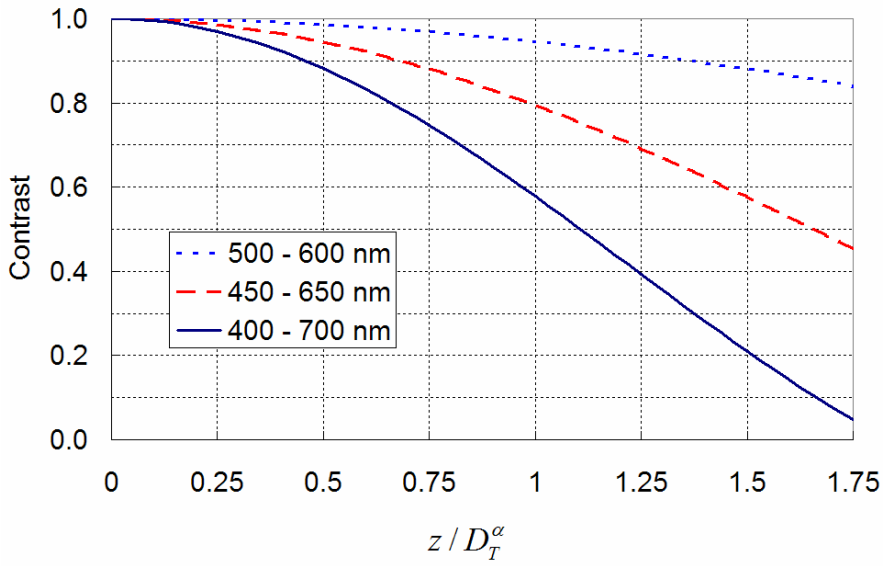

(a)

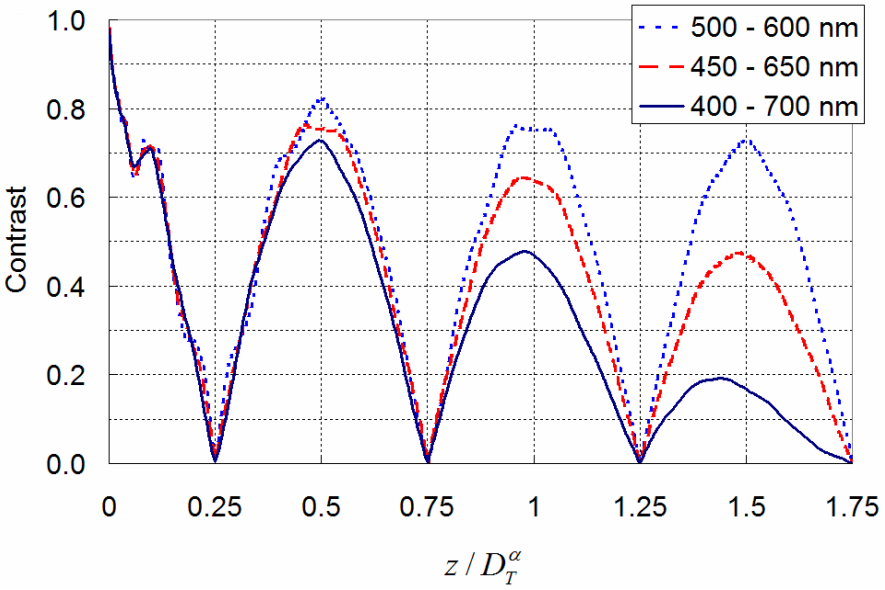

(b)

Figure 4.7 Illustration of effect of wavelength width of light source on the Talbot contrast: (a) absolute sinc function, (b) Talbot contrast.

Chapter 5. High Sensitivity Shadow Moiré Using Non-zero Talbot Distance (SM-NT)

5.1 Theoretical Limit of Measurement Sensitivity of Shadow Moiré

5.1.1 Analysis of Phase-shifting Error in Shadow Moiré

The previous chapters have contributed to the complete understanding of the intensity distribution of shadow moiré fringe. In this chapter, the errors induced by the non-sinusoidal intensity distribution will be quantified using shadow moiré fringe produced by a broad spectrum light source.

Substituting Eq. 4.12 into Eq. 1.11, the true intensity distribution of the four phase-shifted patterns, $I_i^S(z)$, can be expressed as

$$I_i^S(z) = I_s\left(z + \left(\frac{g}{4\tan\alpha}\right)(i-1)\right) \quad , \quad i = 0, 1, 2, 3 \tag{5.1}$$

The corresponding intensity distribution based on the sinusoidal assumption, $I_i^R(z)$, can be expressed using a *cosine* function as

$$I_i^R(z) = 1 + \cos\left[\frac{2\pi}{g/\tan\alpha}\left\{z + \left(\frac{g}{4\tan\alpha}\right)(i-1)\right\}\right] \quad , \quad i = 0, 1, 2, 3 \tag{5.2}$$

By substituting Eq. 5.1 and 5.2 into Eq. 1.12, the phase values can be calculated as

$$\phi^S(x,y) = \arctan\left[\frac{I_4^S(x,y) - I_2^S(x,y)}{I_1^S(x,y) - I_3^S(x,y)}\right] \tag{5.3}$$

$$\phi^R(x,y) = \arctan\left[\frac{I_4^R(x,y) - I_2^R(x,y)}{I_1^R(x,y) - I_3^R(x,y)}\right] \tag{5.4}$$

The phase error from the sinusoidal assumption can be defined as

$$\text{Error} = \phi^S(x,y) - \phi^R(x,y) \tag{5.5}$$

The error in fractional fringe order, e_N , can be expressed as

$$e_N = \frac{1}{2\pi}\left(\phi^S(x,y) - \phi^R(x,y)\right) \tag{5.6}$$

The fractional fringe errors were determined numerically for two high sensitivity shadow moiré configurations; (Configuration 1) g = 0.1 mm, α = 63°, $\lambda_c = 550$ nm, $\Delta\lambda = 300$ nm and (Configuration 2) g = 0.2 mm, α = 45°, $\lambda_c = 550$ nm, $\Delta\lambda = 300$ nm. The results are plotted in Figs. 5.1 and 5.2 for the first and second configurations, respectively. In each figure, the plots show the error over a small region near (a) the zero Talbot distance (z/D_T^α = 0 – 0.2) and (b) half the Talbot distance (z/D_T^α = 0.4 – 0.6), respectively.

The errors change cyclically and its frequency is much larger than D_T^α. It is worth noting that the amplitude does not change regardless of the optical configuration

although the frequency becomes higher with a configuration with higher sensitivity (Configuration 1). The amplitude of the error is around ± 0.017 fringe near the zero Talbot distance and around ± 0.003 fringe near half the Talbot distance, which is only 1/5 of the error near the zero Talbot distance.

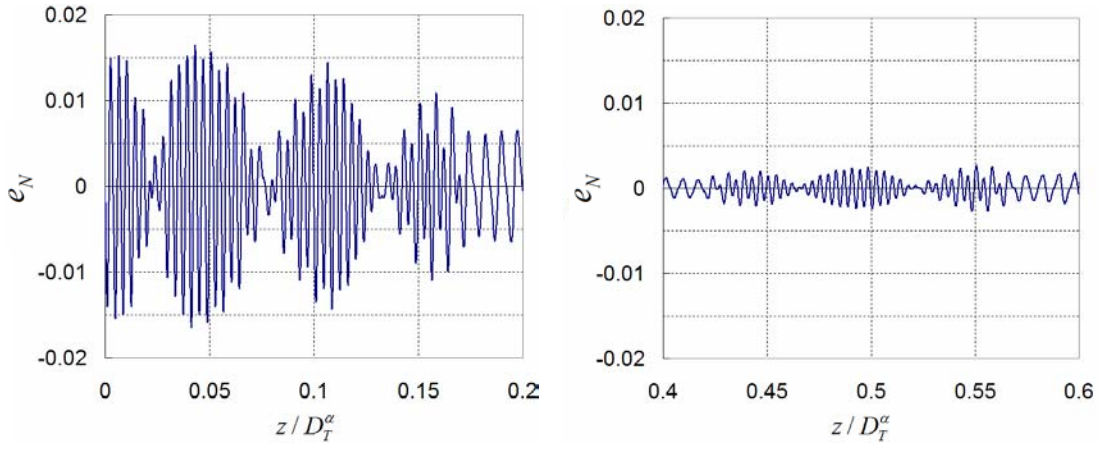

(a) (b)

Figure 5.1 Phase-shifting error of shadow moiré fringe with $g = 0.1$, $\alpha = 63°$, $d_e = 0$ and $\lambda = 400 – 700$ nm for regions near (a) the zero Talbot distance ($z/D_T^\alpha = 0 – 0.2$) and (b) half the Talbot distance ($z/D_T^\alpha = 0.4 – 0.6$).

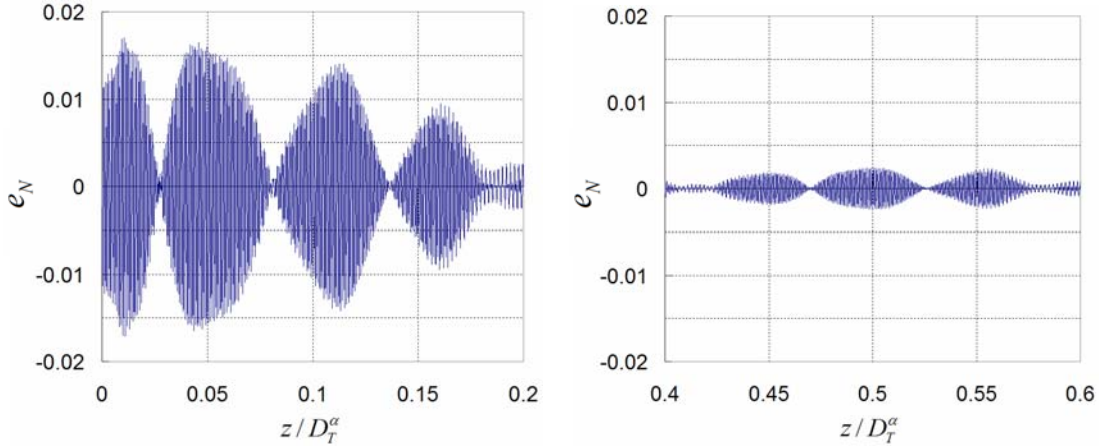

(a) (b)

Figure 5.2 Phase-shifting error of shadow moiré fringe with $g = 0.2$, $\alpha = 45°$, $d_e = 0$ and $\lambda = 400 – 700$ nm for regions near (a) the zero Talbot distance ($z/D_T^\alpha = 0 – 0.2$) and (b) half the Talbot distance ($z/D_T^\alpha = 0.4 – 0.6$).

The much reduced error near half the Talbot distance can be explained by further investigating the intensity function of Eq. 4.12. The intensity function is plotted in Figure 5.3 for the optical setup of g = 0.1 mm, α = 63°, $\lambda_c = 550$ nm and $\Delta\lambda = 300$ nm. A pin-hole aperture was assumed. The intensity is plotted over (a) one Talbot distance, (b) near the zero Talbot distance, and (c) near half the Talbot distance. It is clear from (b) and (c) that the intensity distribution near the zero Talbot distance deviates from sinusoidal function more significantly than near half the Talbot distance.

Each harmonic term in Eq. 4.12 contributes to the final intensity distribution. The individual terms corresponding to n = 1, 2, and 3 in Eq. 4.12 are plotted in Fig. 5.4 (a), (b), and (c), respectively. It is clear from the figures that the contributions of the higher order terms are localized only near the zero Talbot distance and diminished rapidly as z increase. Near half the Talbot distance, the contribution of higher order terms is trivial because of the *sinc* function in Eq. 4.12, which is extremely sensitive to $\Delta\lambda$.

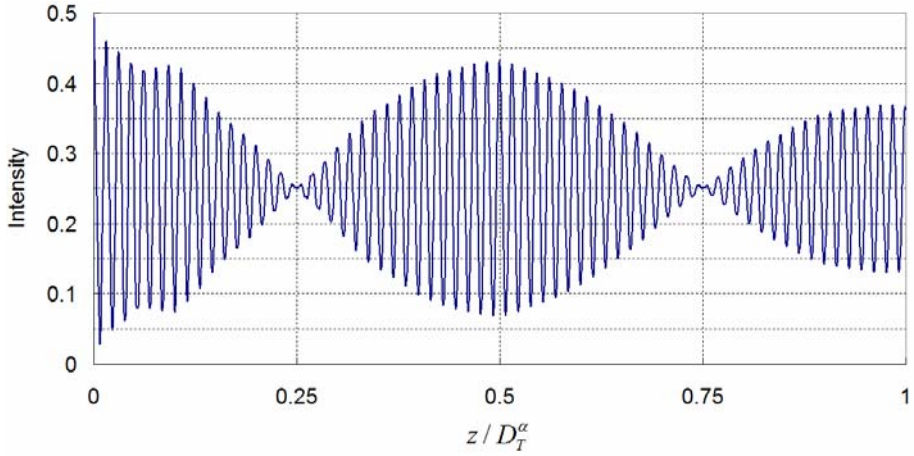

(a)

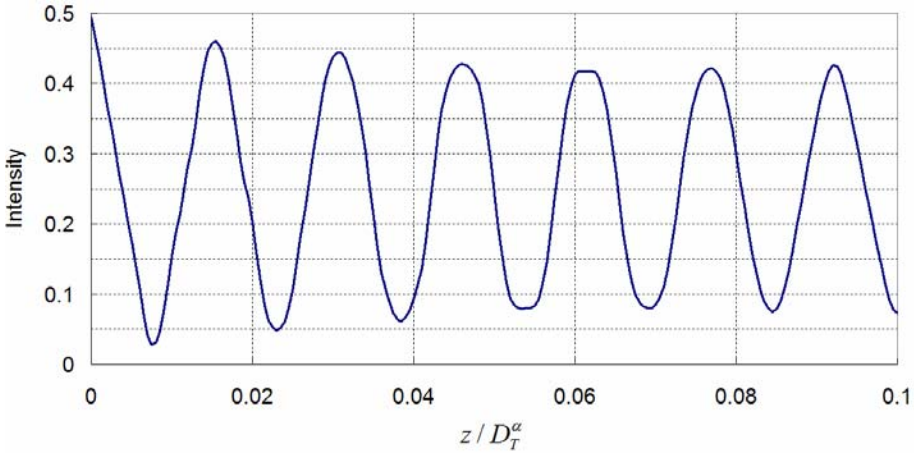

(b)

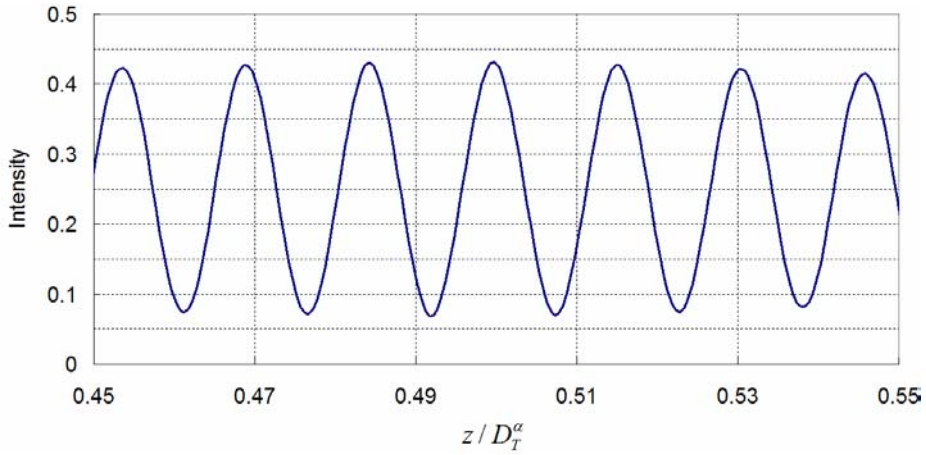

(c)

Figure 5.3 Intensity distribution of shadow moiré fringe for $g = 0.1$, $\alpha = 63°$, and $\lambda =$ 400 – 700 nm with z/ D_T^{α} = (a) 0 – 1, (b) 0.0 – 0.1, and (c) 0.45 – 0.55.

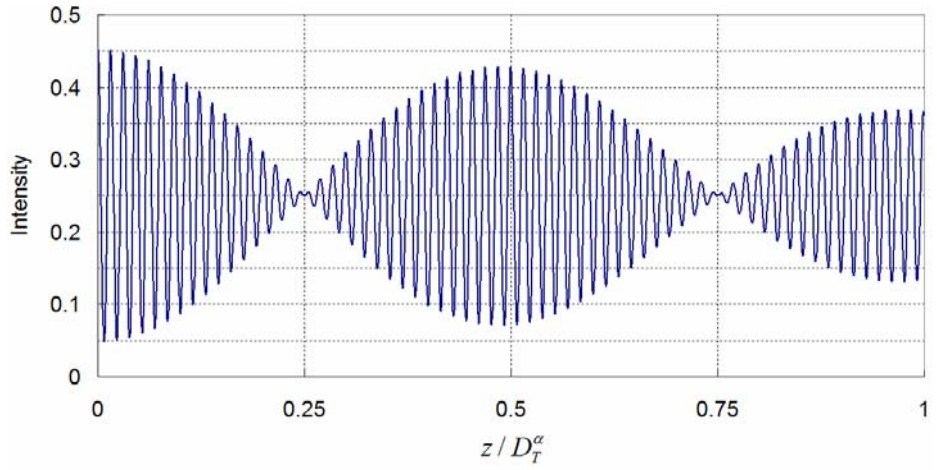

(a)

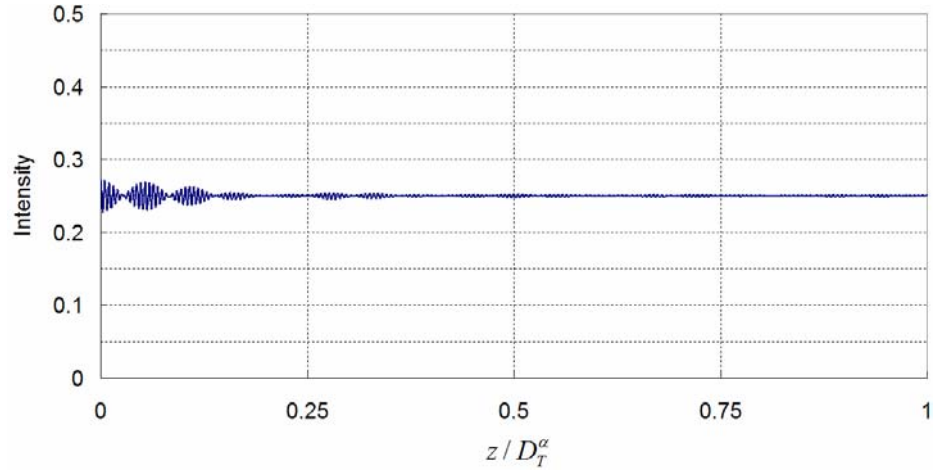

(b)

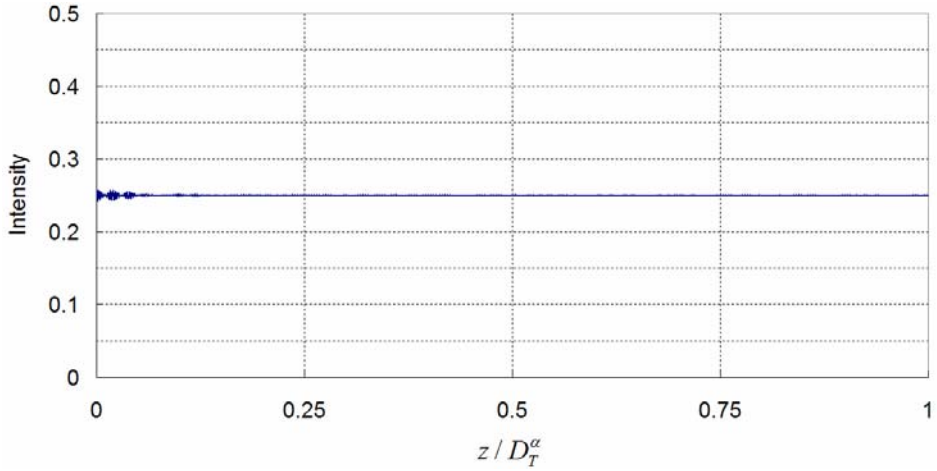

(c)

Figure 5.4 Contribution of each order (n) on the intensity function for the configuration of g = 0.1, α= 63°, and λ = 400 – 700 nm; n = (a) 1, (b) 2, and (c) 3.

It is instructive to analyze the case of a monochromatic light. With a monochromatic light $(\Delta\lambda = 0)$, the effect of *sinc* function diminishes completely and thus the reduction of the error at half the Talbot distance would not be possible. The phase shift error was calculated for a monochromatic light, where Eqs. 2.8 and 2.9 were used to describe the intensity distribution and the same optical configuration used to produce Fig. 5.1 was used. The results are shown in the Fig. 5.5. As expected, the phase errors near half the Talbot distance are as significant as those near the zero Talbot distance.

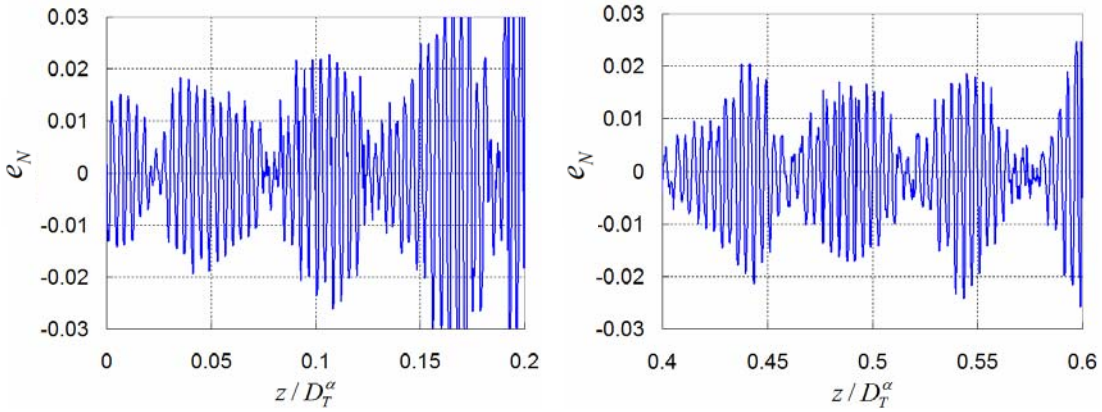

(a) (b)

Figure 5.5 Phase-shifting error of shadow moiré fringe with monochromatic light (λ = 550 nm), g = 0.1, α = 63°, and d_e = 0 for regions near (a) the zero Talbot distance (z/D_T^α = 0 – 0.2) and (b) half the Talbot distance (z/D_T^α = 0.4 – 0.6).

5.1.2 Effect of Aperture on Phase-shifting Error

In the previous chapter, the phase-shifting errors were determined with a pin-hole aperture. Recalling that a finite aperture changes the fringe contrast, the aperture size can affect the phase-shifting errors.

Janssens et al. [Janssens 1985] and Ladak et al. [Ladak 2000] analyzed the effect of aperture on the fringe contrast and associated phase-shifting errors. Since the exact expression of shadow moiré fringes were not available, they assumed a sinusoidal function to represent shadow moiré fringes. The similar approach is repeated here to analyze the effect of the aperture but using the true mathematical expression derived in the previous chapter. The intensity distribution of shadow moiré with finite aperture can be written as

$$I_s(z) = \frac{1}{4} + \sum_{n=1}^{\infty} \frac{2}{\pi^2 (2n-1)^2} \left(1 - \frac{8 d_e z}{3\pi g}\right) \cos\left\{\frac{2\pi z (2n-1)^2}{D_T^{\alpha}}\right\} \times \cos\left\{\frac{2\pi z (2n-1)}{g / \tan\alpha}\right\} \operatorname{sinc}\left\{\frac{2z(2n-1)^2}{D_{T,secondary}^{\alpha}}\right\} \tag{5.7}$$

where the equation is valid only for $0 \le z \le D_W$. Beyond the wash-out distance, the intensity remains a constant of 0.25. After substituting Eq. 5.7 into Eq. 1.11, the procedure used to calculate the phase errors for the case of the pin-hole aperture was repeated.

The effective aperture can be expressed in terms of f-number (*f/#*) and magnification as

$$d_e = \frac{d}{L} = \frac{f/(f/\#)}{f(M+1)/M} = \frac{M}{(M+1)(f/\#)} \tag{5.8}$$

where M is magnification factor and f is focal length of the imaging system.

Numerical calculations were performed for the identical optical setup used in the previous chapter: g = 0.1 mm, α = 63°, $\lambda_c = 550$ nm and $\Delta\lambda = 300$ nm. A magnification factor of 0.2 was assumed, which offers a viewing area of 50 mm when a 1" format CCD camera is used (sensing area of 10 mm). The phase-shifting errors were determined for two effective apertures of 0.01 and 0.03; these two apertures correspond to f/# of 16 and 5.5 for the given magnification factor.

The washout distances of the two apertures are 3.6 and 1.2 times of each D_T^{α}. The results are shown at Fig. 5.6 and 5.7. The results are very similar to Fig. 5.1. More important, however, the phase errors remain virtually unchanged in spite of three time increase in the effective aperture. It is clear from the results that the amplitude of the phase errors produced by the aperture effect is ignorable compared with that produced by the non-sinusoidal intensity.

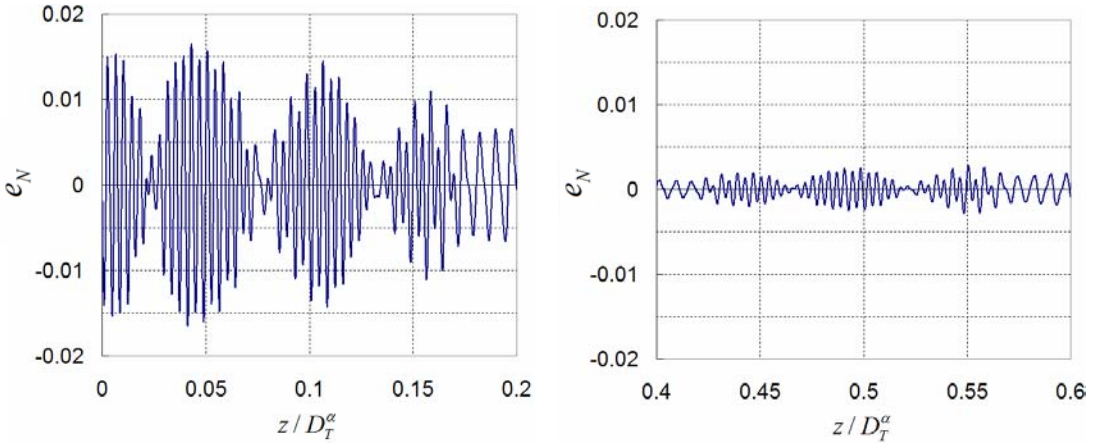

(a) (b)

Figure 5.6 Phase shifting error of shadow moiré fringe with $g = 0.1$, $\alpha = 63°$, $d_e = 0.01$ and $\lambda = 400 – 700$ nm for regions near (a) the zero Talbot distance ($z/D_T^\alpha = 0 – 0.2$) and (b) half the Talbot distance ($z/D_T^\alpha = 0.4 – 0.6$).

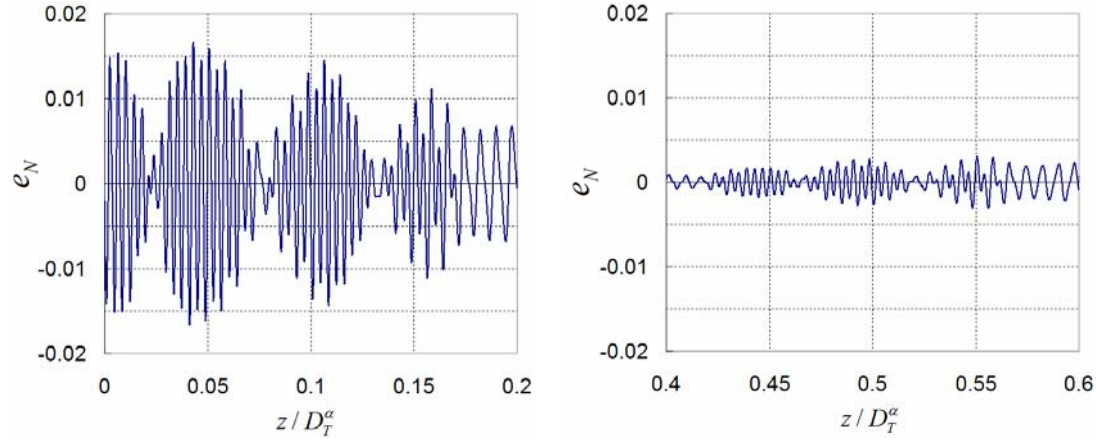

(a) (b)

Figure 5.7 Phase shifting error of shadow moiré fringe with $g = 0.1$, $\alpha = 63°$, $d_e = 0.03$ and $\lambda = 400 – 700$ nm for regions near (a) the zero Talbot distance ($z/D_T^\alpha = 0 – 0.2$) and (b) half the Talbot distance ($z/D_T^\alpha = 0.4 – 0.6$).

5.1.3 Experimental Verification of Phase-shifting Error

The error defined by Eq. 5.6 was verified experimentally. The optical setup used for verification is illustrated in Fig. 5.8a, where g = 1 mm and $\alpha = 45°$. The 250 W white light illuminator used in the previous experiment was employed as a light source. The setup produces a contour interval of 1 mm per fringe. The magnitude of e_N is independent of the contour interval, and thus the absolute displacement error, defined as e_N multiplied by the contour interval, increases as the contour interval increase, e.g., for $e_N = \pm 0.01$, the errors in displacements are ±1 μm and ±10 μm for contour intervals of 100 μm and 1 mm, respectively. The large contour interval helps distinguish the phase shifting error from the other experimental errors.

An optical flat 58 mm × 58 mm with a surface accuracy of ¼ λ was coated with white spray paint. The optical flat provided an ideal flat surface to be used as a reference. The optical flat was viewed by a high resolution CCD camera (Pulnix TM-1040). An adjustable circular aperture with diameter of 2 mm was inserted between the camera and the grating. The focal length of the imaging lens was 40 mm. The distance between the specimen and the aperture, L, was set to be 758 mm, which produced the effective aperture (d_e) of 0.003 and a magnification factor of 0.044.

The optical flat was positioned initially at 0.01 D_T^{α} (13 mm from the reference grating) and it was tilted slightly to produce rigid-body displacements. The fringe pattern was captured by the camera and it is shown in Fig. 5.8b. The pitch of the reference grating was coarse and its image was resolved by the camera, which

reduced fringe visibility significantly. To cope with the problem, the reference grating was translated in its plane perpendicular to the direction of the grating lines during exposure [Post 1994]. Translation of the reference grating has no influence on the positions of moiré fringes but the grating bars are smeared and become invisible because of their motion faster than exposure time. Desired translation was accomplished by using a precision ball-screw actuator (THK model KR2001A+100) controlled by a high precision stepper motor and controller (Parker Compumotor model zeta 6104). The resultant fringe pattern is shown in Fig. 5.9 (a). Improvement of fringe visibility is evident.

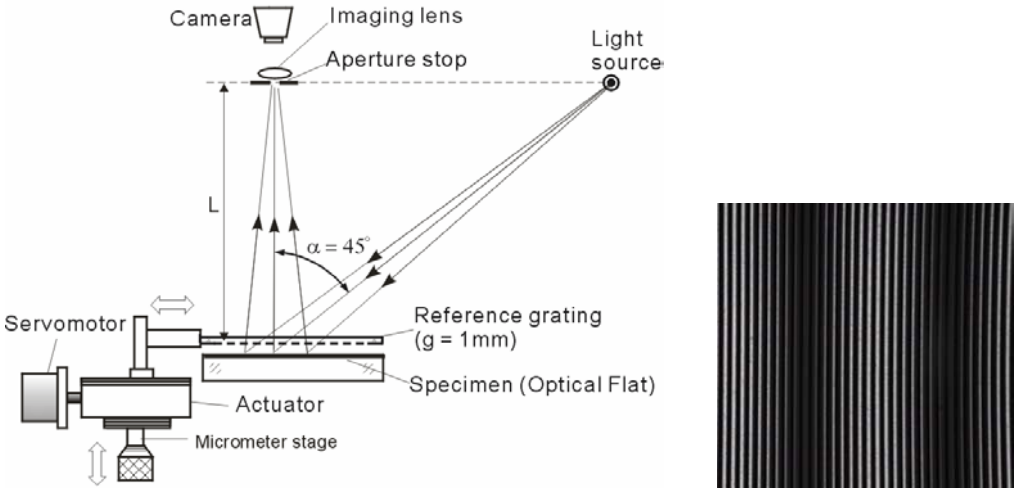

(a) (b)

Figure 5.8 Experimental setup to verify the error from non-sinusodial intensity distribution; (a) optical setup of shadow moiré, (b) fringe papttern of the specimen.

The reference grating was also mounted to a high precision micrometer stage in such a way that the reference grating was translated normal to the optical flat. The fringes obtained by a shifting interval of 0.25 mm are shown in Figs. 5.9(b)-(d).

The fringe patterns were analyzed by a phase-shifting software. The resultant unwrapped phase map is shown in (e). The displacement along a line A-A is shown in (f). The optical flat had only rigid-body-displacement, which would produce a linear change in displacements along A-A. Deviation of the line in (f) from the straight line was caused by the non-sinusoidal intensity distribution.

In order to visualize the errors more effectively, the rigid-body displacements were subtracted mathematically by adding a linear displacement function. The errors are clearly seen in Fig. 5.9 (g). The errors obtained from the experiment were compared with the numerical predictions in (h). The magnitude and period of the experimental errors match well to the prediction, which confirms the validity of Eq. 5.6.

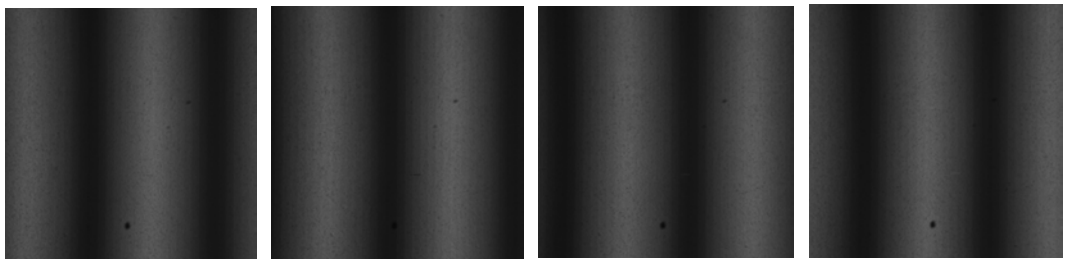

(a) (b) (c) (d)

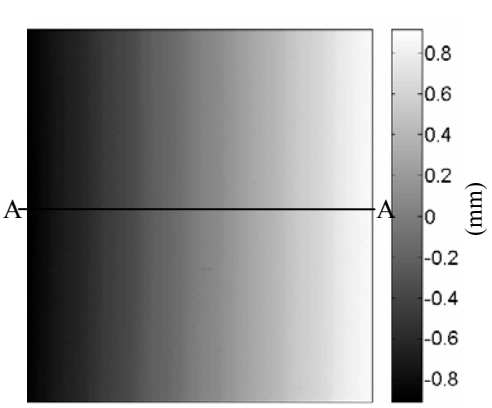

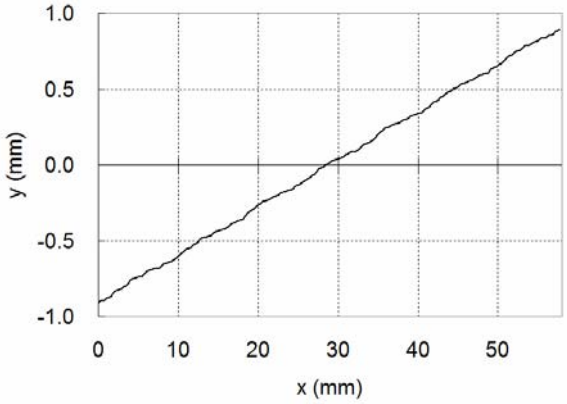

(e) (f)

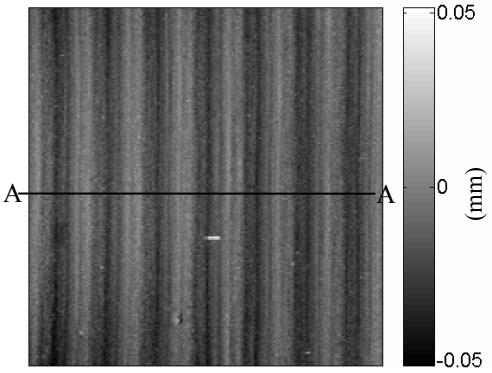

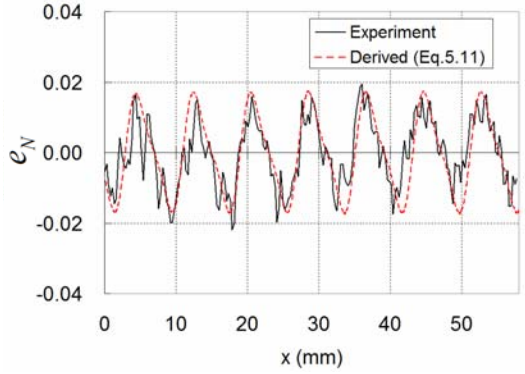

(g) (h)

Figure 5.9 Experimental results with a contour interval of 1 mm; (a) 0, (b) π/4, (c) π/2, (d) 3π/4 shifted image, (e) deformation plot, (f) displacement along A-A, (g) error plot, and (h) the error along A-A is compared with the theoretical value.

5.1.4 Maximum Phase-shifting Error

The analysis in the previous section indicates that the maximum systematic error from the non-sinusoidal fringe intensity distribution of shadow moiré is approximately ± 1.7 % of the contour interval, which provides a theoretical limit of the minimum fractional fringe order that can be determined by the phase-shifting method as $\frac{1.7}{100} \approx \frac{1}{60}$. Figure 5.10 shows the maximum phase-shifting error as a function of contour interval. The results clearly indicate that high basic measurement sensitivity is desired for high precision even when the phase-shifting is employed.

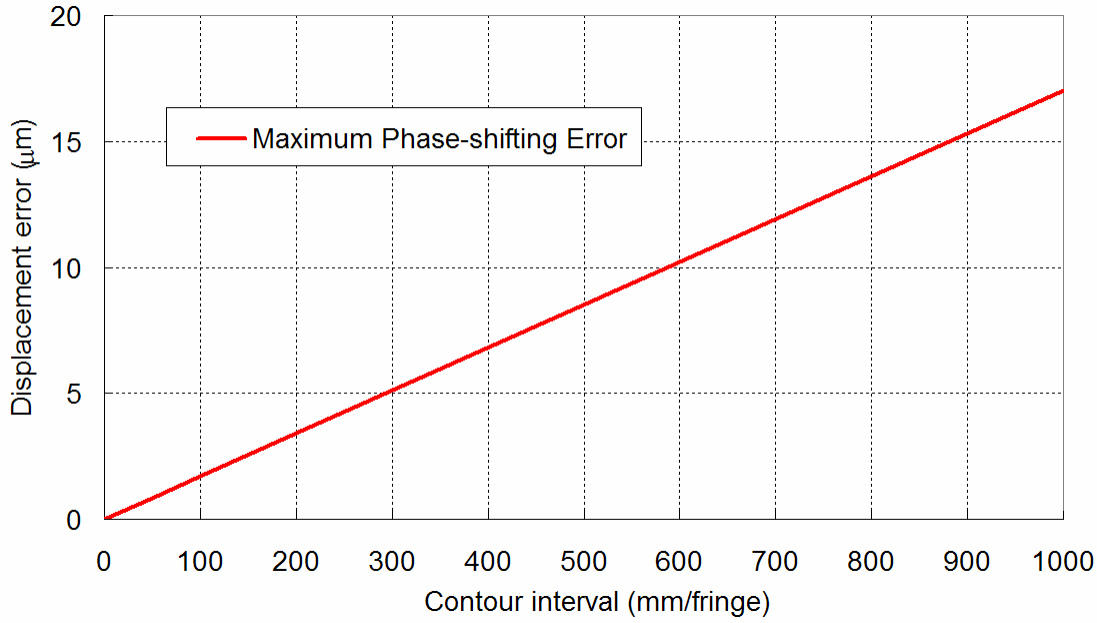

Figure 5.10 Maximum phase-shifting errors as a function of contour interval.

5.2 Shadow Moiré Using Non-zero Talbot Distance (SM-NT)

5.2.1 Extension of Theoretical Limit

For the configuration of high sensitivity shadow moiré, the Talbot distance is so small that the contrast of fringe diminishes rapidly and thus the dynamic range of measurement is limited.

The limited dynamic range is demonstrated in Fig. 5.11. An optical setup of high sensitivity shadow moiré is shown in Fig. 5.11 (a), which provides a contour interval of 50 μm/fringe with g = 0.1 mm, $\alpha = 63°$, and d_e = 0.01. The Talbot distance of the setup is 3.25 mm. An optical flat was tilted to produce a linearly varying displacement field. The combined contrast function, or Eq. 4.16, is drawn in Fig. 5.11 (b) and the obtained fringe pattern from the setup is shown in Fig. 5.11 (c). Due to the Talbot effect, the fringe contrast reduces abruptly and becomes zero at the quarter Talbot distance. The fringe contrast increases again until z reaches half the Talbot distance.

The results clearly indicate that the dynamic range is limited by the Talbot distance. If the specimen is placed at 0.5 mm from the grating, only a few fringes can be visible in the zero Talbot area. But if the specimen is placed in the half Talbot area, the dynamic range can be increased significantly. This is one of the important motivations to propose shadow moiré using non-zero Talbot distance.

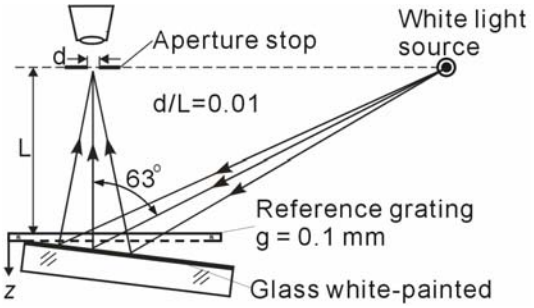

(a)

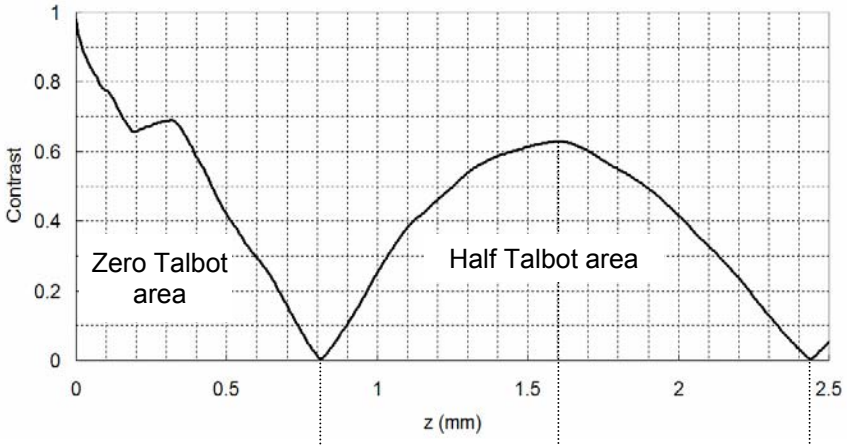

(b)

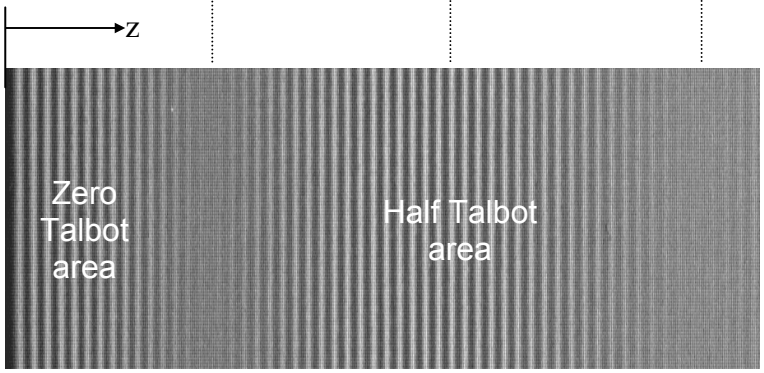

(c)

Figure 5.11 Demonstration of the dynamic range in half the Talbot distance; (a) shadow moiré setup, (b) theoretical fringe contrast, and (c) the fringe pattern representing linearly varying displacements.

5.2.2 Maximum Talbot Distance and Critical Angle

Repeated here, the Talbot distance (D_T^α) and the contour interval (Γ) of shadow moiré are defined as

$$D_T^\alpha = \frac{2g^2}{\lambda}\cos^3\alpha \tag{1.5}$$

$$\Gamma = \frac{g}{\tan\alpha} \tag{3.5}$$

where g is the grating pitch, λ is the wavelength, and α is the angle of illumination.

A larger Talbot distance is desired for a larger dynamic range provided that an aperture effect is small. From Eqs. 1.5 and 3.5, the Talbot distance is related to the contour interval as

$$D_T^\alpha = \frac{\Gamma^2}{\lambda}\sin 2\alpha \sin\alpha \tag{5.9}$$

The incident angle that provides the maximum Talbot distance for a given contour interval can be calculated by differentiating Eq. 5.9 as

$$\frac{\partial D_T^\alpha}{\partial \alpha} = \frac{\Gamma^2}{\lambda}\frac{\partial\left(\sin 2\alpha \sin\alpha\right)}{\partial\alpha} = \frac{\Gamma^2}{\lambda} 2\sin\alpha\left(3\cos^2\alpha - 1\right) = 0 \tag{5.10}$$

The value of α that satisfies Eq. 5.10 is $\alpha_c = 54.7^\circ$, which will be referred to as *critical angle*. Figure 5.12 shows the maximum Talbot distance and the

corresponding pitch of grating for the contour interval of (a) 100 μm/fringe and (b) 50 μm/fringe.

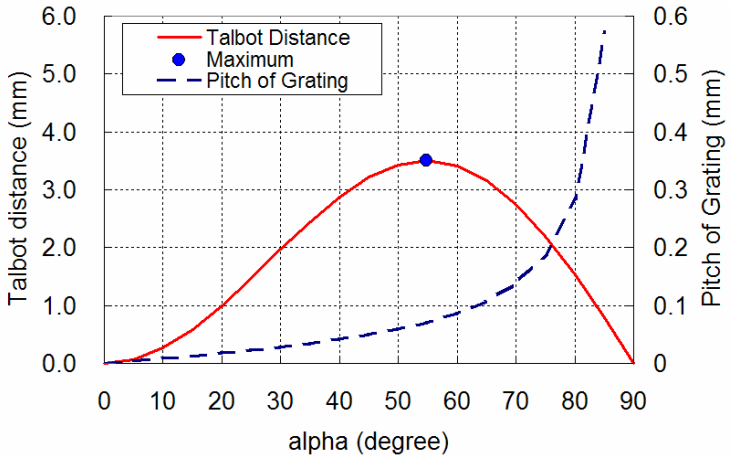

(a)

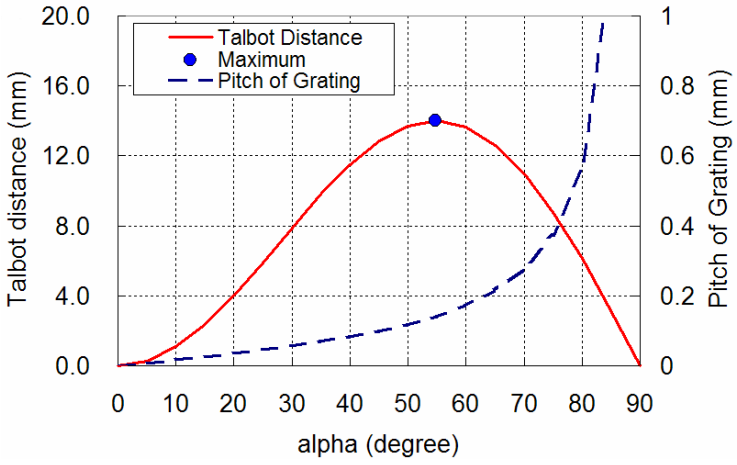

(b)

Figure 5.12 Maximum Talbot distance and grating pitch for the contour interval of (a) 100 μm/fringe and (b) 50 μm/fringe.

5.2.3 Enhancement of Dynamic Range

Enhancement of the dynamic range in the half Talbot area is demonstrated in Tables 5.1 and 5.2. The following criteria were used to determine the parameters in Table 5.1.

(1) Minimum gap between the specimen and the reference grating: 1 mm

(2) Minimum dynamic range = 10 contour interval

(3) Additional range for good contrast = 1 mm + 10 contour interval.

(4) Required quarter Talbot distance = (1) + (2) + (3)

The item (3) is needed to ensure reasonable contrast of all the fringes within the dynamic range. It is to be noted that the quarter Talbot distance was calculated using the critical angle. As can be seen from the table, the required quarter Talbot distance is greater than the maximum quarter Talbot distance except a contour interval of 200 μm.

The required half Talbot distance was also calculated for the half Talbot area. In this case, the criteria become:

(1) Minimum gap between the specimen and the reference grating: 1 mm

(2) Minimum dynamic range = 10 contour interval

(3) Additional range for good contrast = ±5 contour interval.

(4) Required half Talbot distance = maximum((1) + (2)/2, (2) + (3))

The results are shown in Table 5.2. The required half Talbot distance is smaller than the maximum value even for the contour interval of 50 μm.

Table 5.1 Utilizing the zero Talbot area for high sensitivity shadow moiré

Contour interval (μm/fringe)	Required Dynamic Range (mm)*	Required Quarter Talbot Distance (mm)**	Maximum Quarter Talbot Distance (mm)***
200	2	6	14
100	1	4	3.5
50	0.5	3	0.9

* Required dynamic range = 10 × contour interval

** Required quarter Talbot distance = (1mm + dynamic range) × 2

*** Quarter Talbot distance is calculated using the critical angle.

Table 5.2 Utilizing the half Talbot area for high sensitivity shadow moiré

Contour interval (mm/fringe)	Required Dynamic Range (mm)*	Required half Talbot Distance (mm)**	Maximum Half Talbot Distance (mm)***
100	1	2	7
50	0.5	1.25	1.8

* Required dynamic range = 10 × contour interval

** Required half Talbot distance = maximum (1mm + dynamic range/2, dynamic range × 2)

*** Half Talbot distance is calculated using the critical angle.

Using the dynamic range defined in Tables 5.1 and 5.2, extension of shadow moiré into a higher sensitivity domain is illustrated graphically in Fig. 5.13. In the figure, the dashed line represents the maximum possible Talbot distance for a given contour interval, the dashed-dot line represents the required Talbot distance when the zero Talbot area is utilized, and the solid line denotes the required Talbot distance when the half Talbot area is utilized. In the conventional practice of shadow moiré where only the zero Talbot area is utilized, the required Talbot distance is greater than the maximum Talbot distance if a contour interval is lower than 110 μm per fringe. Utilizing the non-zero Talbot distance, however, the sensitivity of shadow moiré can be extended to 45 μm per fringe.

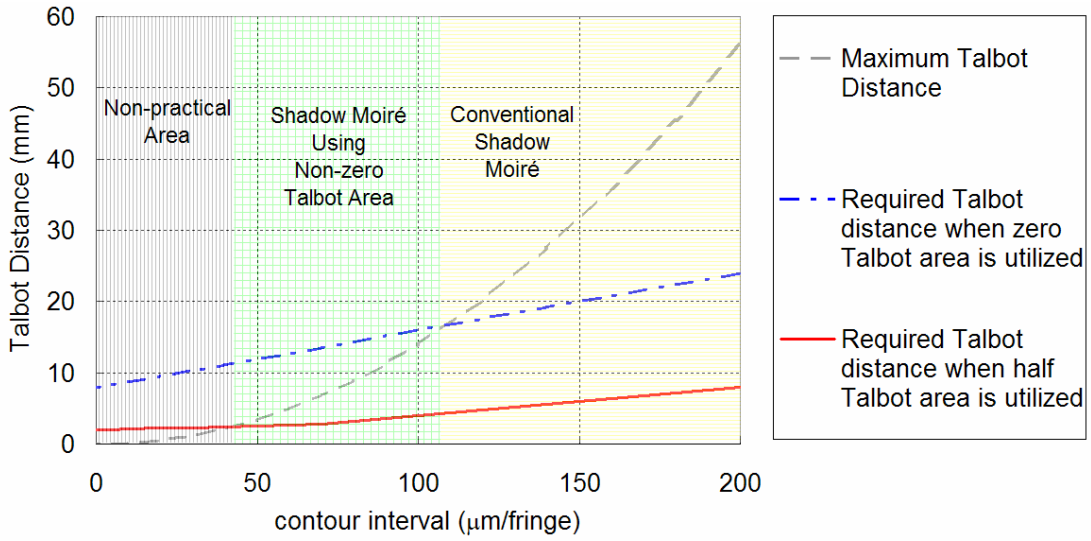

Figure 5.13 Graphical representation of the extension of shadow moiré sensitivity by utilizing the non-zero Talbot distance.

5.2.4 Maximum Sensitivity of SM-NT

The maximum basic measurement sensitivity of shadow moiré can be determined considering (1) the phase-shifting error from the non-sinusoidal fringe intensity distribution and (2) the limit from the Talbot distance requirement. As shown in Fig. 5.14, a SM-NT system with the contour interval of 50 μm per fringe satisfies the criterion of the dynamic range while providing the high measurement resolution less than ±1 μm.

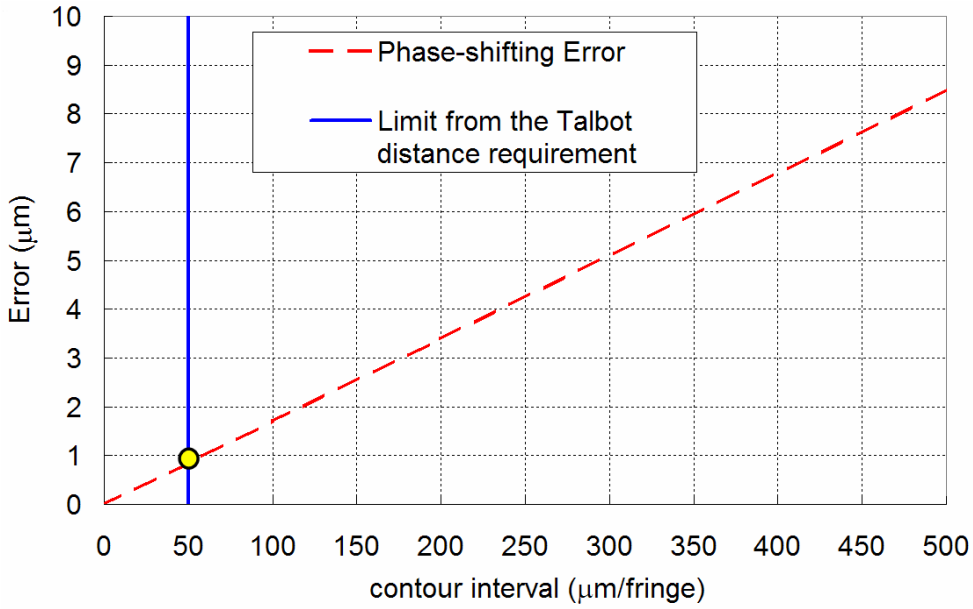

Figure 5.14 Sensitivity selection of shadow moiré using non-zero Talbot distance.

Although it is possible to achieve a larger dynamic range by utilizing half the Talbot distance, the contrast of fringe may be sacrificed substantially due to the aperture effect. An optimization process is required to maximize the dynamic range and the fringe contrast at half the Talbot distance.

5.3 Optical Configuration for Optimal Contrast for SM-NT

From Eqs. 1.5, 3.2, and 3.5, the Talbot distance and the washout distance are related to the contour interval as

$$D_T^{\alpha} = \frac{\Gamma^2}{\lambda} \sin 2\alpha \sin \alpha \tag{5.9}$$

$$D_W = \frac{3\pi}{8} \frac{\Gamma}{d_e} \tan \alpha \tag{5.11}$$

where Γ is the contour interval, λ is the wavelength of the light, α is the angle of illumination, and d_e is the relative aperture.

Recalling the contrast defined in Chap 3,

$$C(z) = C_T(z) \times C_A(z) \tag{3.4}$$

The contrast of shadow moiré at half the Talbot distance can be expressed as

$$\begin{aligned} C\left(D_T^{\alpha}/2\right) &= C_T\left(D_T^{\alpha}/2\right) \times \left(1 - \frac{D_T^{\alpha}/2}{D_W}\right) \\ &= C_T\left(D_T^{\alpha}/2\right) \times \left(1 - \frac{\frac{\Gamma^2}{2\lambda}\sin 2\alpha \sin \alpha}{\frac{3\pi}{8}\frac{\Gamma}{d_e}\tan \alpha}\right) \\ &= C_T\left(D_T^{\alpha}/2\right) \times \left(1 - \frac{4\Gamma d_e}{3\pi\lambda} \sin 2\alpha \cos \alpha\right) \end{aligned} \tag{5.12}$$

Considering a practical application with white light, the Talbot contrast at half the Talbot distance, $C_T\left(D_T^{\alpha}/2\right)$, is 0.73 (Eq. 4.16). Then Eq. 5.12 can be written as

$$C\left(D_T^{\alpha}/2\right)=0.73\left(1-\frac{4\Gamma d_e}{3\pi\lambda_c}\sin 2\alpha\cos\alpha\right) \tag{5.13}$$

where λ_c is the mean wavelength.

5.3.1 Optimization with Finite Aperture

Equation 5.13 is the objective function of the contrast optimization for a given contour interval. The variables of the objective function are the angle of illumination, α, and the relative aperture, d_e. The constraints for optimization are defined after considering the following practical parameters:

1) Upper limit of the incident angle: $\tan\alpha \le 3$ (or $\alpha \le 72°$)

   As the angle of incidence increases, the reflection from the reference grating increases significantly [Post 1994]. In addition, the distance between the light source and the specimen increases proportionally to $\tan\alpha$. As a result, light utilization would be too poor to be practical. Angle of 72°, which matches arctan (3), is set to the upper limit of α.

2) Upper and lower bound of the effective aperture: d_e = 0.01 and 0.03

3) Minimum half the Talbot distance: 1.25 mm for 50 μm and 2.0 mm for 100 μm from Table 5.2.

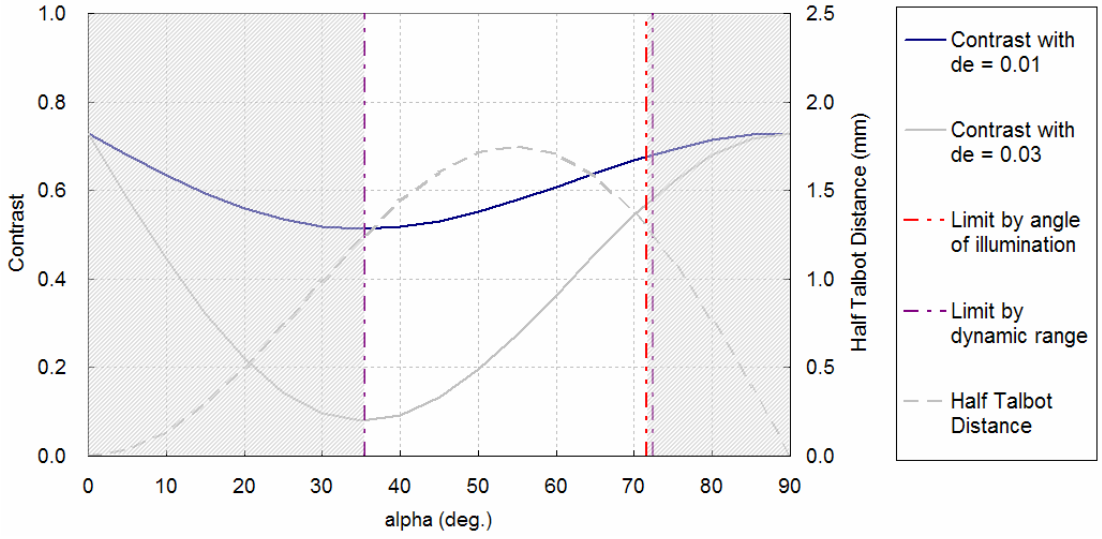

(a)

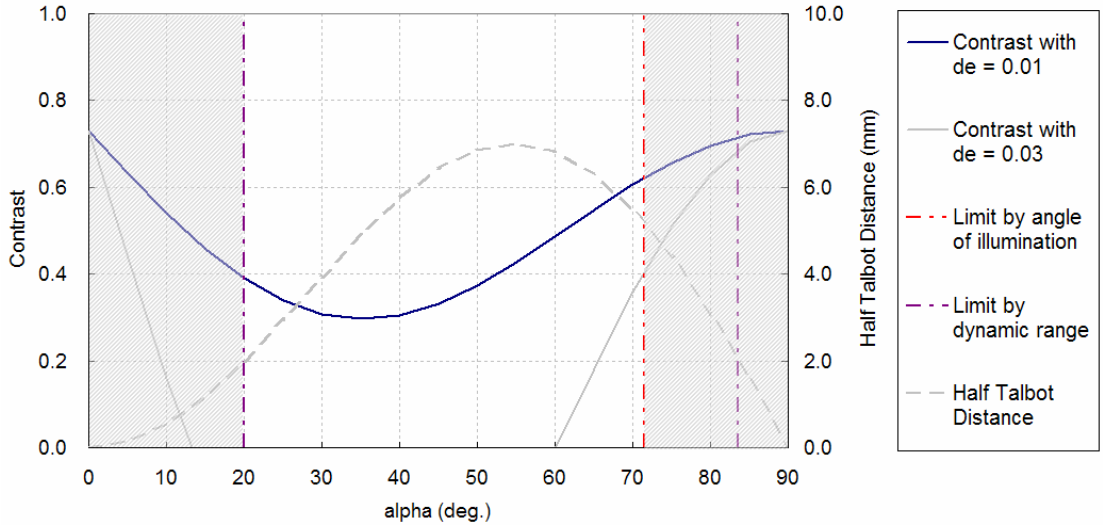

(b)

Figure 5.15 Contrast curve at half the Talbot distance for the contour interval of (a) 50 μm/fringe and (b) 100 μm/fringe.

Figure 5.15 shows the contrast at half the Talbot distance, or Eq. 5.13, using the constraints for two different contour intervals, (a) 50 μm and (b) 100 μm. In the figures, solid black and gray lines represent the contrast for the effective apertures of 0.01 and 0.03, respectively. A dashed line shows half the Talbot distance and a dashed-dot line is obtained from the constraints of the required half Talbot distance; if the angle of illumination is either too large or too small, the required half Talbot distance can be larger than half the Talbot distance. A double dots-dashed line indicates the constraints of illumination angle.

The domain which is limited by any of the constraints is shaded in the figures. By analyzing the non-shaded domain, the following general conclusions can be made:

1) A larger angle of illumination provides a better contrast.
2) The aperture is the most stringent limiting parameter. For example, the non-zero Talbot distance configuration cannot be employed for a configuration with a 100 μm contour interval if an angle of illumination is 45° and the effective aperture is 0.03.

5.4 Implementation of SM-NT

An experiment was conducted to implement the optimized optical configuration. The setup is shown in Fig. 5.16. The specimen was the plano-convex lens (25.0 mm in diameter) and was placed at half the Talbot distance.

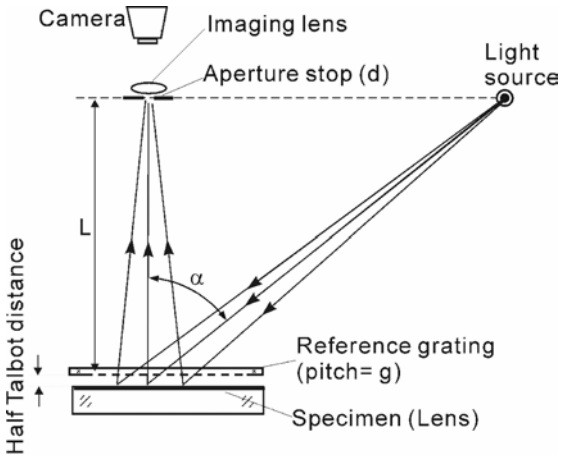

Figure 5.16 Experimental setup to implement the optimization result.

The results obtained for the 50 μm contour interval are plotted in Fig. 5.17 for two configurations; (a) $\alpha = 63°$, $g = 0.1$ mm and (b) $\alpha = 45°$, $g = 0.05$ mm. The effective aperture was 0.01 for both configurations. The two configurations have the same contour interval but it is evident from the fringe patterns that the first configuration offers better contrast at half the Talbot distance. The contrasts were calculated from the fringe patterns and they are compared with the prediction in (c). The experimentally determined contrasts were 0.65 and 0.5, and the corresponding theoretical predictions were 0.64 and 0.53.

The same analysis was conducted for the 100 μm contour interval. The two configurations for the same contour interval were (a) $\alpha = 63°$, $g = 0.2$ mm and (b) $\alpha = 45°$, $g = 0.1$ mm. The results are compared to the prediction in (c). The experimentally determined contrasts were 0.54 and 0.35 and the corresponding theoretical predictions were 0.52 and 0.33.

The experimental results match to the prediction well. The analysis can be used for optimizing shadow moiré systems using non-zero Talbot distance.

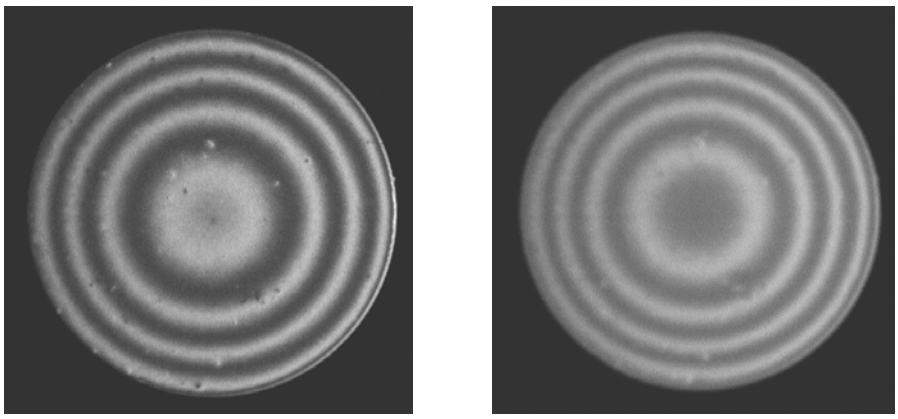

(a) (b)

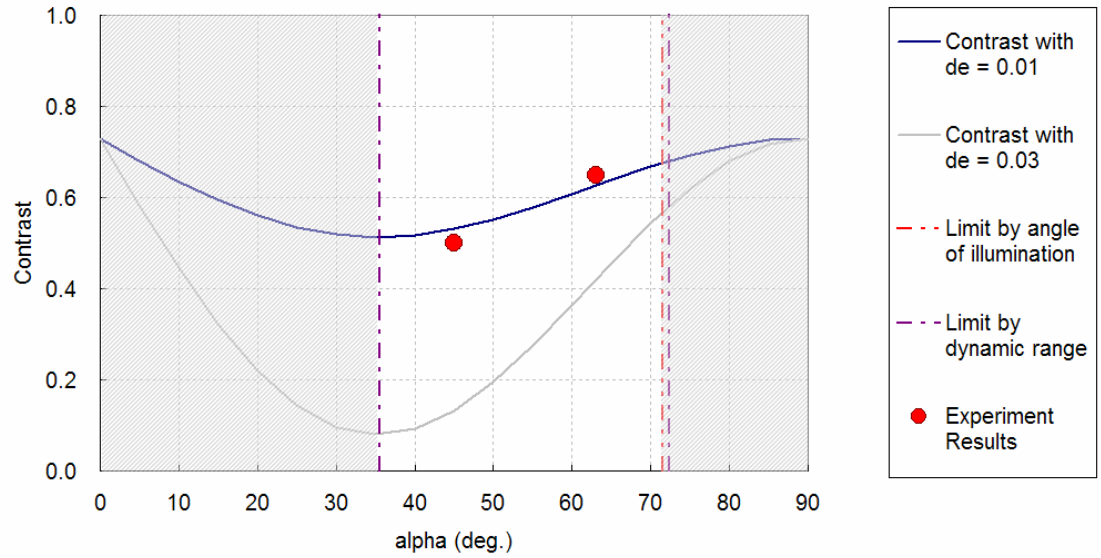

(c)

Figure 5.17 Fringe patterns obtained at half the Talbot distance for the contour interval of 50 μm/fringe; (a) contrast = 0.65 with white light, $\alpha = 63°$, $g = 0.1$ mm, and $d_e = 0.01$, (b) contrast = 0.5 with white light, $\alpha = 45°$, $g = 0.05$ mm, and $d_e = 0.01$, and (c) comparison with the prediction.

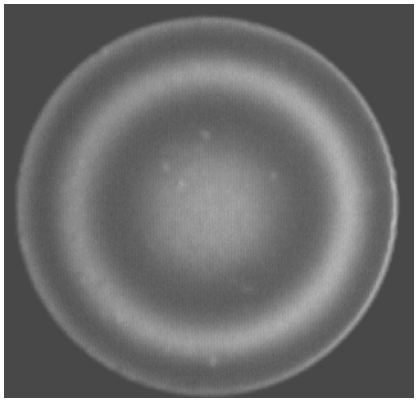

(a)

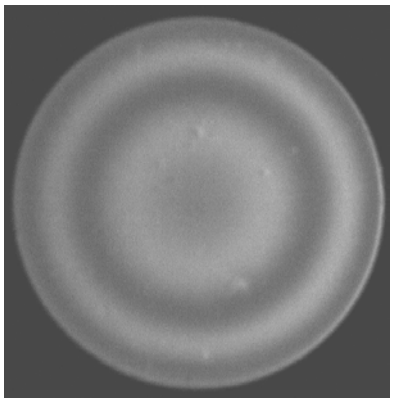

(b)

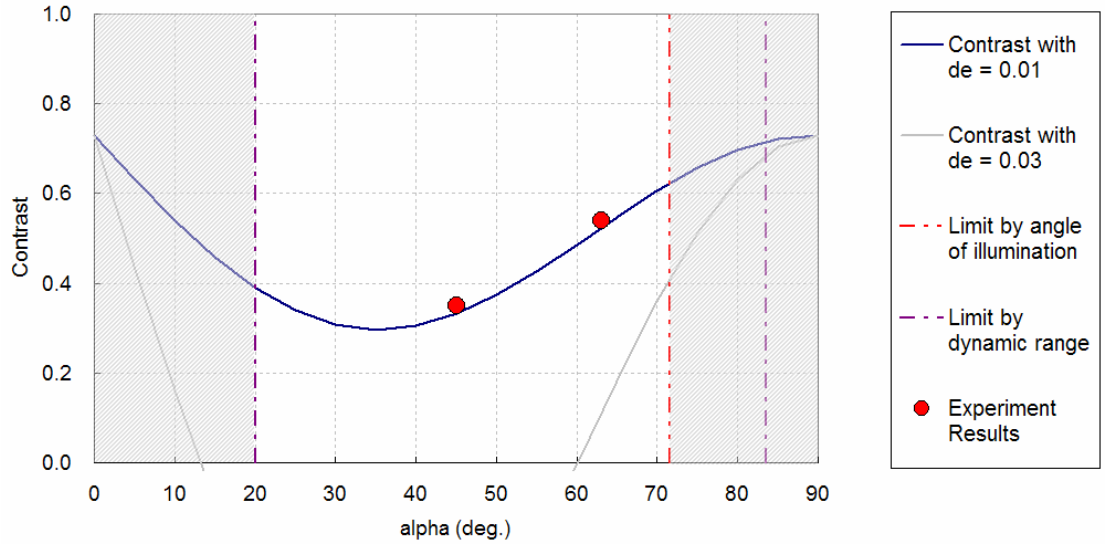

(c)

Figure 5.18 Fringe patterns obtained at half the Talbot distance for the contour interval of 100 μm/fringe; (a) contrast = 0.54 with white light, $\alpha = 63°$, $g = 0.2$ mm, and $d_e = 0.01$, (b) contrast = 0.35 with white light, $\alpha = 45°$, $g = 0.1$ mm, and $d_e = 0.01$, and (c) comparison with the prediction.

5.5 Applications of SM-NT

5.5.1 Warpage Measurement of FC-PBGA Package

The optimized SM-NT system is implemented to measure the warpage of an electronic package. The specimen is a flip-chip plastic ball grid array (FC-PBGA) package. In the package, silicon chips are attached to an organic substrate through tiny solder bumps. The gap between the chip and the substrate is filled with an epoxy underfill to help reduce the thermal stresses induced in the solder bumps. As shown in Fig. 5.19, the size of the package is 54x60 mm^2 and four flip-chips are mounted on the substrate.

The warpage of a FC-PBGA package is attributed to a large mismatch of coefficient of thermal expansion (CTE) between the chip and substrate. In the subsequent assembly process, electrical and mechanical connections are made by solder balls between the substrate and a printed circuit board (PCB). If the bottom side of the substrate warps significantly at the solder reflow temperature, it yields an uneven height of solder interconnections, which could cause premature failure of the assembly. Detailed knowledge of the out-of-plane deformation is essential to optimize design and process parameters for reliable assemblies.

The optimal configuration using a white light source selected in Sec. 5.3 (g = 0.1 mm, α = 63°, d_e = 0.01) was employed to measure the warpage of the back surface of the FC-PBGA package. The Talbot distance of the system was approximately 3.25 mm.

The predicted fringe contrast for the configuration is shown in Fig. 5.20. The warpage of the specimen was measured at the zero Talbot area as well as the half Talbot area.

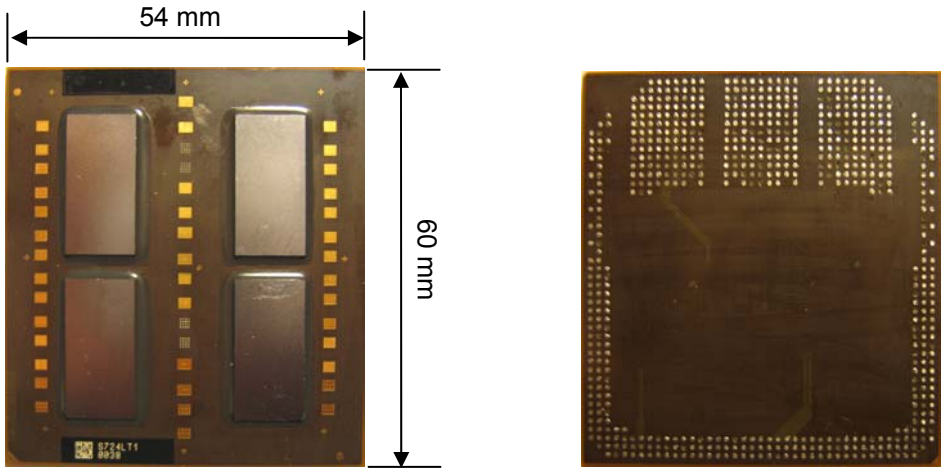

(a) (b)

Figure 5.19 Four chips FC-PBGA package (a) top view and (b) bottom view.

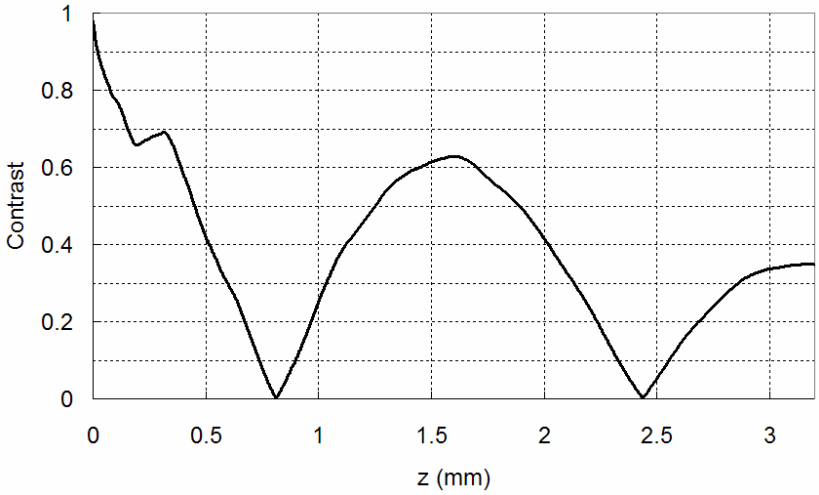

Figure 5.20 Contrast function of SM-NT with white light, g = 0.1mm, α = 63°, and d_e = 0.01.

Fringe patterns obtained at the zero Talbot area are shown in Fig. 5.21(a), where each pattern was obtained with an equal phase-shift of $\pi/4$. The initial gap between the specimen and the reference grating was 0.5 mm. As expected from the contrast plot of Fig. 5.20, the fringes were discernable only at the center and the boundary of the specimen; the fringes near the quarter Talbot distance washed out completely. The unwrapped phase map and the corresponding 3-D plot are shown in (b) and (c), respectively. As a result of the localized contrast loss, the patterns were distorted and could not represent the actual whole-field deformations.

The corresponding results obtained at the half Talbot area are shown in Fig. 5.22. The maximum deformation between the center and the edge of the package was approximately 0.4 mm, which produced 8 fringes between them. In spite of the large dynamic range required for the measurement, the SM-NT system documented the deformations faithfully as evidenced by the excellent contrast of individual fringes. It is to be noted that the small circles on the images are not caused by optical noise. Instead they represent circular copper pads on the substrate.

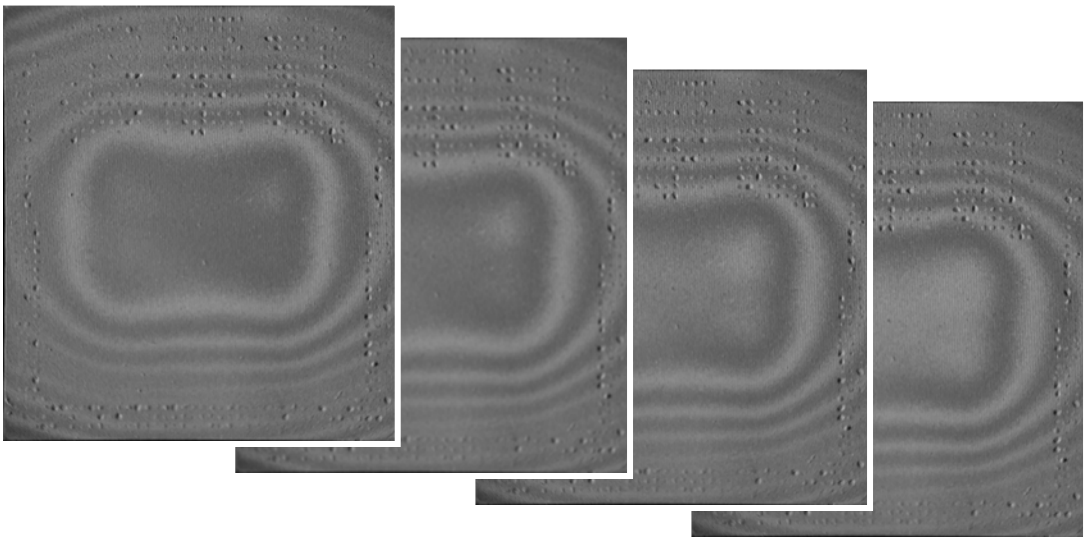

(a)

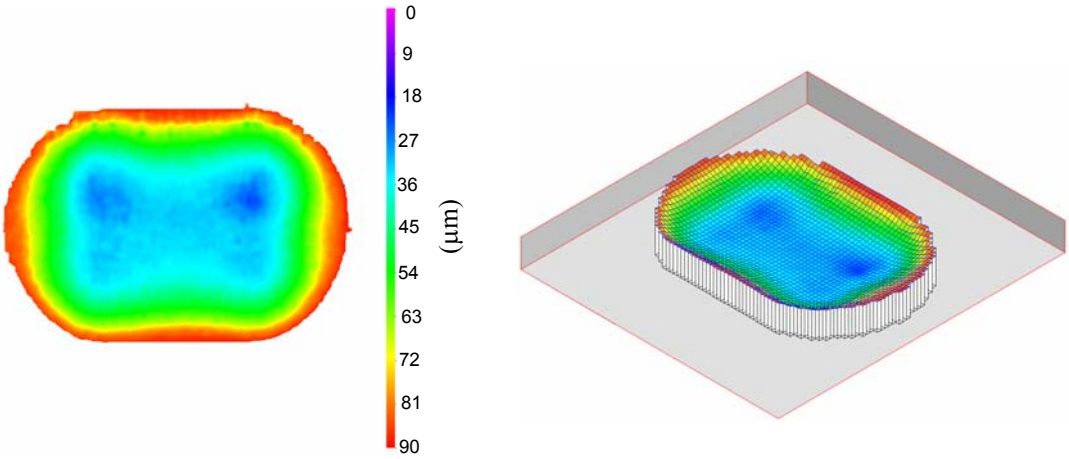

(b) (c)

Figure 5.21 Warpage of FC-PBGA package documented at the zero Talbot area: g = 0.1 mm and $\alpha = 63°$, and $d_e = 0.01$, (a) four phase-shifted images, (b) unwrapped phase map, and (c) 3D deformation plot.

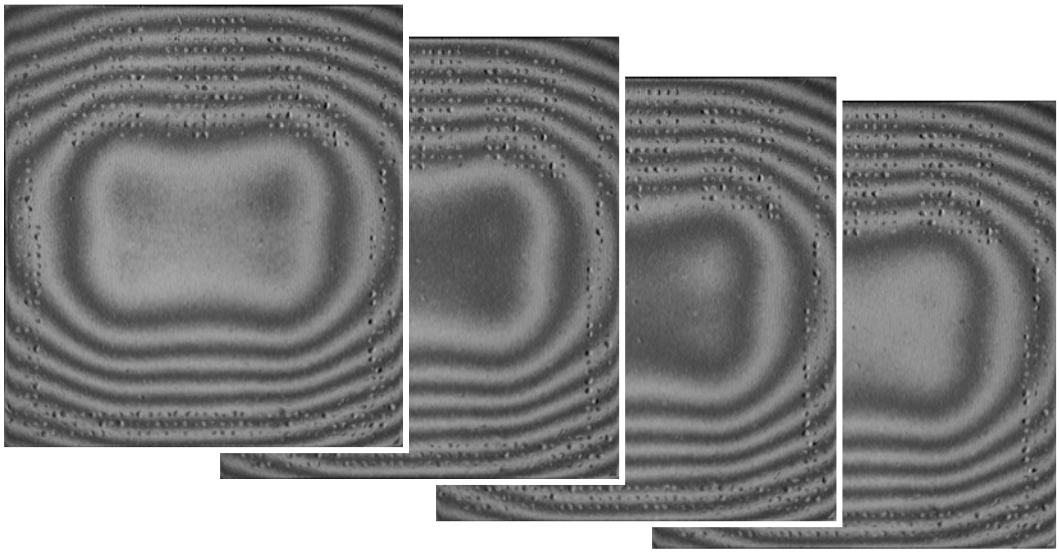

(a)

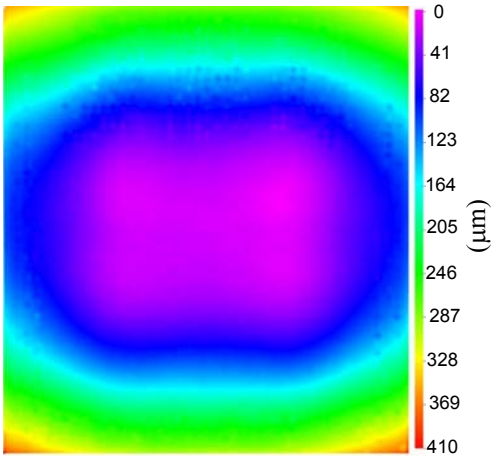

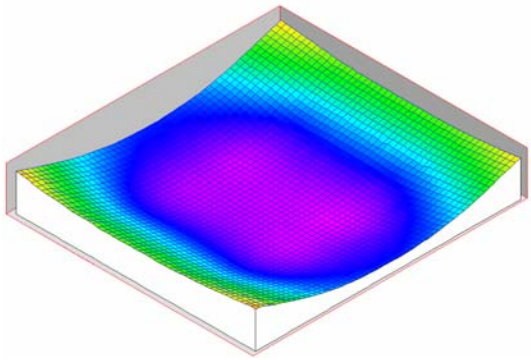

(b) (c)

Figure 5.22 Warpage of FC-PBGA package documented at the half Talbot area: g = 0.1 mm and $\alpha = 63°$, and $d_e = 0.01$, (a) four phase-shifted images, (b) unwrapped phase map, and (c) 3D deformation plot.

5.5.2 Warpage Measurement of Non-coplanar Surfaces

Another FC-PBGA package is shown in Fig. 5.23. In the package, a silicon chip is attached to an organic substrate. The size of the package is 37 x 37 mm^2 and the gap between surface of chip and surface of substrate is 0.7 mm. For high performance FC-PBGA packages, a heat sink is usually required to dissipate the excess of heat, as illustrated at Fig. 5.24. Consequently, the warpage of the top surface becomes an important design parameter for an optimum thermal solution, especially when nonconductive interstitial materials between the heat sink and the silicon are employed [Verma 1999].

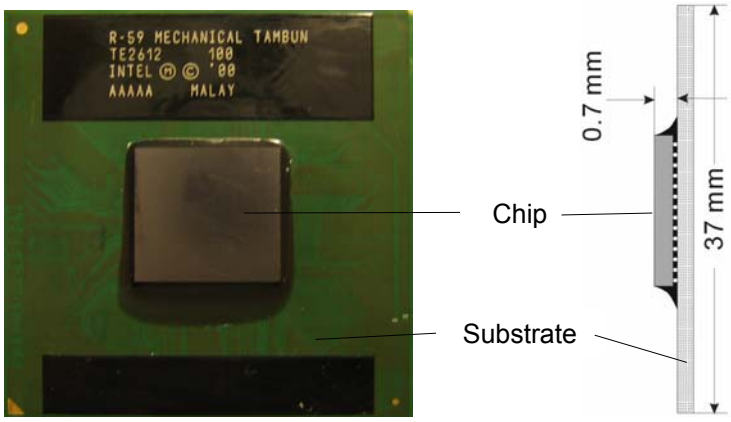

(a) (b)

Figure 5.23 FC-PBGA package (a) top view and (b) side view.

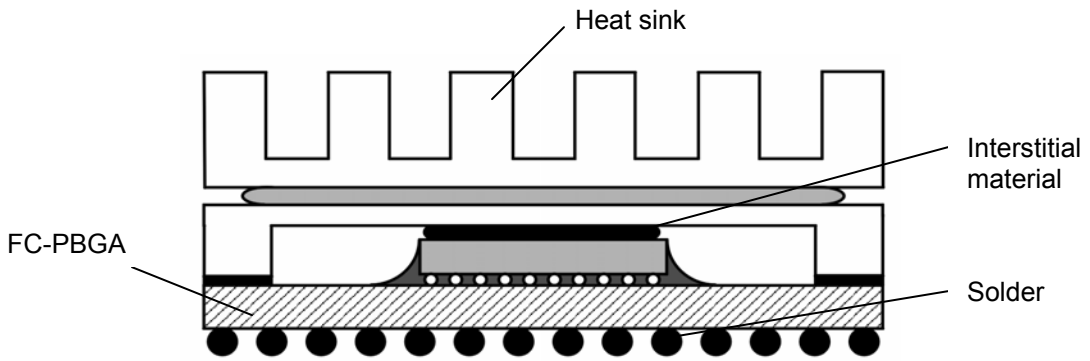

Figure 5.24 FC-PBGA with heat sink

With the conventional practice of using the zero Talbot area, it is not possible to obtain fringes of the non-coplanar surfaces unless the Talbot distance is much greater than the distance between the surfaces. As shown in Fig. 5.23 (b), the chip and substrate surfaces are separated by 0.7 mm. For the high sensitivity shadow moiré with a contour interval of 50 μm, the quarter Talbot distance becomes only 0.8 mm and the contrast of fringes on both surfaces cannot be obtained simultaneously. The contrast function of the two surfaces is illustrated in Fig. 5.25 (a) when the zero Talbot area is utilized. The fringe pattern obtained by the setup of white light, g = 0.1 mm, tan α = 2 and d_e = 0.01 (Γ = 50 μm/fringe) is shown in Fig. 5.25 (b). The fringe pattern can be seen only on the silicon chip.

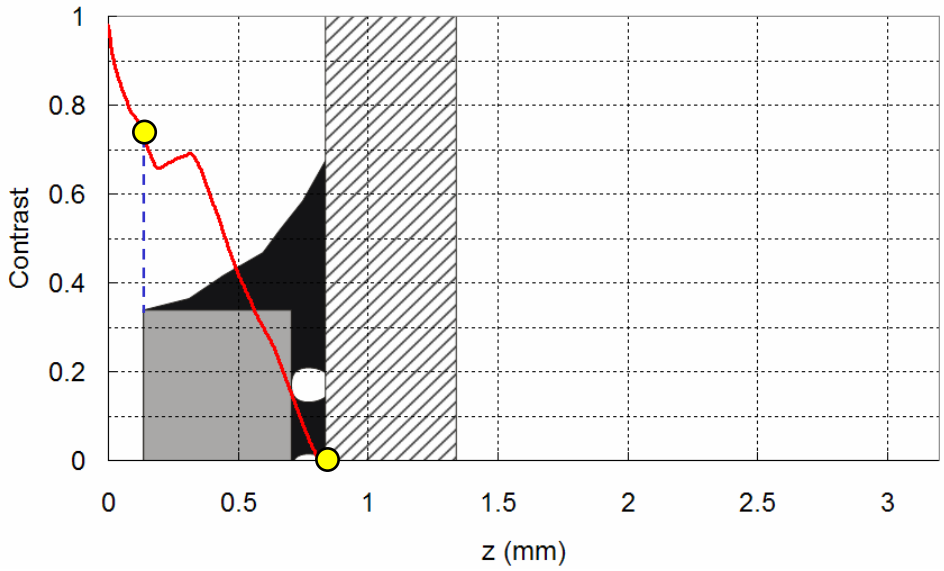

(a)

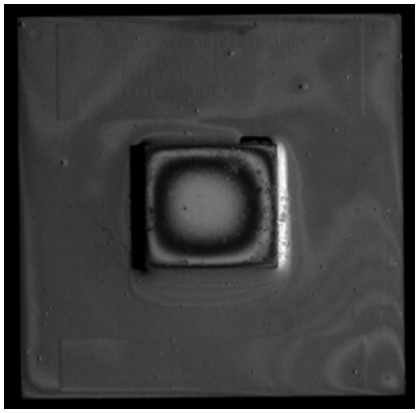

(b)

Figure 5.25 (a) Contrast function of shadow moiré fringe for the setup of white light, $g = 0.1$ mm, tan $\alpha = 2$, and $d_e = 0.01$ ($\Gamma = 50$ μm/fringe) and (b) shadow moiré fringe of the top surface of the specimen using the zero Talbot area.

The non-Zero Talbot area (more specifically the half Talbot area) can be employed to measure the deformation of the two non-coplanar surfaces simultaneously. In the first solution, the angle of incidence was adjusted until the substrate surface can be positioned near half the Talbot distance. Considering the physical gap of 0.7 mm, the incident angle was set at 68.2° $\left(\tan\alpha \approx 2.5\right)$ and its effect on the Talbot distance is illustrated in Fig. 5.26 (a). Note that the contour interval of the new configuration is 40 μm/fringe. The fringe pattern obtained from this configuration is shown in Fig. 5.26 (b). It is important to note that the fringes of the chip surface were obtained at the zero Talbot area while the fringes of the substrate surface were obtained at the half Talbot area.

Although it was implemented successfully for the specimen, this approach has a critical limitation. The optical setup will be extremely case-sensitive; the angle of incidence and the grating pitch will have to be optimized and selected based on the gap between the two surfaces and, for some cases, a practical configuration may not be available.

A more attractive solution is to utilize the half Talbot area by taking advantage of the large dynamic range. This approach is illustrated in Fig. 5.27 (a). The actual fringe pattern obtained from the optimized SM-NT setup is shown in (b). Excellent contrast of the fringes on both surfaces is achieved.

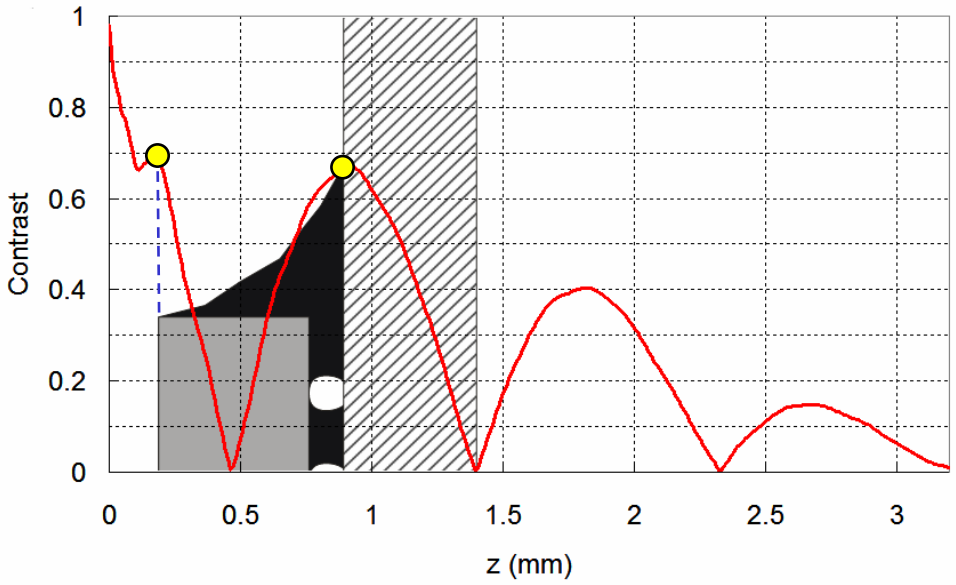

(a)

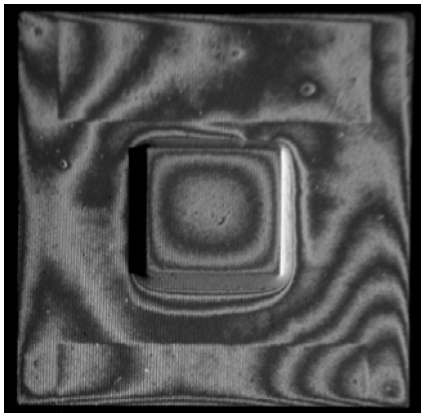

(b)

Figure 5.26 (a) Contrast function of shadow moiré fringe for the setup of white light, $g = 0.1$ mm, tan $\alpha = 2.5$, and $d_e = 0.01$ ($\Gamma = 40$ μm/fringe) and (b) shadow moiré fringe of the top surface of the specimen using the half Talbot area.

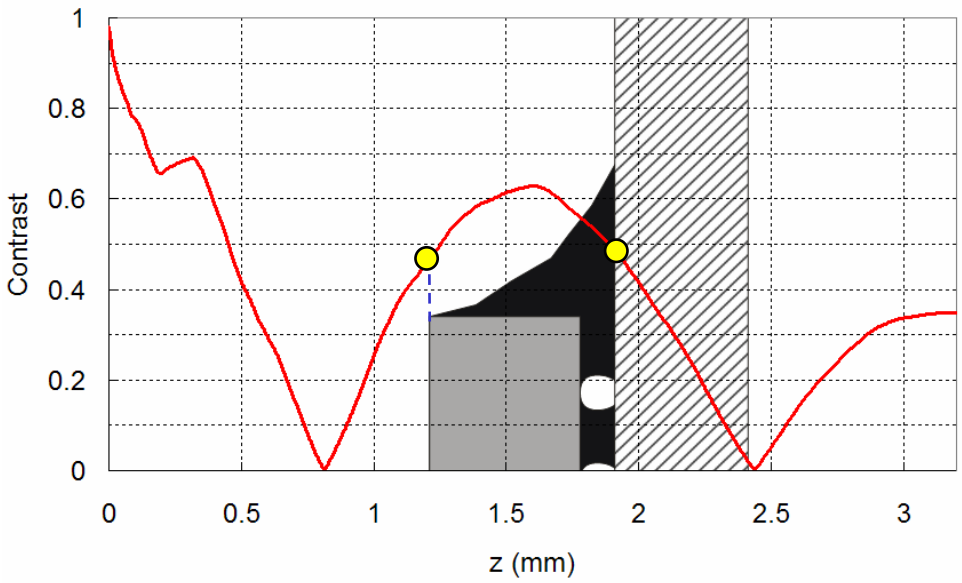

(a)

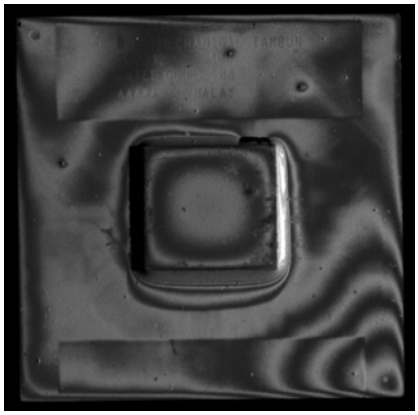

(b)

Figure 5.27 (a) Contrast function of shadow moiré fringe for the setup of white light, $g = 0.1$ mm, tan $\alpha = 2$, and $d_e = 0.01$ ($\Gamma = 50$ μm/fringe) and (b) shadow moiré fringe of the top surface of the specimen using the half Talbot area.

Part II: Application of Diffraction Theory to Moiré Interferometry

Chapter 6. Phase-shifting in Achromatic System

6.1 Basic Principles of Moiré Interferometry [Post 1994]

Moiré interferometry is a whole-field technique to measure in-plane displacements. It has been used extensively for deformation analyses in the various fields of mechanics [Guo 1993, Han 1996, 2000 and 2001, Cho, S. 2002, Cho, S.-M. 2002 and 2004, Ham 2003, Stellrecht 2003]. The data are received as interference fringe patterns, or contour maps, of the displacement fields. Because of the high sensitivity and abundance of data, reliable strain distributions—normal strains and shear strains—can be extracted from the patterns.

The general scheme of moiré interferometry is illustrated in Fig. 6.1. A high-frequency cross-line grating on a specimen, initially of frequency f_g, deforms together with the specimen. A parallel (collimated) beam, A_1, of laser light strikes the specimen and a portion is diffracted back, nominally perpendicular to the specimen, in the $+m_{th}$ order diffraction of the specimen grating. Light from the mutually coherent collimated beam A_2 is diffracted back in its $-m_{th}$ order. Since the specimen grating is deformed as a result of the applied loads, these diffracted beams are no longer collimated. Instead, they are beams with warped wave fronts, where the warpages are related to the deformation of the grating. These two coherent beams interfere in the image plane of the camera lens, producing an interference pattern of dark and light bands, which is the N_x moiré pattern.

Similarly, mutually coherent collimated beams B_1 and B_2, centered in the vertical plane, are diffracted in $+m_{th}$ and $-m_{th}$ orders diffraction by the nominally horizontal lines of the deformed specimen grating. These two diffracted beams interfere to produce the N_y moiré pattern. In practice, beams A_1 and A_2 are blocked, so the N_y fringes are viewed alone. Alternately, B_1 and B_2 are blocked to view the N_x fringes.

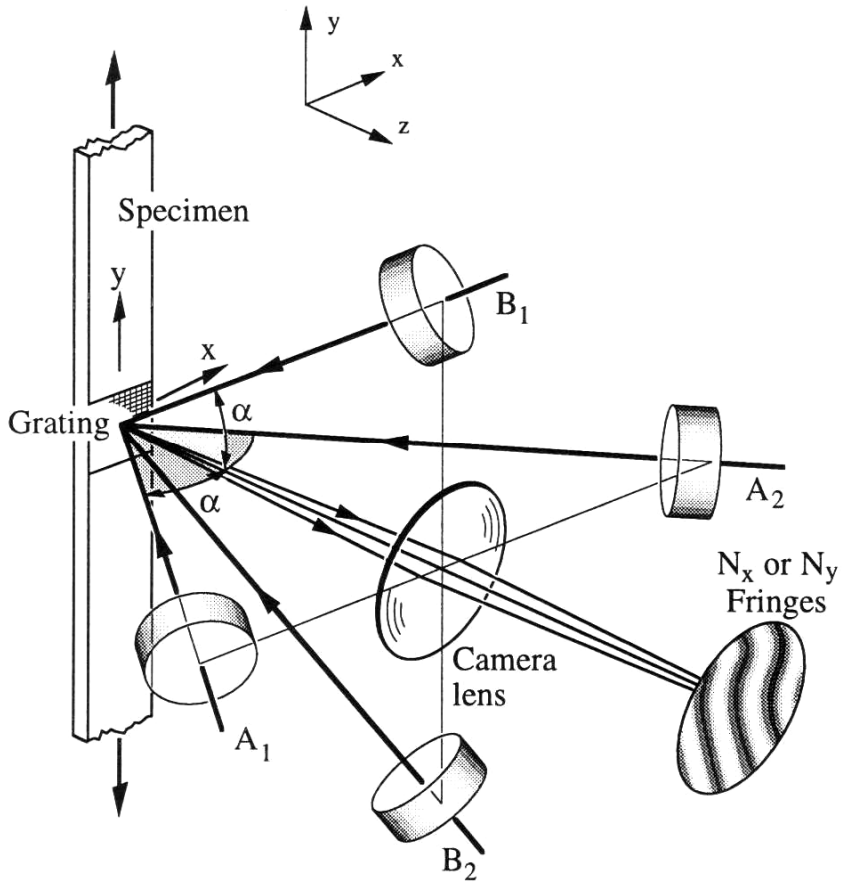

Figure 6.1 Schematic illustration of four-beam moiré interferometry to record the N_x and N_y fringe patterns, which depict the U and V displacement fields [Post 1994].

These moiré patterns are contour maps of the U and V displacement fields, i.e., the displacements in the x and y directions, respectively, of each point in the specimen grating. The relationships, for every x, y point in the field of view, are [Post 1994]

$$\begin{aligned} U(x,y) &= \frac{1}{2mf_g} N_x(x,y) = \frac{1}{f} N_x(x,y) \\ V(x,y) &= \frac{1}{2mf_g} N_y(x,y) = \frac{1}{f} N_y(x,y) \end{aligned} \tag{6.1}$$

In routine practice of moiré interferometry, f_g = 1200 lines/mm (30,480 lines/inch) and m = 1. In the fringe patterns, the contour interval becomes $1/2f_g$, which is 0.417 μm displacement per fringe order. The sensitivity is its reciprocal, 2.4 fringes per μm displacement.

When strains need to be extracted from the measured displacement fields, they can be determined by the small-strain relationships as

$$\varepsilon_x = \frac{\partial U}{\partial x} = \frac{1}{f}\frac{\partial N_x}{\partial x} \tag{6.2a}$$

$$\varepsilon_y = \frac{\partial V}{\partial y} = \frac{1}{f}\frac{\partial N_y}{\partial y} \tag{6.2b}$$

$$\gamma_{xy} = \frac{\partial U}{\partial y} + \frac{\partial V}{\partial x} = \frac{1}{f}\left(\frac{\partial N_x}{\partial y} + \frac{\partial N_y}{\partial x}\right) \tag{6.2c}$$

6.2 Mathematical Explanation of Principle based on Geometrical Approach

Dai [Dai 1990] explained the principle of moiré interferometry based on a geometrical approach, or *optical path length* (*OPL*) and it is briefly reviewed here. Consider any point P on an undeformed specimen grating of Fig. 6.2. Beams A_1 and A_2 have an initial phase difference from the source to P that differ by ϕ. The diffraction order is governed by the following relationship

$$\sin\theta_m = \sin\alpha + m\lambda f_g \tag{6.3}$$

where θ_m is the angle of the m_{th} order diffraction and λ is the wavelength of the beam. To achieve the null field condition where a pair of diffracted beams emerges normal to the specimen grating, the incident angle should satisfy the following relationship.

$$0 = \sin\alpha + m\lambda f_g \tag{6.4}$$

In Fig. 6.2, the two diffracted beams are represented by the wave fronts w_1' and w_2'. With the specimen still undeformed, the diffracted wave fronts w_1' and w_2' are plane and parallel. Thus, their phase difference is constant as ϕ, equal at every *x, y* point in the field and equal to the phase difference at P. The interference pattern seen in the camera image plane is a null field, with the same intensity at every *x, y* point.

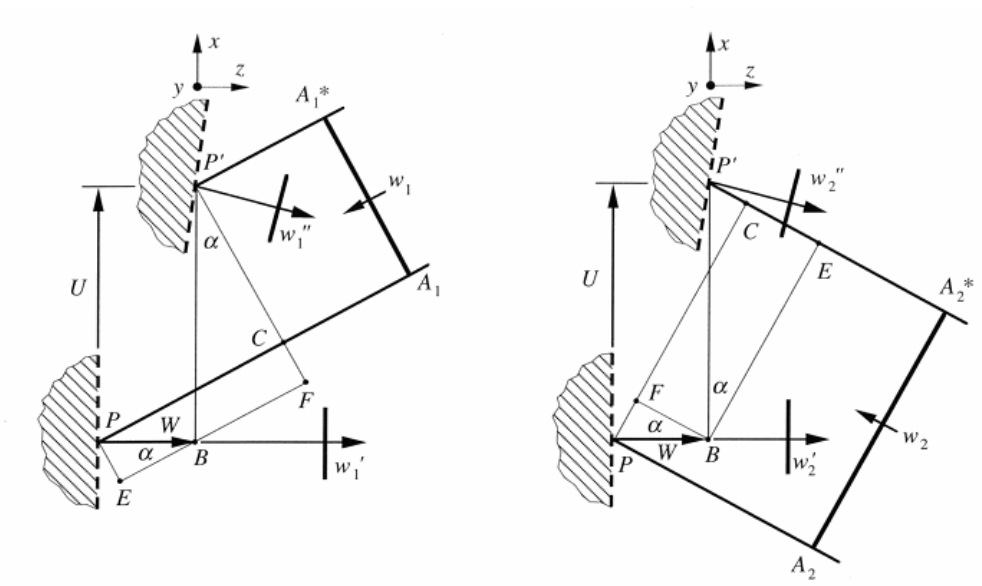

$$\Delta OPL_1 = A_1PB - A_1^*P'$$
$$= CP + PB$$
$$= (FB + BE) + PB$$
$$= (U\sin\alpha + W\cos\alpha) + W$$
$$= W(1 + \cos\alpha) + U\sin\alpha$$

$$\Delta OPL_2 = A_2PB - A_2^*P'$$
$$= A_2P - A_2^*P' + PB$$
$$= -(CP') + PB$$
$$= -(EP' - BF) + PB$$
$$= -(U\sin\alpha - W\cos\alpha) + W$$
$$= W(1 + \cos\alpha) - U\sin\alpha$$

Figure 6.2 Changes of optical path lengths when deformation causes point *P* to move to *P'* [Post 1994].

When the specimen is deformed, point *P* moves to a new location *P′*, where *U* and *V* are the in-plane components of the displacement and *W* is the out-of-plane component. Coordinate *y* and displacement *V* lie perpendicular to the plane of the diagram. In general, the pitch and slope of the grating surrounding *P′* will differ from the initial condition at *P*.

In the figure, w_1 is a plane wave front in incident Beam A_1; it extends as a plane normal to the diagram. The distance between the source and w_1 is the same for every

ray in the incident beam. The same explanation applies for plane wave front w_2. Furthermore, *P'B* lies in the object plane, so the *optical path length (OPL)* from *P'* and *B* through the camera lens to the image plane is the same. Therefore, the changes of *OPL*s between the source and the image plane reduce to the changes of *OPL*s between w_1 and *P'B* and between w_2 and *P'B*.

The changes of *OPL*s are analyzed in the figure, with the result

$$\begin{aligned} \Delta OPL_1(x,y) &= W(x,y)\left(1+\cos\alpha\right)+U(x,y)\sin\alpha \\ \Delta OPL_2(x,y) &= W(x,y)\left(1+\cos\alpha\right)-U(x,y)\sin\alpha \end{aligned} \tag{6.5}$$

Observe that any *V* component of displacement does not change the distance between wave front w_1 and *P'*, nor the distance between w_2 and *P'*. Therefore, the changes of *OPL*s are independent of *V*. Using Eq. 6.5, the relative *OPL* difference, *S*, between two beams at *P'* can be expressed as

$$\begin{aligned} S(x,y) &= \Delta OPL_1(x,y)-\Delta OPL_2(x,y)+\frac{\phi\lambda}{2\pi} \\ &= 2m\lambda f_g U(x,y)+\frac{\phi\lambda}{2\pi} \end{aligned} \tag{6.6}$$

The intensity resulting from the interference of two beams is

$$\begin{aligned} I(x,y) &= I_1(x,y)+I_2(x,y)+2\sqrt{I_1(x,y)I_2(x,y)}\cos\left(2\pi\frac{S(x,y)}{\lambda}\right) \\ &= I_1(x,y)+I_2(x,y)+2\sqrt{I_1(x,y)I_2(x,y)}\cos\left(2\pi 2m f_g U(x,y)+\phi\right) \end{aligned} \tag{6.7}$$

where I_1 and I_2 are the intensity of Beams A_1 and A_2, respectively. The *OPL* difference represents the fringe order N at each point of the pattern by $N_x(x,y) = \frac{S(x,y)}{\lambda}$. Accordingly, the displacement is determined from the interference pattern by

$$U(x,y) = \frac{1}{2mf_g}\left(N_x(x,y) - \frac{\phi}{2\pi} \right) \tag{6.8}$$

The constant $\frac{\phi}{2\pi}$ is equivalent to a uniform displacement throughout the field, or a rigid body translation. When studying deformations we are not interested in rigid body motions. We can disregard the constant and interpret the pattern by

$$U(x,y) = \frac{1}{2mf_g} N_x(x,y) = \frac{1}{f} N_x(x,y)$$

which is identical to Eq. 6.1. $U(x, y)$ represents the displacement of every x, y point relative to an arbitrarily selected reference point of $N_x = 0$.

6.3 Phase-shifting in Achromatic System

The phase-shifting technique has been adopted for moiré interferometry to increase the measurement sensitivity since the early 1990s [Salbut 1990, Kujawinska 1991, Han 1993 b and c, He 1998, Miller 1999, Liu 2003 and 2004].

A concept of phase shifting is illustrated in Fig. 6.3. For the system, the phase-shifting was explained by the concept of *OPL* [Han 1999]. The incident beam is separated into *Beam 1* and *Beam 2* by a beam splitter. They meet at a point *P* on the specimen. The *OPL* difference determines the state of constructive or destructive interference at *P*. If all the optical elements are translated with respect to the specimen grating by the same distance Δ, as illustrated in Fig. 6.3, the *Beam 2* reflected by the beam-splitter hits the same point *P* on the specimen without any change of the *OPL*. However, the transmitted *Beam 1* reaches point *P* with an *OPL* change of

$$\delta = 2\Delta \sin\alpha \tag{6.9}$$

The fringe shifts by $\frac{\delta}{\lambda}$ and the corresponding phase shift is $2\pi\frac{\delta}{\lambda}$.

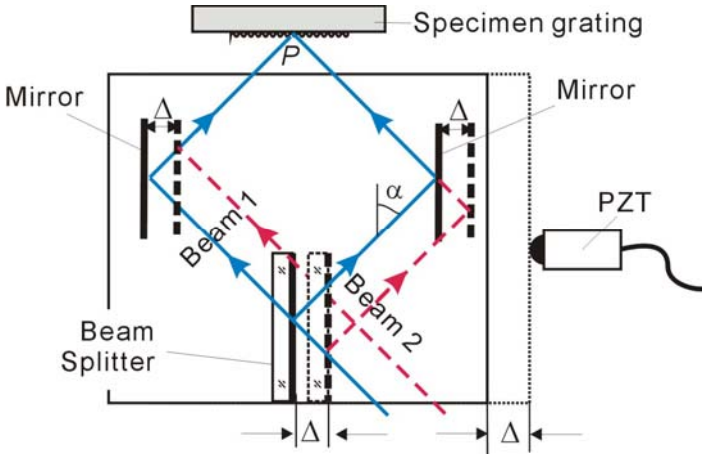

Figure 6.3 Phase-shifting in moiré interferometry.

The achromatic moiré interferometry system was originally developed to relax coherent length requirement of the light source [Post 1994]. As illustrated in Fig. 6.4, a grating, called *compensator grating*, is used in the system instead of a beam splitter. The compensator grating allows variation of α and λ in precise harmony in such a way that the condition of Eq. 6.4 is always satisfied. It has been know that the phase-shifting can be accomplished by translating the compensator grating by a fraction of its pitch as illustrated in Fig. 6.4 [Post 1994].

The phase-shifting mechanism shown in Fig. 6.3 was explained clearly by using the concept of *OPL*. However the phase-shifting mechanism of the achromatic system cannot be explained by the same concept; the translation of the compensator grating does not change the *OPL*. The phase information of the diffracted beam is required to explain the mechanism in the achromatic system.

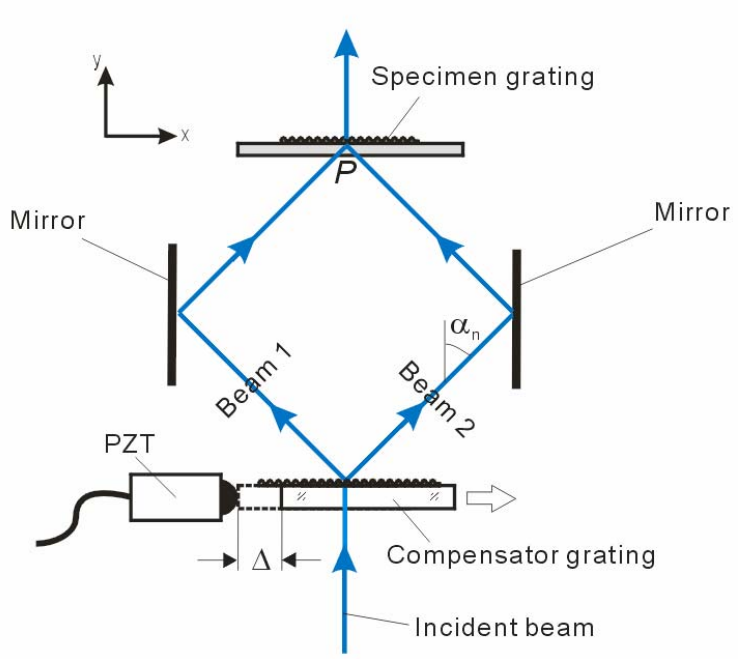

Figure 6.4 Illustration of an achromatic system and phase-shifting.

6.4 Analysis of Phase-shifting in Achromatic System

6.4.1 Mathematical Analysis of Phase Change in Diffracted Beam

The rigorous grating theory based on the laws of electromagnetism [Maystre 1984] is used to define the phase of the diffracted beam with respect to the relative position to the compensator grating.

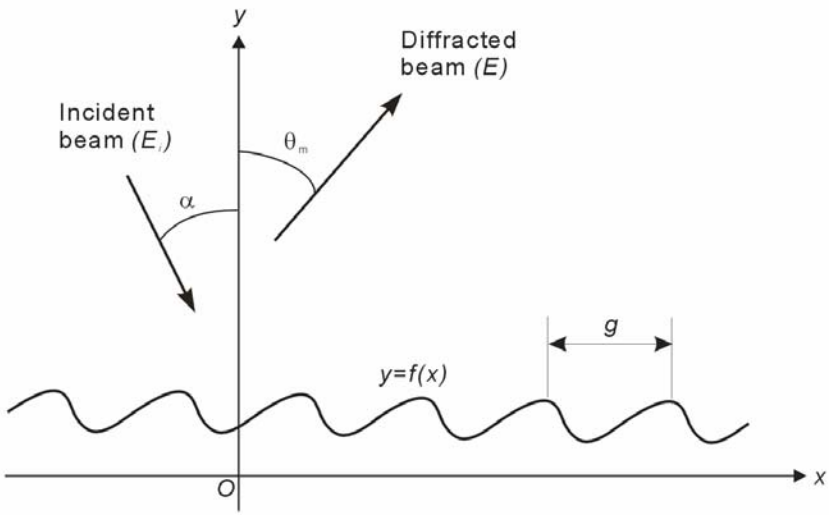

Figure 6.5 Incident and diffracted beams on a linear grating with a pitch of *g* and a profile of *f(x)*.

Complex field of an incident beam of unit amplitude at an angle of incidence, α, is defined as

$$E_i = \exp\left(i \frac{2\pi}{\lambda} \left(x \sin\alpha - y \cos\alpha \right) \right) \tag{6.10}$$

The incidence beam illuminates a linear grating with a pitch of *g* and a profile of *f(x)* in *Oxy* coordinate as illustrated at Fig. 6.5.

From the rigorous grating theory, it was shown that the complex field of the diffracted beam from the grating is governed by [Maystre 1984]

$$\nabla^2 E + k^2 E = 0 \tag{6.11}$$

and solution of Eq. 6.11 is derived as [Maystre 1984]

$$\begin{aligned} E(x,y) &= \sum_m E_m(x,y) = \sum_m B_m \Phi_m(x,y) \\ &= \sum_m B_m \exp\left(i \frac{2\pi}{\lambda} \left(x \sin\theta_m + y \cos\theta_m \right) \right) \end{aligned} \tag{6.12}$$

where $\sin\theta_m = \sin\theta + \lambda m / g$ and m stands for the order of diffraction. Each term of E_m in Eq. 6.12 represents a diffraction order. The 2-D function $\Phi_m(x,y)$, defines the phase of each diffracted beam and the coefficient B_m, defines the amplitude of the diffraction order.

The coefficient can be evaluated for the case of transverse polarization, where the complex field remains normal to *Oxy* plane. For the transverse polarization, the condition as following should be met on the boundary of the grating [Maystre 1984]

$$E = -E_i = -\exp\left(i \frac{2\pi}{\lambda} \left(x \sin\alpha - f(x) \cos\alpha \right) \right) \tag{6.13}$$

With the boundary condition, the coefficient is represented by [Maystre 1984]

$$B_m = \frac{\lambda}{i4\pi g \cos\theta_m} \int_0^g \exp\left(-i\frac{2\pi}{\lambda}\left(x\sin\theta_m + f(x)\cos\theta_m \right) \right) \left(1 + f'(x)^2\right)^{1/2} \frac{d(E+E_i)}{dn} dx \tag{6.14}$$

As the coefficient B_m in Eq. 6.14 includes the complex field itself, the explicit form of solution for the coefficient cannot be obtained. Numerical approach is inevitable to evaluate the coefficient. There are several numerical methods to determine B_m; the Rayleigh method, the Waterman method, the integral method, and the differential method. In this study, Point Matching Method (PMM), which is one of the Rayleigh methods, is used for simplicity. In the method, the boundary condition is written as [Maystre 1984]

$$\sum_m B_m \Phi_m(x, f(x)) + F_i(x, f(x)) = 0 \tag{6.15}$$

The only unknown in Eq. 6.15 is a set of complex coefficient B_m. Eq. 6.15 can be changed into a system of $2N+1$ linear equation with $2N+1$ unknowns as

$$\sum_{m=-N}^{+N} B_m^{(N)} \Phi_m(x, f(x)) + E_i(x, f(x)) = 0 \tag{6.16}$$

Eq. 6.16 can be solved by selecting $2N+1$ points in the profile. More information about the method can be found in the reference [Maystre 1984].

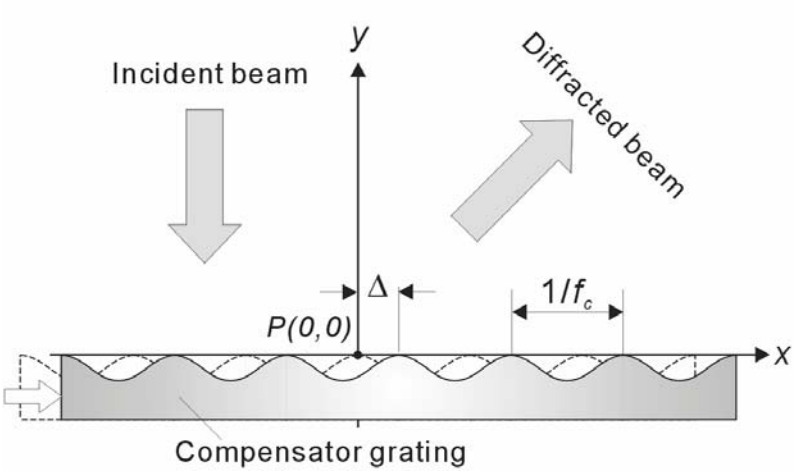

Figure 6.6 Translation of compensator grating and phase change at a point *P(0, 0)* of a diffracted beam.

As illustrated in Fig. 6.6, phase change in a point with the translation of compensator grating in the achromatic system is analyzed using the point matching method. The profile of the compensator grating is defined as a sinusoidal function as

$$f(x) = \frac{h}{2}\cos\left(2\pi f_c\left(x-\Delta\right)\right) - \frac{h}{2} \tag{6.17}$$

where h is the depth of groove, f_c is the frequency of the compensator grating, and Δ is the amount of translation of the compensator grating. As the compensator grating is translated Δ, the change of phase in a diffracted beam at point *P(0, 0)* is calculated. For the calculation, the compensator grating of f_c = 1200 lines/mm and h = 0.1 μm is selected in practical consideration. The wavelength of the incident beam is assumed as 350 nm to investigate the diffraction up to the second order. The *Matlab* code used in the numerical calculation can be found in Appendix A. As the phase is calculated at *P(0, 0)*, the phase is only decided by the coefficient B_m. It is important to note that

the constant B_m is a complex number depending on the boundary condition. If the coefficient is a real number, which corresponds to any scalar diffraction theory, the change of phase in the diffracted beam with the translation of the compensator grating cannot be reflected.

The calculated phase is shown at Fig. 6.7. Figure 6.7 (a) represents the results of the first order diffraction. As the compensator grating translates from 0 to one period of the grating, the phase at *P(0, 0)* changes linearly from 0 to 2π. In the second order diffraction, the phase changes two times faster as shown in Fig. 6.7 (b).

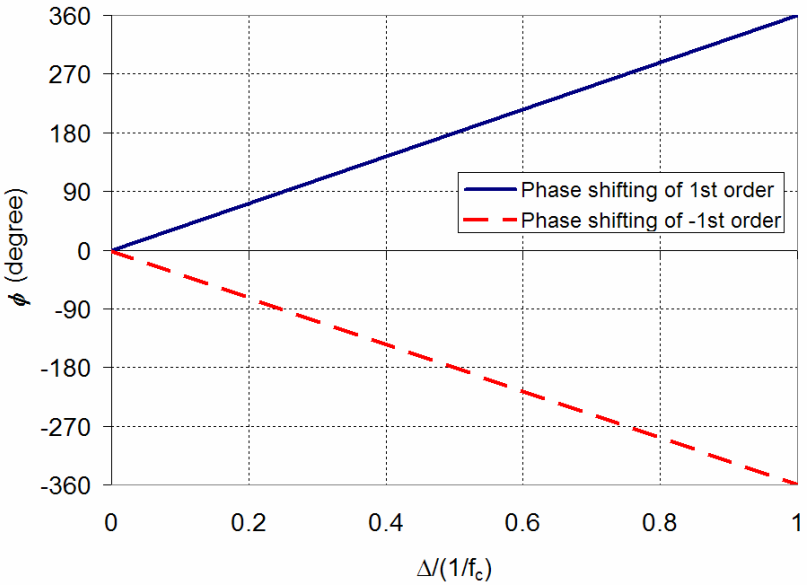

(a)

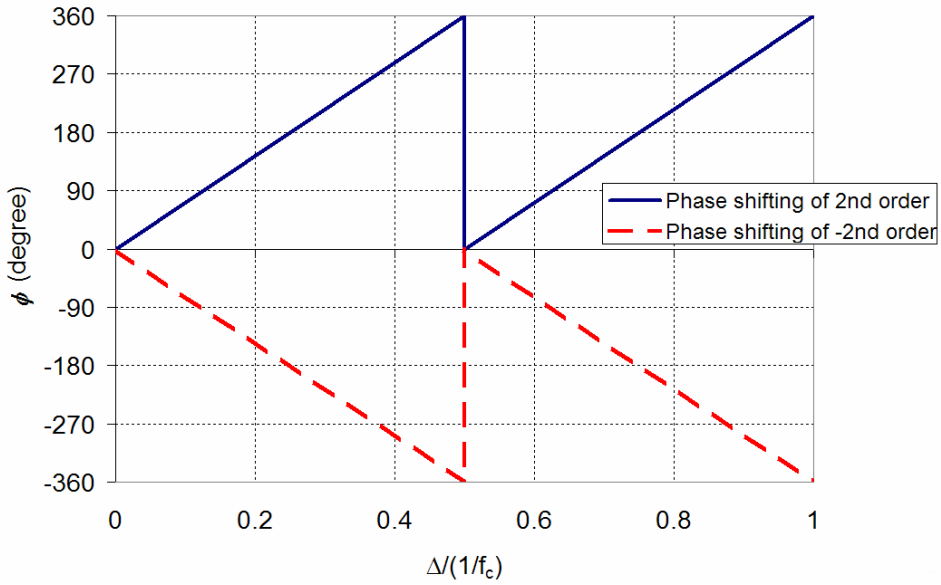

(b)

Figure 6.7 Result of the rigorous grating theory analysis for the relation phase-shifting and the translation of the compensator grating: (a) first and (b) second order of diffraction beam.

The relation between the translation of the compensator grating Δ, and the phase change in the diffracted beam ϕ, can be summarized as

$$\phi = 2\pi n f_c \Delta \tag{6.18}$$

where n is the order of diffraction and f_c is the frequency of the compensator grating.

6.4.2 Physical Explanation of Phase Change in Diffracted Beam

Based on the mathematical analysis, the plane wave fronts of the first and second order beams diffracted from a compensator grating are illustrated in Fig. 6.8 (a) and (b). The phase of the diffracted beams changes cyclically from 0 to 2π as the wave fronts propagate in the diffraction direction. In the figures, a series of solid grid lines represents the phase of multiples of 2π in the diffracted beams and the distance between two adjacent lines is the wavelength of incident beam.

The diffraction equation with the normal illumination can be written as

$$\sin \alpha_n = n\lambda f_c \tag{6.19}$$

where n represents the diffraction order from the compensator grating and α_n is the diffraction angle. Equation 6.19 defines the amount of phase change within one pitch of the compensator and it is illustrated graphically in Figs. 6.8 (c) and (d). With the first order diffraction (Fig. 6.8(c)), the phase change within one pitch is 2π, while the phase change of the second order within one pitch increased by a factor of 2 (Fig. 6.8 (d)).

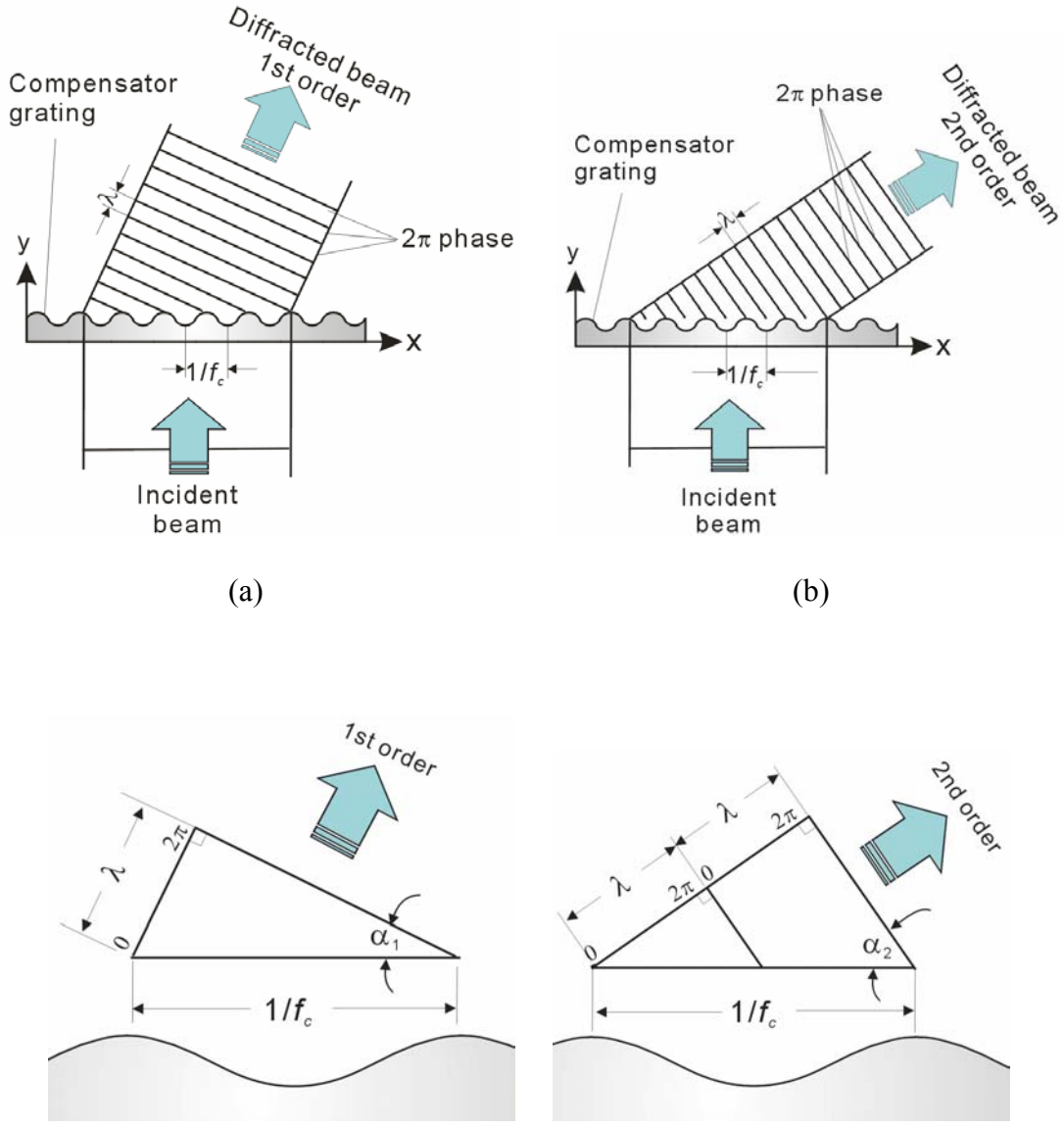

Figure 6.8 Illustration of the phase of diffracted beam from the compensator grating: (a) first and (b) second order of diffraction. Geometrical relations between the diffraction orders and the phase change within a pitch of grating are shown in (c) and (d).

Since the phase of the diffracted beam is defined as the relative position to the grating, the phase should change together with the translation of the grating coordinate. Consequently, the phase should be shifted linearly when the compensator grating is translated. The phase shifting of the diffracted beams is illustrated in Figs. 6.9 (a) and (b), where the compensator grating is translated along the *x* direction by a distance of Δ. Further details are presented in Figs. 6.9 (c) and (d), where the relationship between the phase shift, ϕ, and the amount of translation, Δ for the two different diffraction orders. The relationship for the n_{th} order can be written again as

$$\phi = 2\pi n f_c \Delta \tag{6.18}$$

The amount of phase change is proportional to the amount of translation of the compensator grating. The constant of the proportionality is the product of the diffraction order and the frequency of the compensator grating.

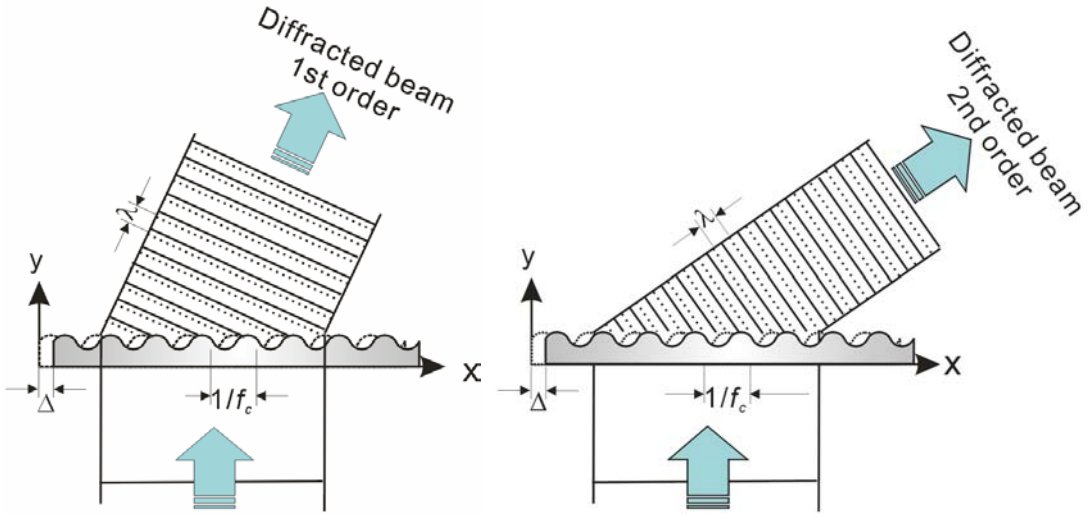

(a) (b)

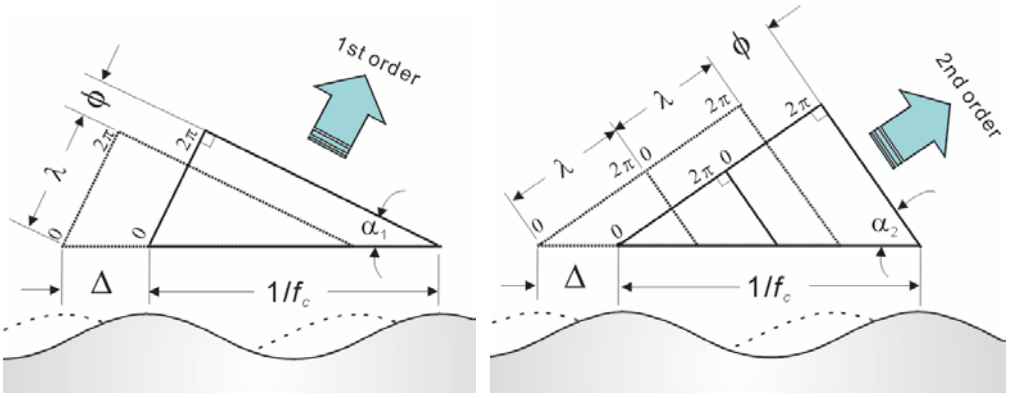

(c) (d)

Figure 6.9 Translation of compensator grating (Δ) and the corresponding phase-shifting of diffracted beams (ϕ) for the first (a), and second (b) order diffraction. More detailed geometrical relationship is given in (c) and (d).

6.4.3 Phase-shifting in Fringe of Achromatic System

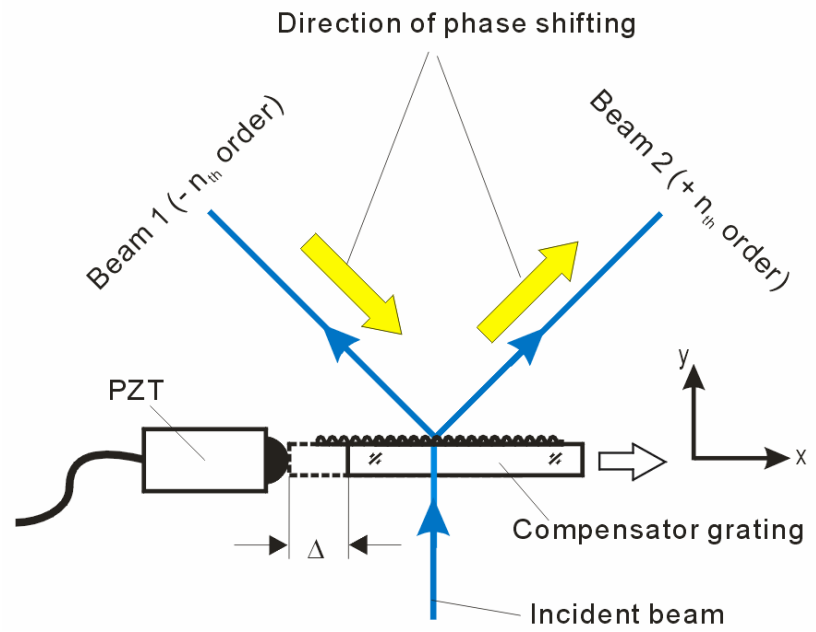

Figure 6.10 Two diffracted beams in an achromatic system and the direction of phase shifting on the beams after the compensator grating is shifted.

Figure 6.10 shows the two diffracted beams from an achromatic system; one (*Beam 1*) is $-n_{th}$ order and the other (*Beam 2*) is $+n_{th}$ order. The complex field of each beam is written as

$$E_1 = B_{-n} \exp\left\{ i\left[\frac{2\pi}{\lambda}\left(-x\sin\alpha_n + y\cos\alpha_n\right)\right] + \phi_1\big|_{-n} \right\} \tag{6.20a}$$

$$E_2 = B_n \exp\left\{ i\left[\frac{2\pi}{\lambda}\left(x\sin\alpha_n + y\cos\alpha_n\right)\right] + \phi_2\big|_{n} \right\} \tag{6.20b}$$

From Eq. 6.18, the phase shift of each beam is

$$\phi_1\big|_{-n} = -2\pi n f_c \Delta \tag{6.21a}$$

$$\phi_2\big|_{n} = 2\pi n f_c \Delta \tag{6.21b}$$

Translating the compensator grating in the positive *x*-direction causes the phase of the two beams to shift in the same positive *x*-direction as illustrated in Fig. 6.10.

By plugging the phase shift of Eq. 6.21 into the governing equation of moiré interferometry in Eq. 6.7, the phase shift in the fringe of moiré interferometry due to the translation of the compensator grating can be written as

$$\begin{aligned} I &= I_1 + I_2 + 2\sqrt{I_1 I_2}\cos\left\{2\pi 2 m f_g U(x) + \phi_1 - \phi_2\right\} \\ &= {}_1 + I_2 + 2\sqrt{I_1 I_2}\cos\left\{2\pi 2 m f_g U(x) - 4\pi n f_c \Delta\right\} \\ &= {}_1 + I_2 + 2\sqrt{I_1 I_2}\cos\left\{2\pi\left(2 m f_g U(x) - 2 n f_c \Delta\right)\right\} \end{aligned} \tag{6.22}$$

Equation 6.22 says that the required amount of compensator grating translation to get the 2π phase-shifting in the fringe of moiré interferometry, $\Delta_{2\pi}$, is

$$\Delta_{2\pi} = \frac{1}{2 n f_c} \tag{6.23}$$

Two examples of an achromatic system are shown in Fig. 6.11. The system in Fig. 6.11 (a) uses a 1200 lines/mm reflection-type compensator grating with ± 1 diffraction order and the same frequency of specimen grating, which is replicated on a specimen [Post 1994, He 1998]. From Eq. 6.23, the compensator grating is translated by $1/2nf_c = 0.417$ μm to get a 2π fringe shift.

The system shown in Fig. 6.11 (b) utilized the same compensator grating of 1200 lines/mm but the 2400 lines/mm of specimen grating was selected to take advantage of the concept of an immersion interferometer [Han 1992 a and b]. Also, to achieve the extremely high magnification factor of imaging system, a replica of the deformed grating, which is a transmission-type specimen grating, is utilized [Han, C. 2003]. The sensitivity of the system is 4800 fringes/mm, doubling the sensitivity of the system in Fig. 6.11 (a). However, by Eq. 6.23, the required amount of compensator grating translation remains the same at 0.417 μm.

Utilizing the result that the phase-shifting in an achromatic system is only dependent on the frequency and diffraction order of the compensator grating, it is possible to select an optimal frequency of compensator grating for the best response of PZT regardless of the sensitivity of the system.

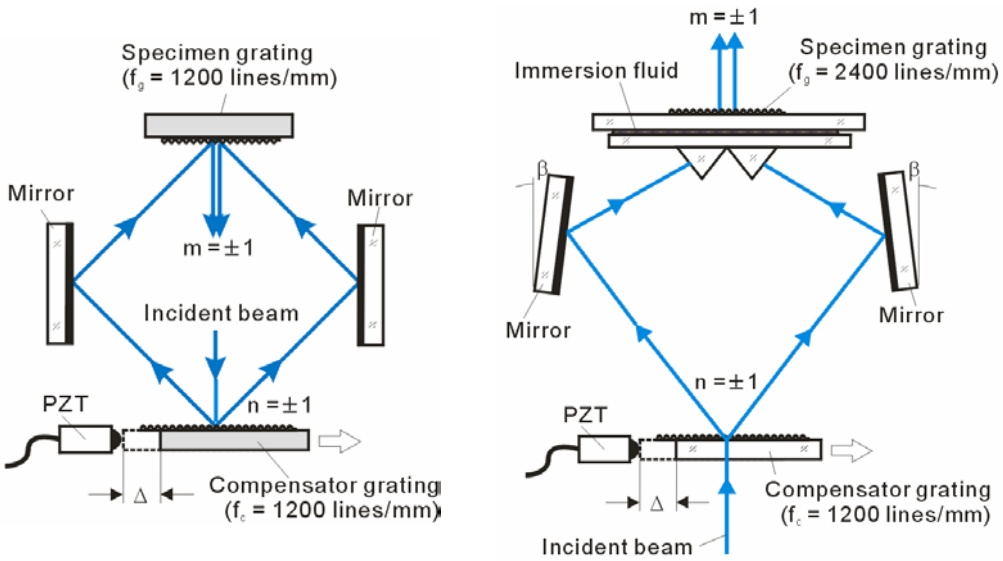

(a) (b)

Figure 6.11 Examples of an achromatic system (a) reflection type, (b) transmission type with immersion interferometer.

Chapter 7. Characteristics of the Diffracted Wave Front

7.1 Decomposition of Wave Front

In an important paper [McKelvie, 1990] on moiré interferometry, McKelvie explained the fringe formation of moiré interferometry by decomposing the diffracted beams into a series of *mini-order*s. His derivation was based on a scalar diffraction theory using a sinusoidal type strain distribution. The following discussion summarizes a part of his analysis.

The profile of an undeformed holographic grating is given by

$$\phi_i = \frac{h}{2}\sin\left(2\pi f_g x\right) \tag{7.1}$$

where h is the depth of the grating groove and f_g is the frequency of the grating. The grating is illuminated by a monochromatic collimated beam of unit amplitude at an angle of incidence, α. The incident beam is represented by

$$E_i = \exp\left(i\frac{2\pi}{\lambda}x\sin\alpha\right) \tag{7.2}$$

The diffracted beam on the grating has its flat phase disturbed by $2\phi_i$, and its representation is

$$
\begin{aligned}
E_d &= \exp\left(\frac{i2\pi}{\lambda}\left(x\sin\alpha + h\sin(2\pi f_g x)\right)\right) \\
&= \exp\left(\frac{i2\pi}{\lambda}x\sin\alpha\right)\exp\left(\frac{i2\pi h}{\lambda}\sin(2\pi f_g x)\right)
\end{aligned}
\tag{7.3}
$$

The perfect conduction of the grating surface is assumed in Eq. 7.3 and consequently the total energy will be preserved. This assumption will be held for all of the following analysis.

The second exponential in Eq. 7.3 can be decomposed by *Jacobi-Anger expansion* into a series, which leads to

$$
\begin{aligned}
E_d &= \exp\left(\frac{i2\pi}{\lambda}x\sin\alpha\right)\sum_{m=-\infty}^{\infty} J_m\left(\frac{2\pi h}{\lambda}\right)\exp\left(im2\pi f_g x\right) \\
&= \sum_{m=-\infty}^{\infty} J_m\left(\frac{2\pi h}{\lambda}\right)\exp\left(\frac{i2\pi x}{\lambda}(\sin\alpha + m\lambda f_g)\right)
\end{aligned}
\tag{7.4}
$$

where $J_m(\ )$ is the m_{th} order first kind Bessel function. Equation 7.4 represents the diffracted beams on a uniform grating. The angle of diffraction is governed by the grating equation and the amplitude of beam is defined by a Bessel function. Figure 7.1 (a) illustrates the m_{th} order of Eq. 7.4, which is diffracted normal to the undeformed grating.

When the specimen is subjected to a sinusoidal strain distribution of

$$
\varepsilon(x) = b\cos 2\pi f_s x \tag{7.5}
$$

, the deformed grating becomes

$$\phi = \frac{h}{2}\sin\left(2\pi f_g x - \frac{bf_g}{f_s}\sin(2\pi f_s x)\right) \tag{7.6}$$

Then, the diffracted beam from the incident beam of Eq. 7.2 is expressed as

$$E_d = \exp\left(\frac{i2\pi}{\lambda}\left(x\sin\alpha + h\sin\left(2\pi f_g x - \frac{bf_g}{f_s}\sin(2\pi f_s x)\right)\right)\right) \tag{7.7}$$

Equation 7.7 can be also decomposed by *Jacobi-Anger expansion* into

$$\begin{aligned} E_d &= \exp\left(\frac{i2\pi}{\lambda}x\sin\alpha\right)\sum_{m=-\infty}^{\infty} J_m\left(\frac{2\pi h}{\lambda}\right)\exp\left(im\left(2\pi f_g x - \frac{bf_g}{f_s}\sin(2\pi f_s x)\right)\right) \\ &= \exp\left(\frac{i2\pi}{\lambda}x\sin\alpha\right)\sum_{m=-\infty}^{\infty} J_m\left(\frac{2\pi h}{\lambda}\right)\exp\left(im2\pi f_g x\right) \\ &\qquad \times \sum_{r=-\infty}^{\infty} J_r\left(\frac{mbf_g}{f_s}\right)\exp\left(ir2\pi f_s x\right) \\ &= \sum_{m=-\infty}^{\infty}\sum_{r=-\infty}^{\infty} J_m\left(\frac{2\pi h}{\lambda}\right)J_r\left(\frac{mbf_g}{f_s}\right)\exp\left(\frac{i2\pi x}{\lambda}\left(\sin\alpha + m\lambda f_g + r\lambda f_s\right)\right) \end{aligned} \tag{7.8}$$

The m_{th} order diffraction beam is written from Eq. 7.8 as

$$E_d\big|_m = \sum_{r=-\infty}^{\infty} J_m\left(\frac{2\pi h}{\lambda}\right)J_r\left(\frac{mbf_g}{f_s}\right)\exp\left(\frac{i2\pi x}{\lambda}\left(\sin\alpha + m\lambda f_g + r\lambda f_s\right)\right) \tag{7.9}$$

Note that the m_{th} order diffraction beam consists of a series of plane beams, called *mini-order*s. Mini-orders carry the information on strain variations. Figure 7.1 (b) illustrates the m_{th} order and its mini-order, which is produced by the deformed grating with the sinusoidal strain distribution. Although numerical examples were not presented in the McKelvie's paper [McKelvie, 1990], it is clear from Eq. 7.9 that the

magnitudes of the mini-orders are very small compared to that of the main diffraction order.

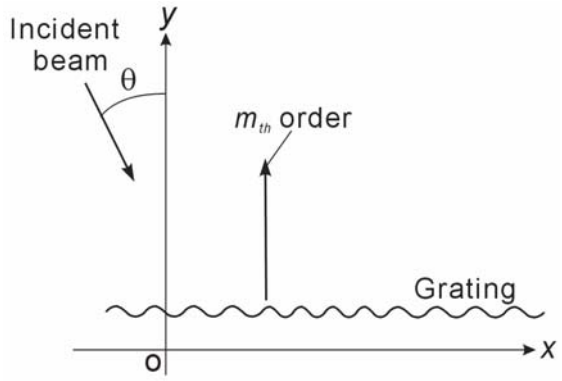

(a)

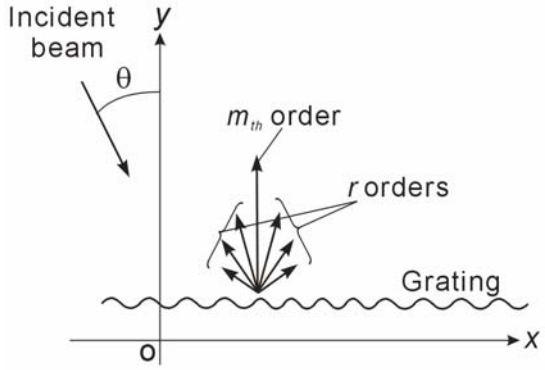

(b)

Figure 7.1 (a) Diffracted beam of an undeformed grating and (b) diffracted beam and its mini-order of a deformed grating.

7.2 Extension to General Strain Distribution

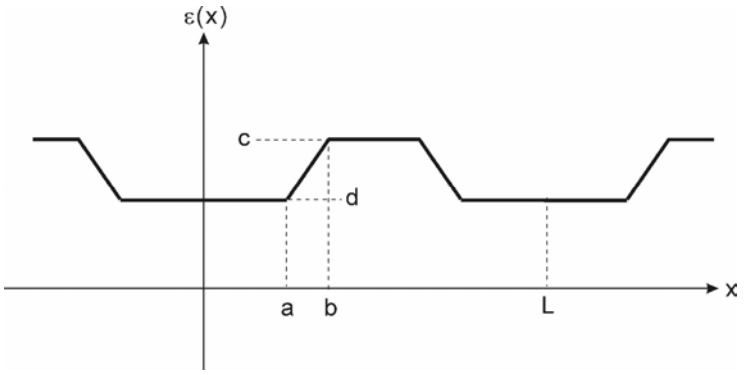

Figure 7.2 Trapezoid-shaped strain distribution.

The sinusoidal strain distribution used in the previous section is not realistic; it was chosen for the original analysis just for mathematical convenience. A more general case of strain distribution is considered. As illustrated in Fig. 7.2, a trapezoid-shaped strain distribution makes a parametric study possible to investigate the effect of various parameters on the magnitude and angle of the *min-order*s; the parameters include the ratio of strain width (*a* and *b*), the strain level (*c* and *d*), the strain gradient ((*d*-*c*)/(*a*-*b*)), and the period of strain (*L*). The trapezoid-shaped strain distribution in Fig. 7.2 can be represented by a Fourier series as

$$\varepsilon(x) = a_0 + \sum_{k=1}^{\infty} a_k \cos\left(\frac{2k\pi}{L}x\right)$$

$$\text{where} \quad a_0 = \frac{1}{L}\left[d(a+b) + c(L-a-b)\right] \tag{7.10}$$

$$\text{and} \quad a_k = \frac{c-d}{b-a}\frac{L}{(k\pi)^2}\left[\cos\left(\frac{2k\pi b}{L}\right) - \cos\left(\frac{2k\pi a}{L}\right)\right]$$

The deformed grating profile for the strain distribution of Eq. 7.10 can be written as

$$\phi = \frac{h}{2}\sin\left(2\pi f_g\left(x - a_0 x - \sum_{k=1}^{\infty}\frac{a_k L}{2k\pi}\sin\left(\frac{2k\pi}{L}x\right)\right)\right) \tag{7.11}$$

Then the diffracted beam from the deformed grating becomes

$$E_d = \exp\left(\frac{i2\pi}{\lambda}\left(x\sin\alpha + h\sin 2\pi f_g\left(x - a_0 x - \sum_{k=1}^{\infty}\frac{a_k p}{2k\pi}\sin\left(\frac{2k\pi}{L}x\right)\right)\right)\right) \tag{7.12}$$

By applying *Jacobi-Anger expansion*, Eq. 7.12 is transformed into

$$\begin{aligned} E_d &= \exp\left(\frac{i2\pi}{\lambda}x\sin\alpha\right)\times \\ &\quad \exp\left(\frac{i2\pi h}{\lambda}\sin 2\pi f_g\left(x - a_0 x - \sum_{k=1}^{\infty}\frac{a_k L}{2k\pi}\sin\left(\frac{2k\pi}{L}x\right)\right)\right) \\ &= \exp\left(\frac{i2\pi}{\lambda}x\sin\alpha\right)\times \\ &\quad \sum_{m=-\infty}^{\infty} J_m\left(\frac{2\pi h}{\lambda}\right)\exp\left(im2\pi f_g\left(x - a_0 x - \sum_{k=1}^{\infty}\frac{a_k L}{2k\pi}\sin\left(\frac{2k\pi}{L}x\right)\right)\right) \end{aligned} \tag{7.13}$$

The second exponential term in Eq. 7.13 can be also decomposed by *Jacobi-Anger expansion* as

$$E_d = \exp\left(\frac{i2\pi}{\lambda} x \sin\alpha\right) \times$$
$$\sum_{m=-\infty}^{\infty} J_m\left(\frac{2\pi h}{\lambda}\right) \exp\left(im2\pi f_g\left(1-a_0\right)x\right) \exp\left(imf_g\left(-\sum_{k=1}^{\infty}\frac{a_k L}{k}\sin\left(\frac{2k\pi}{L}x\right)\right)\right)$$

$$= \sum_{m=-\infty}^{\infty} J_m\left(\frac{2\pi h}{\lambda}\right) \exp\left(\frac{i2\pi x}{\lambda}\left[\sin\alpha + m\lambda f_g\left(1-a_0\right)\right]\right) \times$$
$$\exp\left(-i\frac{mf_g a_1}{1/L}\sin\left(\frac{2\pi}{L/1}x\right)\right) \exp\left(-i\frac{mf_g a_2}{2/L}\sin\left(\frac{2\pi}{L/2}x\right)\right) \times$$
$$\exp\left(-i\frac{mf_g a_3}{3/L}\sin\left(\frac{2\pi}{L/3}x\right)\right) \cdots$$

$$= \sum_{m=-\infty}^{\infty}\sum_{r=-\infty}^{\infty}\sum_{s=-\infty}^{\infty}\sum_{t=-\infty}^{\infty} \cdots J_m\left(\frac{2\pi h}{\lambda}\right) J_r\left(-\frac{mf_g a_1}{1/L}\right) J_s\left(-\frac{mf_g a_2}{2/L}\right) J_t\left(-\frac{mf_g a_3}{3/L}\right) \cdots \times$$
$$\exp\left(\frac{i2\pi x}{\lambda}\left[\sin\alpha + m\lambda f_g\left(1-a_0\right) + r\lambda/L + s2\lambda/L + t3\lambda/L \cdots\right]\right) \qquad (7.14)$$

A graphical representation of Eq. 7.14 is shown in Fig. 7.3. It is to be noted that more mini orders appear due to the more general representation of strain distribution using the trapezoid.

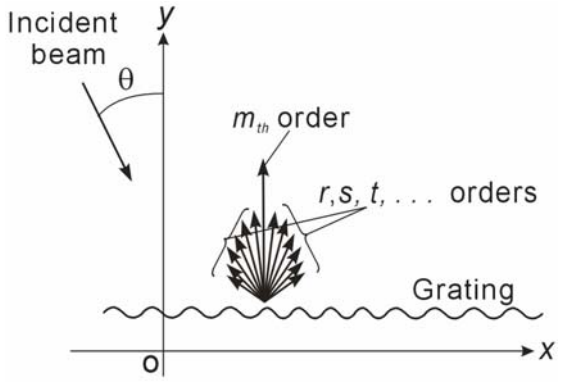

Figure 7.3 Diffracted beam and its mini-order of a grating by trapezoid-shaped strain distribution.

For the general cases of strain distribution, there are infinite numbers of the summation indices for mini-orders. This makes the parametric study mathematically complicated. A more efficient approach is desired to handle the mini-orders effectively.

7.3 Fourier Transform of Diffraction Field

The Fourier transform of $f(x)$ in one dimension is defined as

$$\Im(f(x)) = F(s) = \int_{-\infty}^{\infty} f(x)\exp(-i2\pi sx)dx \tag{7.15}$$

where $\Im()$ represents the Fourier transform and s is a spatial coordinate. The Fourier transform of the complex field distribution across the aperture can evaluate the diffraction pattern in the spatial-frequency spectrum with the Fraunhofer approximation [Goodman 1968, Hecht 1998].

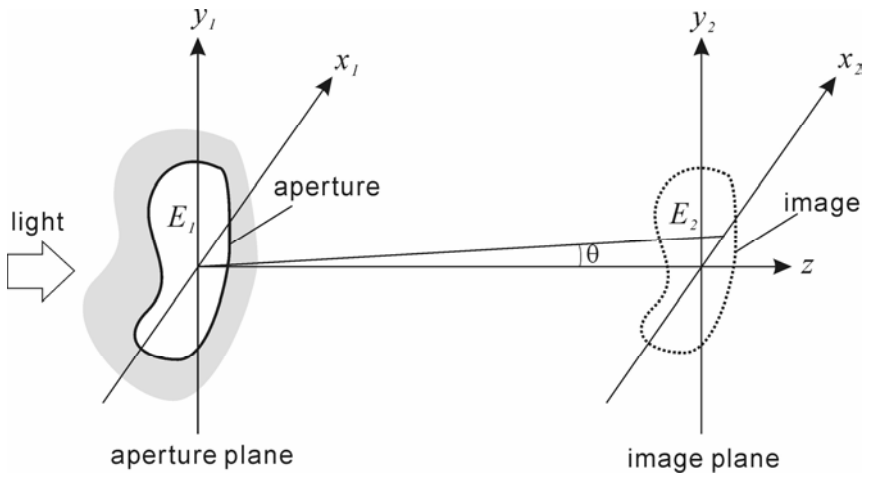

Figure 7.4 Diffraction and Fourier transform [Goodman 1968].

An aperture is illuminated by a monochromatic light, the diffracted field E at z distance from the aperture plane (Fig. 7.4) can be expressed by the Fraunhofer diffraction theory as [Goodman 1968]

$$E_2(x_2) = \frac{\exp(ikz)\exp\left(ik\frac{x_2^2}{2z}\right)}{i\lambda z}\int_{-\infty}^{\infty} E_1(x_1)\exp\left(-i2\pi\frac{x_2}{\lambda z}x_1\right)dx_1 \tag{7.16}$$

where λ is the wavelength of the light and k is the wave number defined as $2\pi/\lambda$. Note that Eq. 7.16 was derived for the 1-dimensional space but an extension to the 2-dimensional space is straightforward. Apart from the multiplication term preceding the integral, Eq. 7.16 is simply the Fourier transform of the complex field at the aperture plane, which can be evaluated at a spatial frequency, s, defined as

$$s = \frac{x_2}{\lambda z} = \frac{1}{\lambda}\tan\theta \tag{7.17}$$

As an example of this Fourier transform, the case of the sinusoidal strain distribution, (Eq. 7.5) is considered again. The complex field of the m_{th} order diffraction beam across the deformed grating is written here again from Eq. 7.9

$$E_d\big|_m = \sum_{r=-\infty}^{\infty} J_m\left(\frac{2\pi h}{\lambda}\right)J_r\left(\frac{mbf_g}{f_s}\right)\exp\left(\frac{i2\pi x}{\lambda}\left(\sin\alpha + m\lambda f_g + r\lambda f_s\right)\right) \tag{7.9}$$

With the condition of Eq. 6.4, Eq. 7.9 can be written as

$$E_d\big|_m = \sum_{r=-\infty}^{\infty} J_m\left(\frac{2\pi h}{\lambda}\right)J_r\left(\frac{mbf_g}{f_s}\right)\exp\left(i2\pi x\left(rf_s\right)\right) \tag{7.18}$$

The Fourier transform of Eq. 7.18 is

$$\begin{aligned}\Im\left(E_d\big|_m\right) &= \sum_{r=-\infty}^{\infty} J_m\left(\frac{2\pi h}{\lambda}\right) J_r\left(\frac{mbf_g}{f_s}\right) \Im\left(\exp\left(i2\pi x\left(rf_s\right)\right)\right) \\ &= \sum_{r=-\infty}^{\infty} J_m\left(\frac{2\pi h}{\lambda}\right) J_r\left(\frac{mbf_g}{f_s}\right) \delta\left(s - rf_s\right)\end{aligned} \tag{7.19}$$

where $\delta(s)$ is the Dirac delta function.

To illustrate Eq. 7.19, the following case of moiré interferometry practice was considered; h (groove depth) = 200 nm, λ (wavelength) = 633 nm, f_g (grating frequency) = 1200 lines/mm, m (diffraction order) = 1, f_s (strain cycle) = 0.1 cycles/mm, and b (peak strain) = 0.1 %. Figure 7.5 plots the result. The value on the abscissa represents the spatial frequency multiplied by the wavelength, which becomes the angle of the mini-order in degrees when the angles are small; i.e., $s\lambda = \tan\theta \approx \theta \frac{\theta}{\lambda}$. The value on the ordinate represents the magnitude of the mini-order, or $\left| J_m\left(\frac{2\pi h}{\lambda}\right) J_r\left(\frac{mbf_g}{f_s}\right)\right|$.

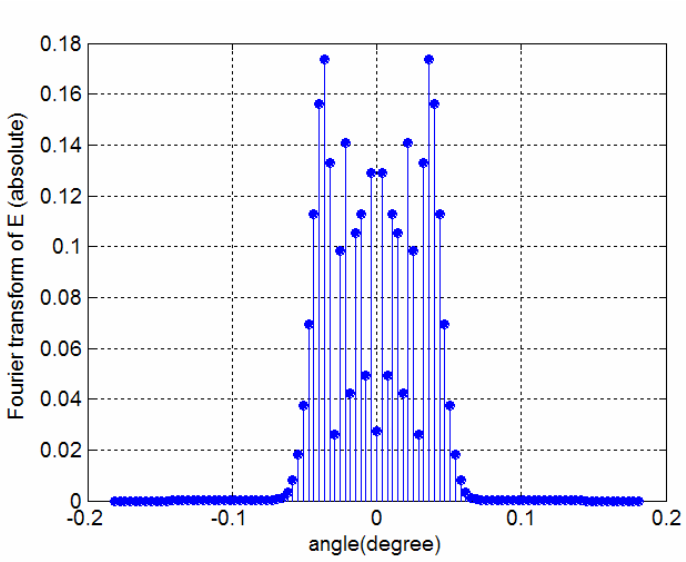

Figure 7.5 Example of Fourier transform for a deformed grating with a sinusoidal-strain distribution.

Figure 7.5 clearly demonstrates that the characteristics of the mini-orders can be analyzed effectively using the Fourier transform. It is extended to the general strain distribution. From Eq. 7.14, the complex field of the m_{th} order diffraction from the deformed grating with the trapezoid-shaped strain distribution can be written as

$$E_d\big|_m = \exp\left(\frac{i2\pi}{\lambda} x \sin\alpha\right) \times \\ J_m\left(\frac{2\pi h}{\lambda}\right) \exp\left(im2\pi f_g\left(1-a_0\right)x\right) \exp\left(imf_g\left(-\sum_{k=1}^{\infty}\frac{a_k L}{k}\sin\left(\frac{2k\pi}{L}x\right)\right)\right) \tag{7.20}$$

The Fourier transform of Eq. 7.20 is analytically possible after decomposing it into infinite series using *Jacobi-Anger expansion* but the Fourier transform will have an infinite series of functions, which makes the parametric study impractical. In the

following section, discrete Fourier transform is introduced to obtain the Fourier transform numerically.

7.4 Numerical Approach Using Discrete Fourier Transform

The discrete Fourier transform is an approximation of the continuous Fourier transform developed to calculate the transform of digital data. Figure 7.6 (a) illustrates the example function $h(t)$ and its continuous Fourier transform $H(f)$. It is required to modify this Fourier transform pair in such a manner that the pair is amenable to digital computation. This modified pair, termed the discrete Fourier transform, is to closely approximate the continuous Fourier transform.

To determine the Fourier transform of $h(t)$ by means of digital technique, the initial step is to sample $h(t)$ in discrete points. Sampling is accomplished by multiplying $h(t)$ by the sampling function, as illustrated in Fig. 7.6 (b), where the sample interval is T. The sampled function and its Fourier transform are illustrated in Fig. 7.6 (c). The Fourier transform of the sampled function is conducted through convolution theory, which is denoted by '*' in the figure. Note that the modified transform pair differs from the original transform pair only by the *aliasing* effect that results from sampling. If the spatial spectrum of function $h(x)$ is band-limited, faster sampling can eliminate aliasing [Brigham 1974].

Because only a finite number of points can be calculated by digital computation, it is necessary to truncate the sampled function $h(t)$ so that only a finite number of points, say N, can be considered. The truncation function and its Fourier transform are illustrated in Fig. 7.6 (d). The product of the infinite sequence of impulse functions representing $h(t)$ and the truncation function yields the finite length time function as

shown in Fig. 7.6 (e). Truncation introduces the second modification to the original Fourier transform of pair; this effect is to convolve the aliased frequency transform of Fig. 7.6 (c) with the Fourier transform of the truncation function in Fig. 7.6 (d). As shown in Fig. 7.6 (e), the frequency transform has a *ripple* on it. If the function $h(t)$ is periodic and the size of truncation T_0 is exactly one period of $h(t)$, the rippling can be eliminated [Brigham 1974].

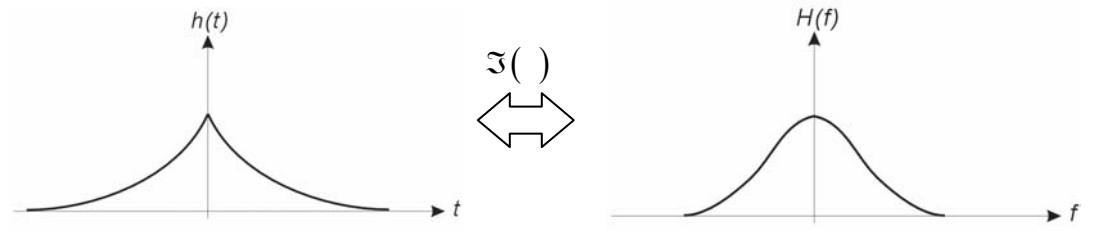

(a)

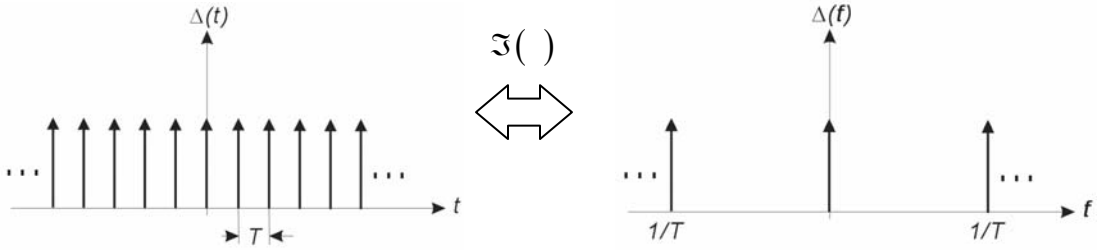

(b)

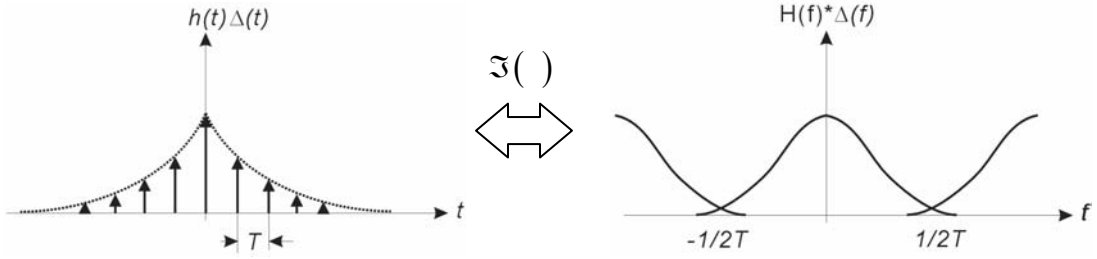

(c)

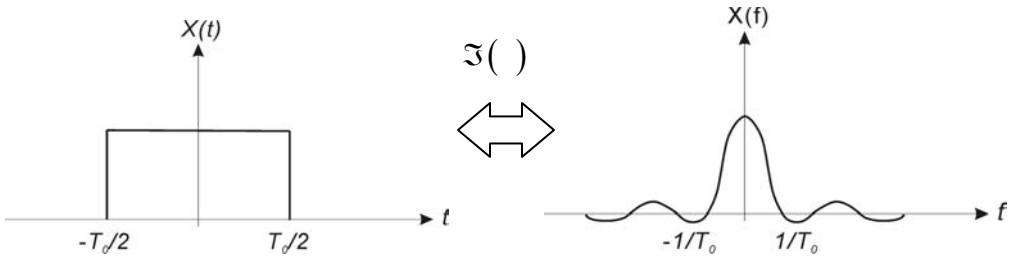

(d)

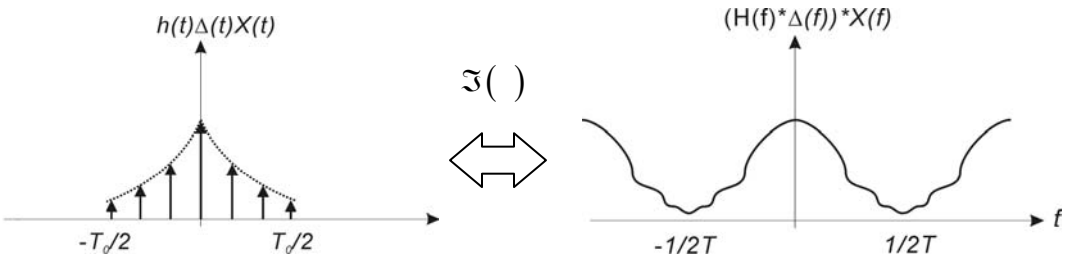

(e)

Figure 7.6 Relation of Fourier transform and discrete Fourier transform [Brigham 1974].

The formation of the discrete Fourier transform for function $f(x)$ can be written as [Brigham 1974]

$$\Im\left(f\left(\frac{n}{NT}\right)\right)=\sum_{k=0}^{N-1}f\left(kT\right)\exp\left(-i2\pi nk/N\right),\quad n=0,1,\cdots N-1 \tag{7.21}$$

where T is the sampling interval and N is the total number of samples.

The difference between the two transforms, Eqs. 7.15 and 7.21, arises due to the discrete transform requirement for sampling and truncation. Equivalence of the two transforms requires that the following conditions must be met [Brigham 1974];

1) From the sampling theory, the function $f(x)$ should be sampled at a frequency of as least twice the largest frequency component of $f(x)$ not to lose information as a result of sampling.
2) The Fourier transform of $f(x)$ must be band-limited to avoid aliasing.
3) $f(x)$ must be periodic.
4) The size of truncation must be one period (or integer multiple period) of $f(x)$.

The spatial spectrum of the diffracted complex field lies within a very small angular bandwidth. The defined strain distribution in Sec. 7.2 is periodic and the size of truncation can be chosen as the period of the strain distribution. Consequently, the discrete Fourier transform of the diffracted complex field will be equivalent to its continuous Fourier transform as long as the sampling rate is sufficiently large.

7.5 Parametric Study to Characterize the Mini-order

A numerical study was conducted to characterize the mini-orders for the trapezoid-shaped strain distribution. With the condition of Eq. 6.4 in moiré interferometry, Eq. 7.20 can be rewritten as

$$E_d\big|_m = J_m\left(\frac{2\pi h}{\lambda}\right)\exp\left(-i2\pi m f_g\left(a_0 x + \sum_{k=1}^{\infty}\frac{a_k L}{2\pi k}\sin\left(\frac{2k\pi}{L}x\right)\right)\right) \tag{7.22}$$

where a_0 and a_k are defined in Eq. 7.10. Discrete Fourier transform of Eq. 7.22 was conducted through the FFT algorithm available in *Matlab*. The *Matlab* code used in the analysis can be found in Appendix B.

7.5.1 Convergence Check of FFT

As discussed in the previous section, the discrete Fourier transform of the diffracted complex field of Eq. 7.21 is equivalent to the continuous Fourier transform only when the sampling rate is sufficiently large. In order to determine a proper sampling rate, convergence has been tested for the case of c = 0.5 %, d = 0.2 %, L = 5 mm, a = 1 mm, and b = 1.5 mm; other parameters include f_g = 1200 lines/mm, m = 1, h = 200 nm, and λ = 633 nm. Figure 7.7 (a) illustrates the strain distribution and the corresponding displacement distribution and fringe pattern are shown in (b) and (c), respectively. Note that only half of a period is shown in Fig. 7.7 due to the symmetry.

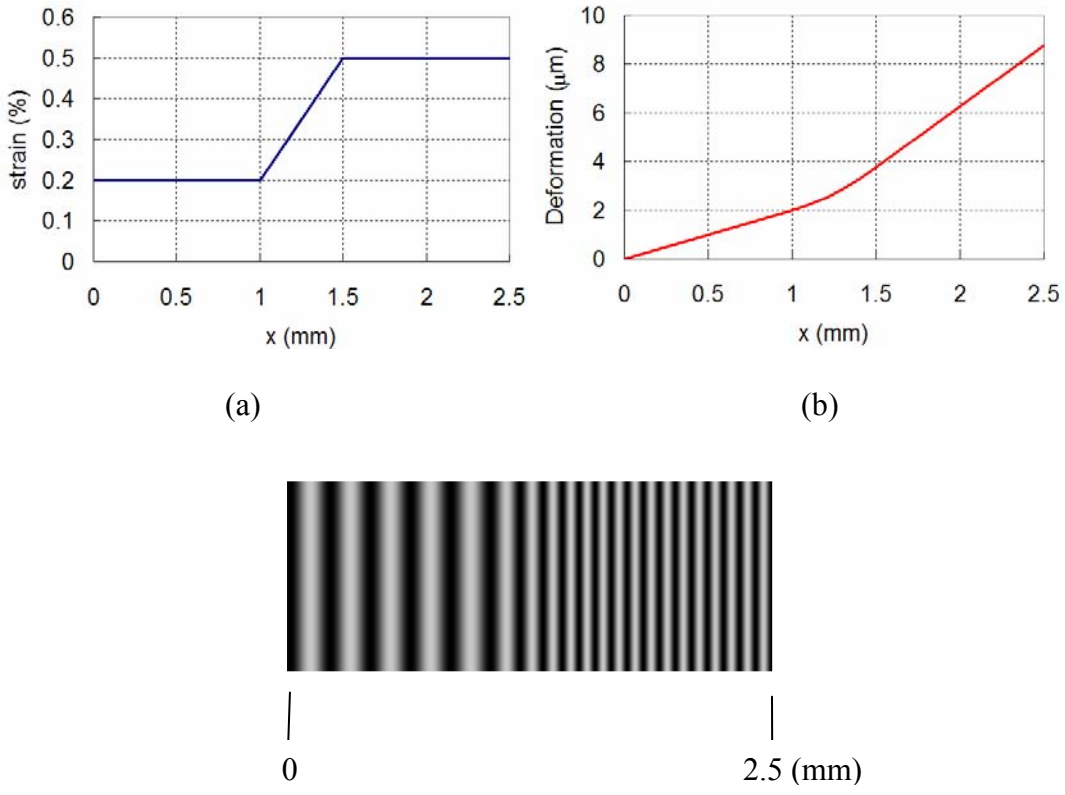

Figure 7.7 Deformation field used for convergence test; (a) strain distribution, (b) displacement distribution, and (c) theoretical fringe pattern.

The FFT results are shown in Fig. 7.8, where sampling numbers of 50, 100, 200, 500, and 1,000 were used. The value on the abscissa represents the angle of the mini-order in degrees and the value on the ordinate represents the magnitude of the mini-order. It is clear from the figure that the angle and the magnitude converge as the sampling number, N, increases.

The convergence study is summarized in Fig. 7.9. In the figure, the x-coordinate represents the sampling number on a log scale and the y-coordinate represents the

amount of deviation of the each transform from the results of N = 1,000. If the sampling number is larger than 200, the deviation is almost negligible. The sampling number of 1,000 was used for the subsequent parametric study.

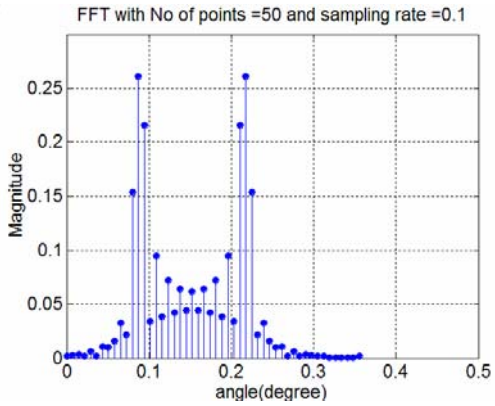

(a)

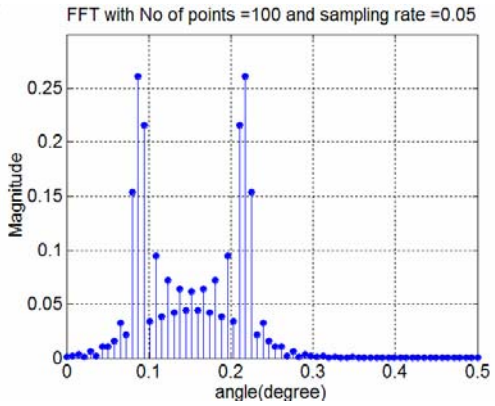

(b)

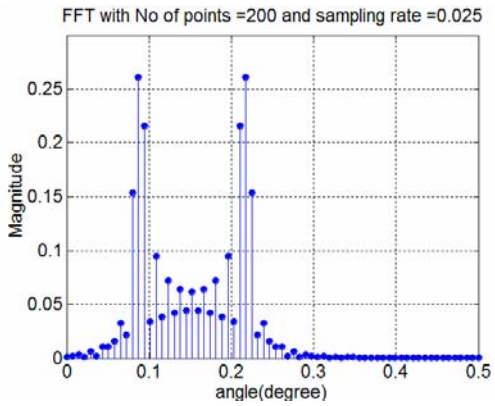

(c)

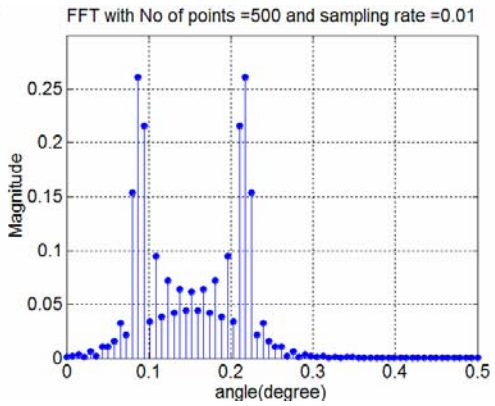

(d)

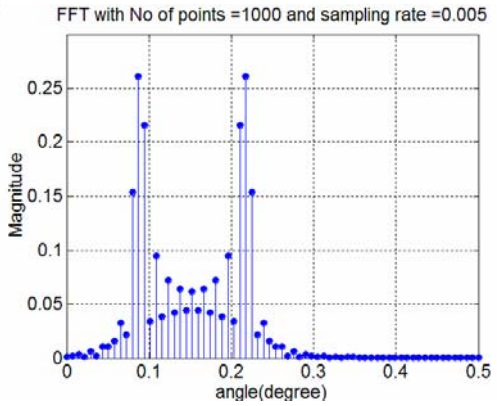

(e)

Figure 7.8 Results of the FFT for the diffracted complex field for the trapezoid-shaped strain with N = (a) 50, (b) 100, (c) 200, (d) 500, and (e) 1,000. The parameters to define the strain field are c = 0.5 %, d = 0.2 %, L = 5 mm, a = 1 mm, and b = 1.5 mm. Other parameters include f_g = 1200 lines/mm, m = 1, h = 200 nm, λ = 633 nm.

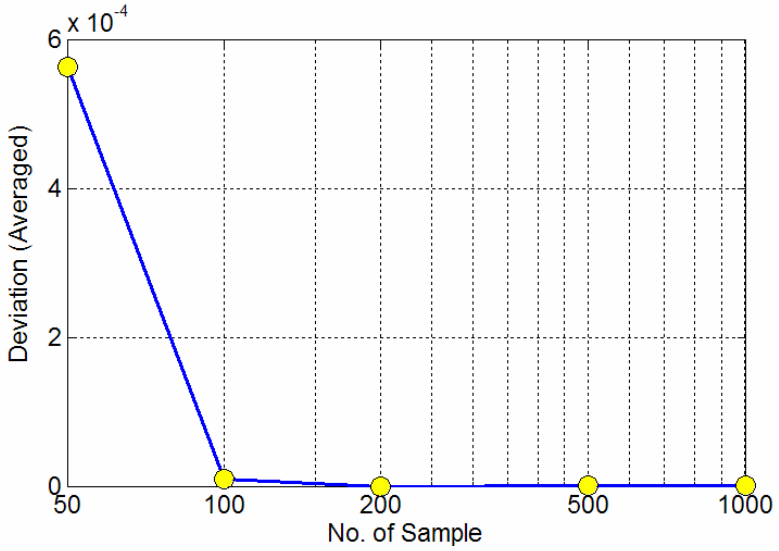

Figure 7.9 Results of convergence test.

7.5.2 Parametric Study: Period of Strain

The trapezoid-shaped strain distribution has a period of L. The period was introduced for the mathematical purpose. By making the period approach to infinite, a local strain variation can be emulated. The effect of the period on the mini-orders is studied here.

Figure 7.10 illustrates various periods of strain used in the analysis; L is (a) 5 mm, (b) 10 mm, (c) 20 mm, and (d) 40 mm. The maximum and minimum strains are 0.5% and 0.2%, respectively (c = 0.5 % and d = 0.2 %) and the width (b-a) between the strain is selected as 0.5 mm. Note that the plots in Fig. 7.10 are made only for half of the period due to the symmetry and that the scales of x in the figure are all different, depending on L. Figure 7.11 shows the FFT results for the different strain periods.

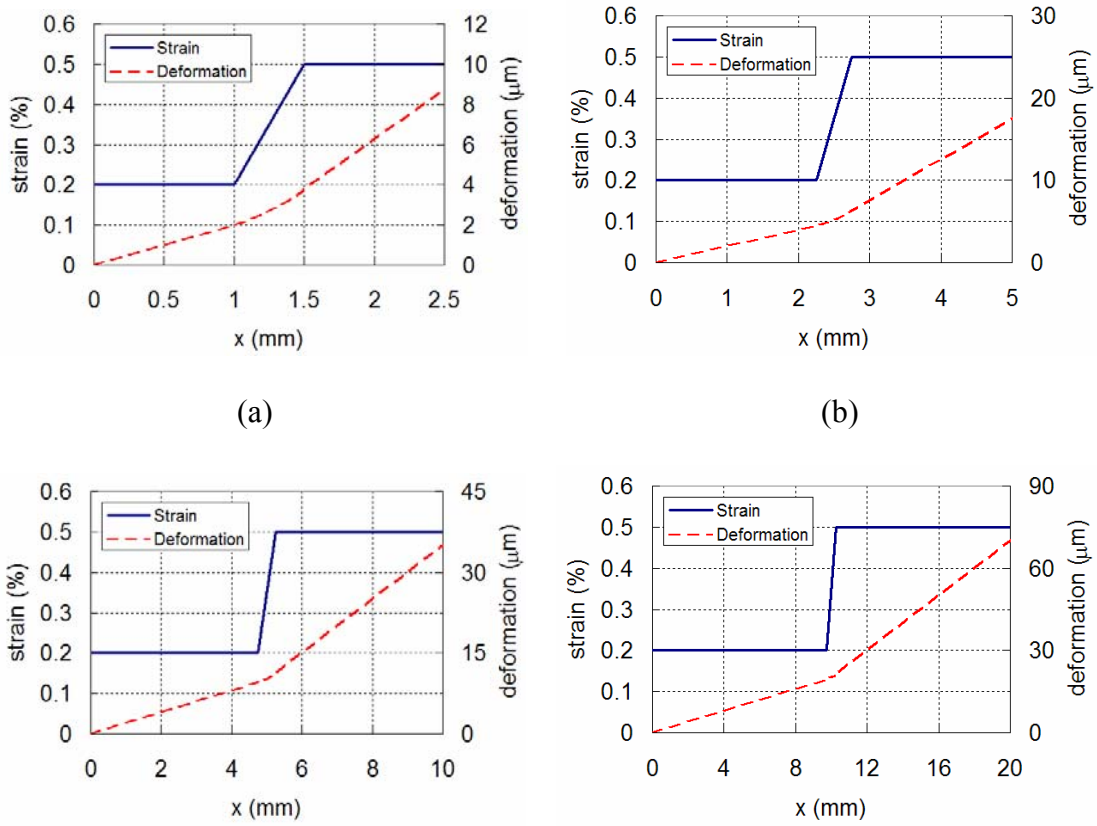

Figure 7.10 Strain distributions for the parametric study; b - a = 0.5 mm, c = 0.5%, d = 0.2%, and L = (a) 5 mm, (b) 10 mm, (c) 20 mm, and (d) 40 mm.

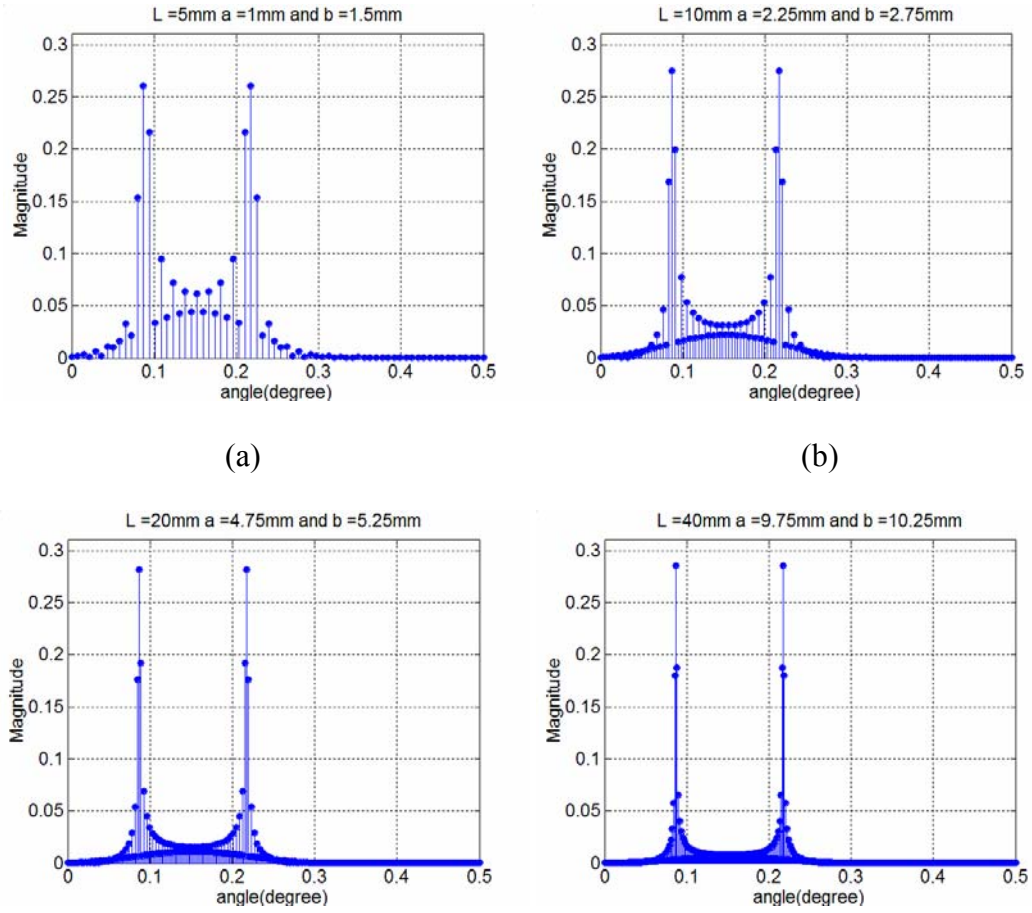

Figure 7.11 Results of the parametric study; b - a = 0.5 mm, c = 0.5%, d = 0.2%, and L = (a) 5 mm, (b) 10 mm, (c) 20 mm, and (d) 40 mm.

As the period increases, the shapes of mini-order are changing but the maximum magnitudes of mini-order are located around 0.09° and 0.22° for all the cases. The magnitude ratio between the maximum and other mini-orders increases with the period of strain. It is important to note that the range of effective mini-order, which eventually contributes the formation of the fringes in moiré interferometry, remains unchanged regardless of the strain period.

7.5.3 Parametric Study: Strain Gradient

Figure 7.12 shows the strain distributions with different gradients used in the parametric study; c = 0.5 %, d = 0.2 %, and L = 40 mm, but the width (b-a) between the strain varies from (a) 0, (b) L/10, (c) L/4 to (d) L/2. The FFT results of the different strain gradients are shown in Fig. 7.13.

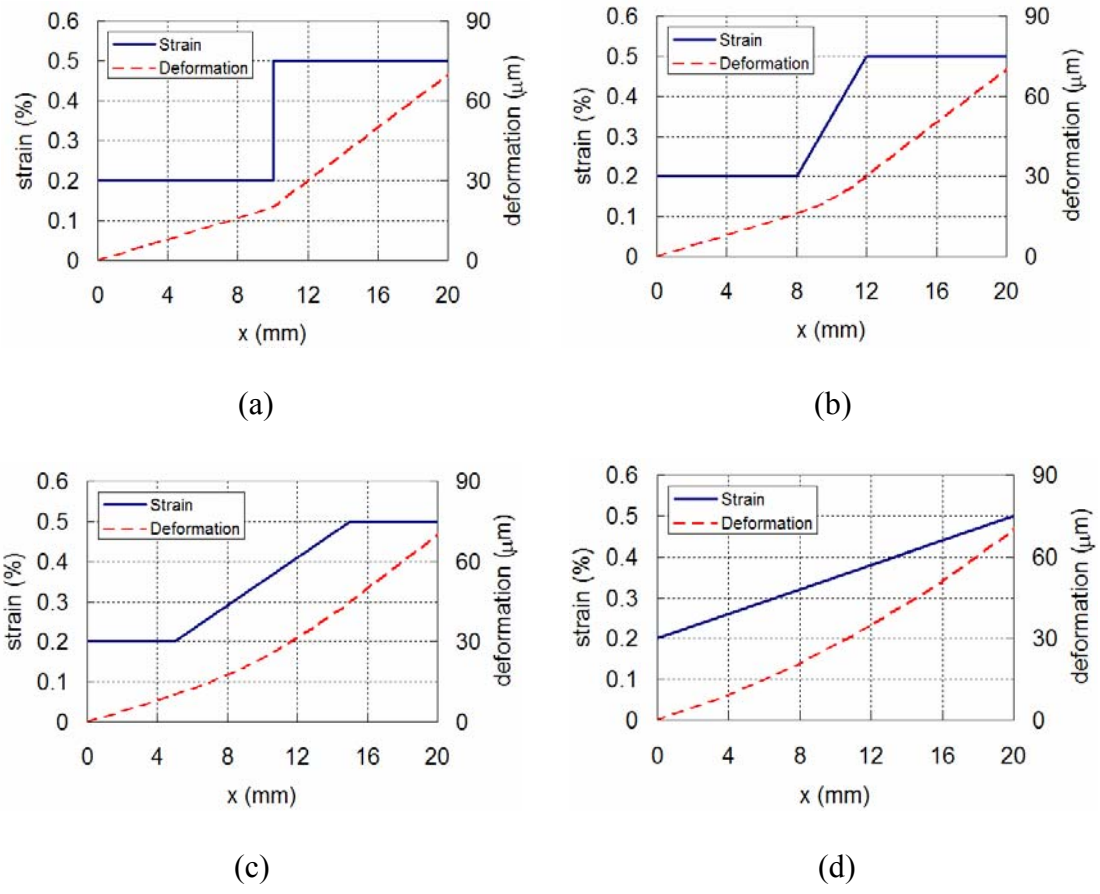

Figure 7.12 Strain distributions for the parametric study; L = 40 mm, c = 0.5%, d = 0.2%, (a +b)/2 = L/4, and the width between the strain = (a) 0, (b) L/10, (c) L/4, and (d) L/2.

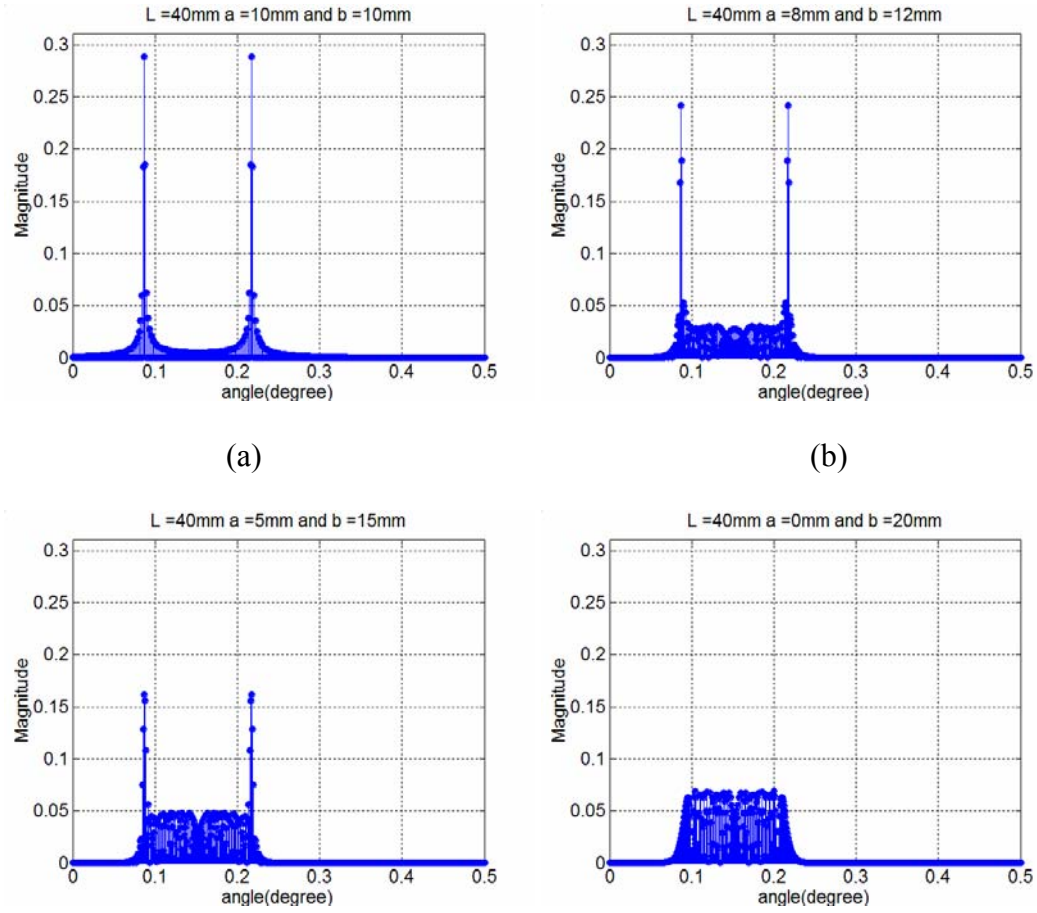

(a) (b)

(c) (d)

Figure 7.13 Results of the parametric study; L = 40 mm, c = 0.5%, d = 0.2%, (a +b)/2 = L/4, and the width between the strain = (a) 0, (b) L/10, (c) L/4, and (d) L/2.

As the strain gradient decreases (Fig. 7.12 (a) to (d)), the magnitudes at the two maximum mini-orders, which occur around 0.09° and 0.22°, decrease but the magnitudes of the mini-orders between them increase. For the case of a linearly varying strain (Fig. 7.12(d)), the magnitudes of the mini-orders become nearly the same. It is worth noting that the strain gradient does not alter the range of effective mini-orders (approximately 0.05° to 0.25° for this case) even though it affects the ratio between the magnitudes of mini-orders.

7.5.4 Parametric Study: Ratio of Strain Width

Figure 7.14 shows the strain distributions with four different values of width; c = 0.5%, d = 0.2 %, $b - a$ = 4 mm, and L = 40 mm. However the ratio between the widths of the maximum and minimum strains (c and d) varies from (a) 3, (b) 1, (c) 1/3 to (d) 0. The FFT results for the different strain width ratios are shown in Fig. 7.15.

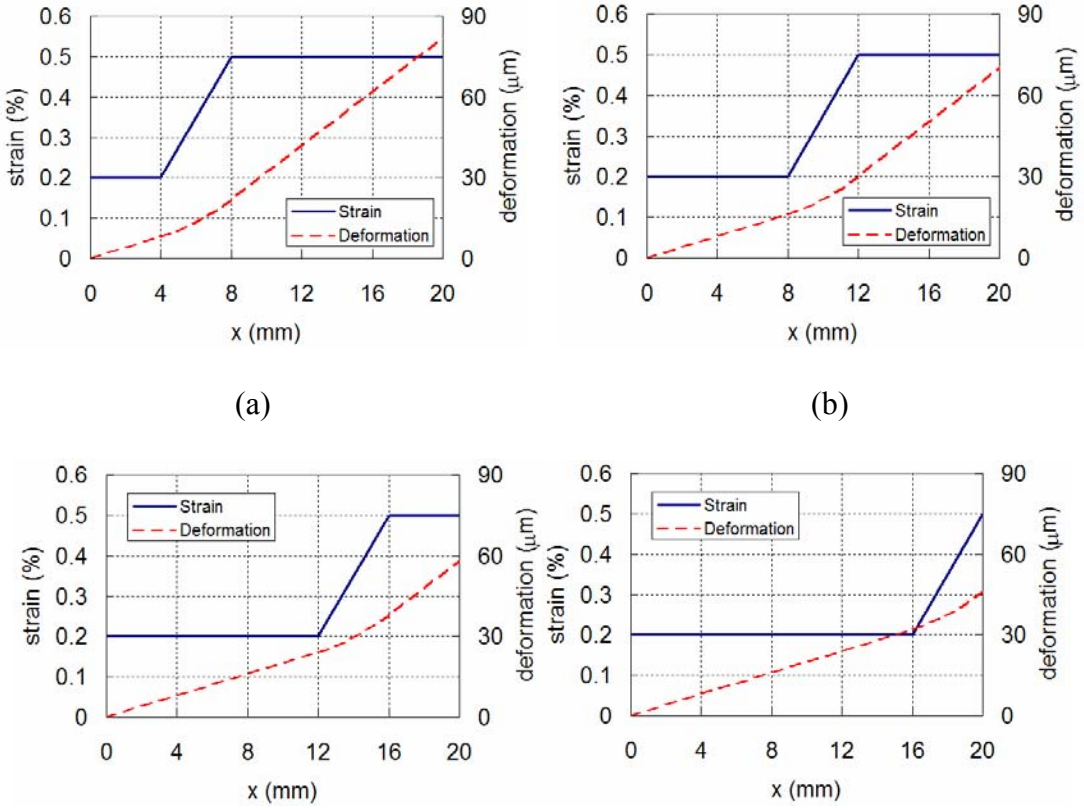

Figure 7.14 Strain distributions for the parametric study on the ratio of strain width; L = 40 mm, c = 0.5%, d = 0.2%, b - a = 4 mm, and a = (a) 4 mm, (b) 8 mm, (c) 12 mm, and (d) 16 mm.

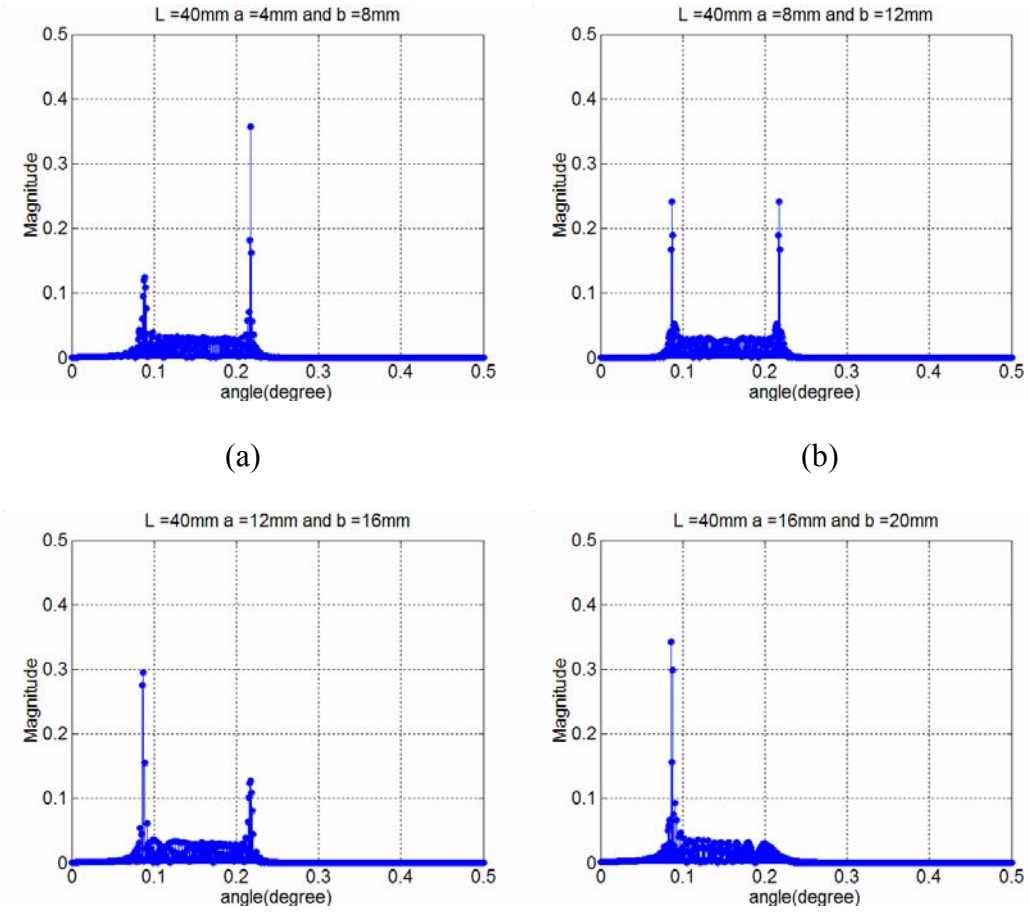

Figure 7.15 Results of the parametric study on the ratio of strain width; L = 40 mm, c = 0.5%, d = 0.2%, b - a = 4 mm, and a = (a) 4 mm, (b) 8 mm, (c) 12 mm, and (d) 16 mm.

The results of Fig. 7.15 indicate that only the ratio between the magnitudes of the two maximum mini-orders changes proportionally as the ratio between the widths of the maximum and minimum strains change.

7.5.5 Parametric Study: Magnitude of Strain

Finally, the effect of strain magnitude on the mini-order is investigated. Figure 7.16 shows the four different strain distributions. All of them have the same L of 40 mm, the ramp (b - a) of 4 mm, and the strain width ratio of 1, but (a) c = 0.5 % and d = 0.2 %, (b) c = 0.2 % and d = 0.5 %, (c) c = 1.0 % and d = 0.2 %, and (d) c = 0.5 % and d = 0.1 %. The FFT results of these four cases are shown in Fig. 7.17.

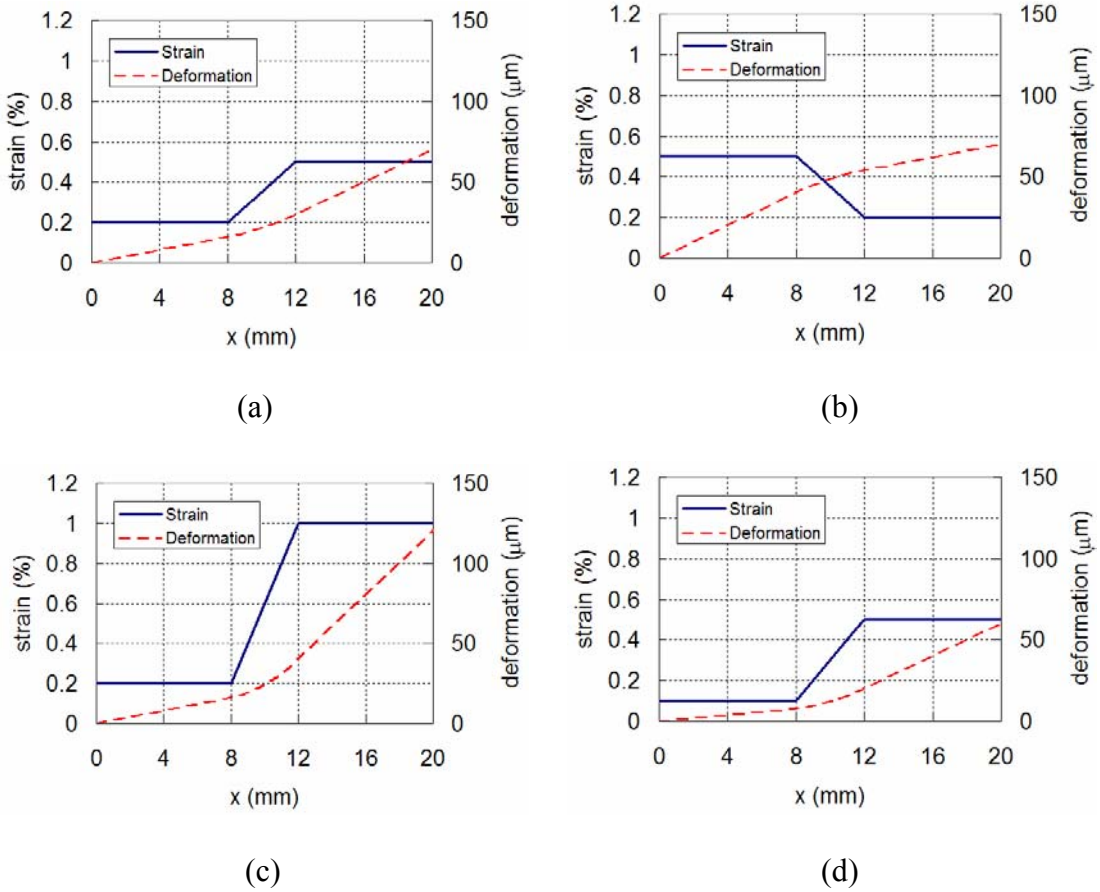

Figure 7.16 Strain distributions for the parametric study on the strain magnitude; L = 40 mm, a = 8 mm, b = 12 mm with (a) c = 0.5 % and d = 0.2 %, (b) c = 0.2 % and d = 0.5 %, (c) c = 1.0 % and d = 0.2 %, and (d) c = 0.5 % and d = 0.1 %.

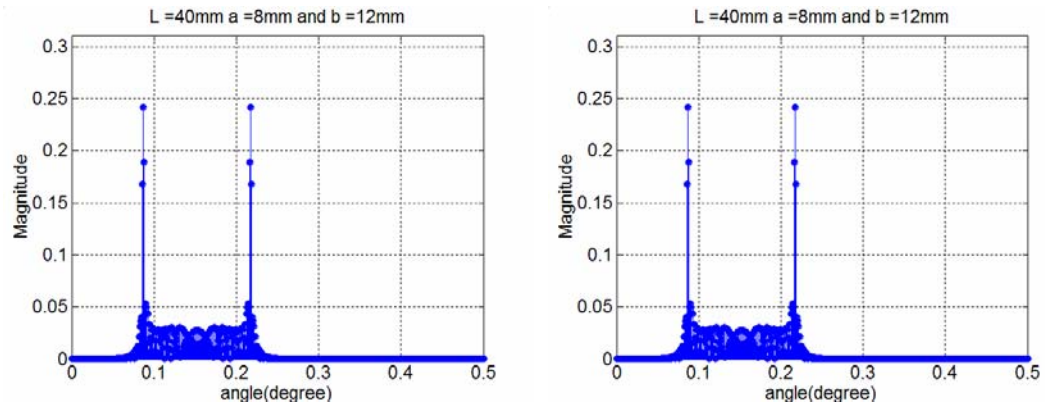

(a) (b)

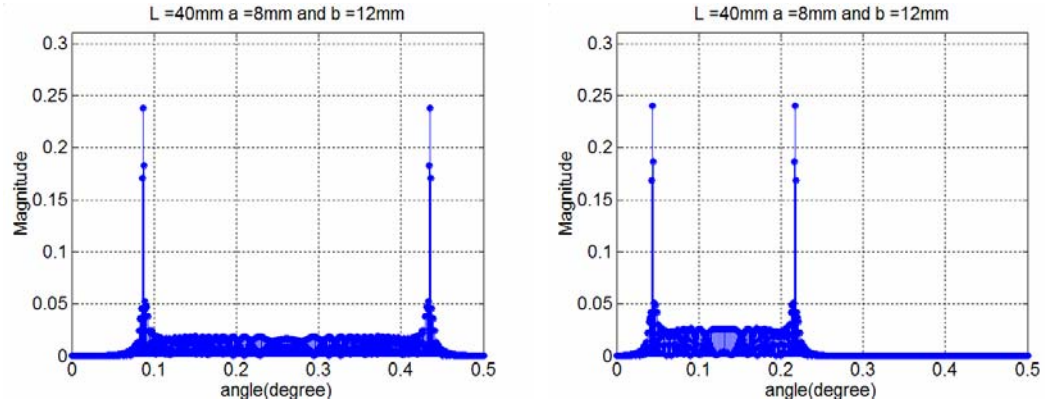

(c) (d)

Figure 7.17 Results of the parametric study on the strain magnitude; L = 40 mm, a = 8 mm, b = 12 mm with (a) c = 0.5 % and d = 0.2 %, (b) c = 0.2 % and d = 0.5 %, (c) c = 1.0 % and d = 0.2 %, and (d) c = 0.5 % and d = 0.1 %.

Figure 7.17 (a) and (b) represent the mini-order for two cases where the magnitudes of the maximum and minimum strains are opposite; (a) c = 0.5 % and d = 0.2 %, (b) c = 0.2 % and d = 0.5 %. The results are nearly identical. The effect of different strain magnitudes are shown in (c) and (d); (c) c = 1.0 % and d = 0.2 %, and (d) c = 0.5 % and d = 0.1 %. The range of the mini-orders, which is defined as the difference

between the angles of two peak mini-orders, is linearly proportional to the difference between the maximum and minimum strain magnitudes.

From the results of the parametric studies using a trapezoid-shaped strain distribution, the following observations were made;

1) The period of strain, the strain gradient, and the ratio of strain width affect the magnitudes of mini-orders, but not the range of mini-orders.
2) Only the strain magnitude controls the range of mini-orders

The range of min-orders is directly related to the fringe formation since the aperture of the imaging system in moiré interferometry is finite. This effect is discussed in the following section.

7.6 Numerical Aperture and Measurable Maximum Strain

From the parametric studies, the angle of mini-order can be defined as

$$\sin\theta_{\text{mo}} = m\lambda f_g b \tag{7.23}$$

where θ_{mo} is the angle of the mini-order, m is the diffraction order, λ is the wavelength, f_g is the frequency of the specimen grating, and b is the strain magnitude.

Numerical aperture (*N.A.*) of an imaging system is defined as

$$N.A. = \sin\theta_{\max} \tag{7.24}$$

where $\theta_{\max}$ is the maximum angle of emerging beam that the imaging system can capture [Hecht 1998].

By combining Eqs. 7.23 and 7.24, the maximum measurable strain, $b_{\max}$, can be expressed as

$$b_{\max} = \frac{N.A.}{m\lambda f_g} \tag{7.25}$$

In routine practice of moiré interferometry, m =1, f_g = 1200 line/mm, and λ = 633 nm. The maximum measurable strain as a function of N.A. is plotted in Fig. 7.19. It is clear from the results that more than $\pm$10% of strain can be readily measured with only *N.A.* of 0.1.

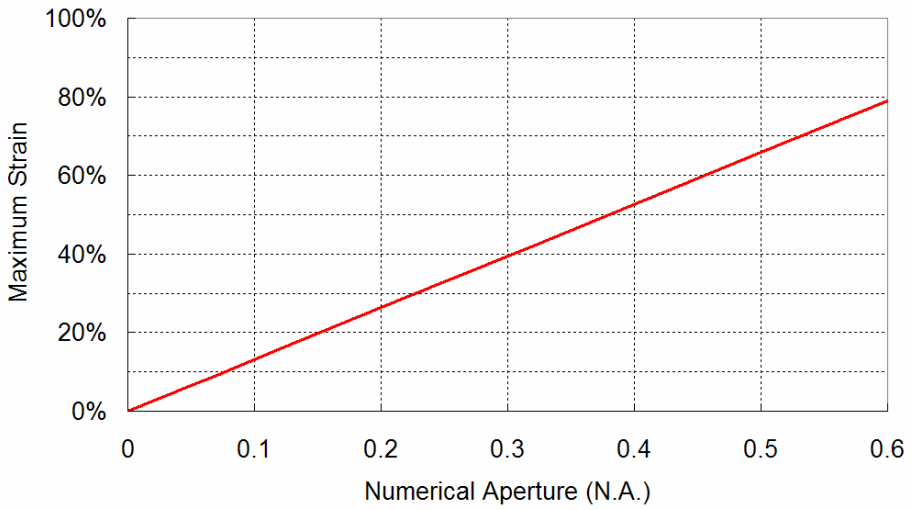

Figure 7.18 Maximum measurable strain as a function of the numerical aperture of an imaging system, where m =1, f_g = 1200 line/mm, and λ = 633 nm.

Chapter 8. Conclusions

In Part I, an extensive study for the contrast and intensity of shadow moiré fringe was conducted. The results were utilized to develop high sensitivity shadow moiré using the non-zero Talbot distance (SM-NT).

In Part II, the diffraction grating theory and Fourier optics were applied to moiré interferometry to explain the phase-shifting in an achromatic system. The theory was extended to characterize the mini-order for a general strain distribution in this dissertation.

The major contributions made in this dissertation include:

1) Developed an exact solution of the contrast and intensity distribution of shadow moiré fringe for a monochromatic light source based on a diffraction theory
2) Conducted an experiment to validate the Talbot contrast of shadow moiré fringe.
3) Evaluated the effect of a broad spectrum light source on the Talbot contrast of shadow moiré fringes.
4) Developed and experimentally validated a complete expression for the contrast of shadow moiré fringes.
5) Developed the intensity function of shadow moiré fringe for a broad spectrum.
6) Evaluated the systematic error of the phase-shifting technique, caused by the non-sinusoidal intensity distribution of shadow moiré.

7) Developed high sensitivity shadow moiré using non-zero Talbot distance (SM-NT) system.
8) Suggested the optical configurations of SM-NT for the optimum fringe contrast and applied them to the warpage measurement of FC-PBGA.
9) Explained the phase-shifting in an achromatic system of moiré interferometry using the diffraction grating theory and Fourier optics.
10) Developed a mathematical model to analyze the mini-orders for a general strain distribution, where the discrete Fourier transform was employed to characterize the mini-orders.

Appendices

Appendix A. Matlab Program to Calculate the Phase Change in Achromatic System

```
clear all;

H=0.1;                  %H: Depth of Gloove (micro meter)
d=1/1.2;                %d: pitch of grating(micro meter): 1200 lines/mm
hc=pi*H/d               %hc: should be less than 0.447743

lambda=.35              %lambda: wavelength of beam
theta=0                 % theta : incidence angle

k=2*pi/lambda;
alpha=k*sin(theta);
betta=k*cos(theta);

N=30 %Number of n

x=linspace(0,d,2*N+1);

shift=0;
e=-H/2;

A=zeros(2*N+1);
for m=-N:N
   for l=-N:N

A(m+N+1,l+N+1)=exp(i*alpha_n(k,theta,l,d)*x(m+N+1)+i*betta_n(k,theta,l,d)*(H/2*cos(2*pi/d*
(x(m+N+1)-shift))+e));
      %Phi(k,theta,l,d,H,x(m+N+1));
   end
end


C=zeros(2*N+1,1);
for m=-N:N
      C(m+N+1)=-exp(i*alpha*x(m+N+1)-i*betta*(H/2*cos(2*pi/d*(x(m+N+1)-shift))+e));
end

B=inv(A)*C;  %Coefficient

theta_n=zeros(2*N+1,1);
for n=-N:N
   theta_n(n+N+1)=asin(sin(theta)+n*lambda/d);
end
theta_n*180/pi %Show in degrees

%Efficiency
```

```
E= B.*conj(B).*cos(theta_n)/cos(theta);

%-------------------------------------------------------------------------
%Plot Mode
x=linspace(0,3*d);
y=linspace(H/2+e,3*lambda);

Order=input('Order?')
%Order=100;
while Order ~= 100
   figure
   BG=B(Order+N+1)
   alphaG=alpha_n(k,theta,Order,d)
   bettaG=betta_n(k,theta,Order,d)

         for l=1:length(x)
      for m=1:length(y)
         z(m,l)=real(BG*exp(i*alphaG*x(l)+i*bettaG*y(m)));
      end
         end

   phase=angle(BG)*180/pi
   %figure
         hold on
         plot(x,H/2*cos(2*pi/d*(x-shift))+e,'k','LineWidth',2)


         contourf(x,y,z)
  colormap(gray);
         axis equal
   xlabel('x')
   ylabel('y')
   title(['Order : ',int2str(Order),'. Grating shift : d/4'])
         hold off
   Order=input('Order?')
end
```

Appendix B. Matlab Program to Evaluate the Mini-order Using FFT

```
clear

order=1;                % diffraction order of beam 1
fg=1200;                % frequency of specimen grating (lines/mm)
h=200e-6;               % groove depth of grating (mm)
lambda=633e-6;          % wavelength (mm): He-Ne 633nm

a=1;                    % strain point 1 (mm)
b=1.5;                  % strain point 2 (mm)
L=5;                    % pitch of periodic strain (mm)

c=0.005;                % maximum strain
d=0.002;                % minimum strain

T=L/10000               % Sampling Rate
n=0:(L/T)-1;            % sampling index
N=length(n)             % Number of sampling

B=zeros(size(n));       % For diffraction complex field

a0=((d-c)*(b+a)+L*c)/L;

for k=1:500
   if a==b              % if a = b, or step function
      B=B+2*(d-c)/(k*pi)*sin(2*k*pi*b/L)*L/2/k/pi*sin(2*k*pi/L*n*T);
   else                 % Trapezoidal case
      B=B+(c-d)/(b-a)*L/(k*pi)^2*(cos(2*k*pi*b/L)-cos(2*k*pi*a/L))* ...
         L/2/k/pi*sin(2*k*pi/L*n*T);
   end
end

% Complex Amplitude
CA=besselj(order, 2*pi*h/lambda)*exp(i*2*pi* order*fg *(a0*n*T+B));
F_CA=fft(CA);       % FFT

stem(atan(n/(T*N)*lambda)*180/pi,1/N*abs(F_CA),'filled')
set(GCA,'fontsize',14)
set(GCA,'FontName','Arial')
xlabel('angle(degree)')
ylabel('Magnitude')
grid on
axis([0,0.5,0,0.3])
title(['FFT with No of points =',num2str(N),' and sampling rate =', num2str(T)])
```

Reference

1. Ackerman, C.W., "Development of a Real-time High Sensitivity Shadow Moiré System and its Application to Microelectronics Packaging" *M.S. Dissertation*, Clemson University (2000).
2. Arai, Y. and Yokozeki, S., "Improvement of measurement accuracy in shadow moiré by considering the influence of harmonics in the moiré profile, *Applied Optics* **38**, 3503-3507 (1999).
3. Asundi, A and Chan, C. S., "Phase shifting applied to non-sinusoidal intensity distribution – an error simulation", *Optics and Lasers in Engineering* **21**, 3-30 (1994).
4. Brigham, E. O., *The Fast Fourier Transform*, Prentice-Hall, New Jersey (1974).
5. Chen, K., Chen, T. Y. F., Chuang, C. C., and Lin, I. K., "Full-field wafer level thin film stress measurement by phase-stepping shadow moiré", *IEEE Transactions on components and packaging technologies* **27**, 594-601 (2004).
6. Chiang, F.-P., "Moiré methods of strain analysis, Chap 7" in *Manual on Experimental Stress Analysis 5th ed*, J. F. Doyle and J. W. Phillips, eds. (Society for Experimental Mechanics, Bethel, CT., 1989).
7. Cho, S. and Han, B., "Effect of underfill on flip-chip solder bumps: an experimental study by microscopic moiré interferometry," *The International Journal of Microcircuits and Electronic Packaging* **24 (3)**, 217-239 (2002).
8. Cho, S.-M., Cho, S.-Y., and Han, B., "Observing real-time thermal deformations in electronic packaging," *Experimental Techniques* **26 (3)**, 25-29 (2002).

9. Cho, S.-M., Han, B., and Joo, J., "Temperature dependent deformation analysis of ceramic ball grid array package assembly under accelerated thermal cycling condition", *ASME Journal of Electronic Packaging* **126**, 41-47 (2004).
10. Creath, K., "Phase-measurement interferometry techniquess", in *Progress in optics Vol. XXVI*, E. Wolf, eds.(North-Holland, Amsterdam), 349-393 (1988).
11. Dai, F. L., McKelvie, J., and Post, D., "An interpretation of moire interferometry from wavefront interference theory" *Optics and Lasers in Engineering* **12,** 101-118 (1990).
12. Dang, A. X. H., Ume. I. C., Bhattacharya, S. K., "Process induced warpage in multitiled alumina substrates for large area MCM-D processing", *IEEE Transactions on Advanced Packaging* **23**, 436-445 (2000).
13. Dunne, R. C. and Sitaraman, S. K., "An integrated process modeling methodology and module for sequential multilayered substrate fabrication using a coupled cure-thermal-stress analysis approach", *IEEE Transactions on Electronics Packaging Manufacturing* **25**, 326-334 (2002).
14. Edgar, R. F., "The Fresnel diffraction images of periodic structures", *Opt. Acta* **16**, 281-287 (1969).
15. Fujimoto, J., "Determination of the vibrating phase by a time-averaged shadow moiré method", *Applied Optics* **21**, 4373-4376 (1982).
16. Goodman. J. W., *Introduction to Fourier Optics*, McGraw-Hill, New York (1968).
17. Guo, Y., Post, D., and Han, B., "Thick composites in compression: an experimental study of micromechanical behavior and smeared engineering properties," *Journal of Composite Materials* **26**, 1930-1944 (1993).

18. Guo, Y., “Applications of shadow moiré method in determination of thermal deformations in electronic packaging,” presented at the 1995 SEM Spring Conference, Grand Rapids, MI., June (1995).
19. Guralnick, S. A., Suen, E. S., and Zoruba, S., “Development of automated road inspection vehicle for nondestructive evaluation of road surface condition”, *Transportation Research Record* **1536**, 125-129 (1996)
20. Hahn, E. K., Carlsson, L. A. and Westerlind, B. S., “Edge-compression fixture for buckling studies of corrugated board panels”, *Experimental Mechanics* **32**, 252-258 (1992).
21. Han, B., “Higher sensitivity moiré interferometry for micromechanics studies”, *Optical Engineering* **31**, 1517-1526 (1992).
22. Han, B. and Post, D., “Immersion interferometer for microscopic moiré interferometry”, *Experimental Mechanics* **32**, 38-41 (1992).
23. Han, B., Guo, Y., and Choi, H. C., “Out-of-plane displacement measurement of printed circuit board by shadow moiré with variable sensitivity,” presented at the ASME International Electronics Packaging Conference, Binghampton, NY, Sept. (1993).
24. Han, B., “Interferometric methods with enhanced sensitivity by optical/digital fringe multiplication”, *Applied Optics* **32**, 4713-4718 (1993).
25. Han, B., Ifju, P., and Post, D., “Geometric moiré methods with enhanced sensitivity by optical/digital fringe multiplication”, *Experimental Mechanics* **33**, 195-200 (1993).

26. Han, B., "Micromechanical deformation analysis of β alloy titanium in elastic and elastic/plastic tension," *Experimental Mechanics* **36 (2)**, 120-126 (1996).

27. Han, B., Columbus, D., Wu, Z., and Lu., J, "Mechanical fringe shifting in moiré interferometry", *Experimental Techniques* **18 (1)**, 16-19 (1999).

28. Han, B., and Kunthong, P., "Micro-mechanical deformation analysis of surface laminar circuit in organic flip-chip package: an experimental stud", *ASME Journal of Electronic Packaging* **122**, 294-300 (2000).

29. Han, B., Wu, Z., and Cho, S., "Measurement of thermal expansion coefficient of flexible substrate by moiré interferometry," *Experimental Techniques* **25 (3)**, 22-25 (2001).

30. Han, C. W., Cho, S., and Han, B., "Transmission Microscopic Moiré Interferometry", *Proceedings of the SEM Annual Conference*, No. 194, Charlotte, NC, USA, June 2-4, (2003).

31. Ham, S.-J., and Lee, S.-B., "Measurement of creep and relaxation behaviors of wafer-level CSP assembly using moiré interferometry", *ASME Journal of Electronic Packaging* **125**, 282-288 (2003).

32. He, X., Zou, D., and Liu, S., "Phase-shifting analysis in moiré interferometry and its application in electronic packaging", *Optical Engineering* **37**, 1410-1419 (1998).

33. Hecht, E., *Optics*, 3rd ed. Addison-wesley (1998).

34. Hung, Y. Y., Liang, C. Y., Hovanesian, J. D., Durelli, A. J., "Time-averaged shadow-moiré method for studying vibrations", *Applied Optics* **16**, 1717-1719 (1977).

35. Janssens, J., Decraemer, W.F. and Vanhuyse, V.J., "Visibility depth of shadow-moiré fringes in function of extend of light source and aperture of recording system," *Optik* **71**, 45-51 (1985).

36. Jin, L., Kodera, Y., Yoshizawa, T., and Otani, Y., "Shadow moiré profilometry using the phase-shifting method", *Optical Engineering* **39**, 2119-2123 (2000).

37. Kafri, O. and Keren, E., "Fringe observation and depth of field in moiré analysis", *Applied Optics* **20**, 2885-2886 (1981).

38. Keren, E. and Kafri, O., "Diffraction effects in moiré deflectometry", *J. Opt. Soc. Am. A*, **2**, 111-120 (1985).

39. Kokidko, D., Gee, L., Chou, S. C., and Chiang, F. P., "Method for measuring transient out-of-plane deformation during impact", *International Journal of Impact Engineering* **19**, 127-133 (1997).

40. Kujawinska, M., Salbut, L., and Patorski, K., "Three-channel phase stepped system for moiré interferometry", *Applied Optics* **30**, 1633-1635 (1991).

41. Ladak, H. M., Decraemer, W. F., Dirckx, J. J. J., and Funnell, W. R. J., "Systematic erros in small deformations measured by use of shadow-moiré topography", *Applied Optics* **39**, 3266-3275 (2000).

42. Liao, J. E. A. and Voloshin, A. S., "Enhancement of the shadow-moiré method through digital image processing", *Experimental Mechanics* **33**, 59-63 (1993).

43. Liu, H., Cartwright, A. N., and Basaran, C., "Sensitivity improvement in phase-shifted moiré interferometry using 1-D continuous wavelet transform image processing", *Optical Engineering* **42**, 2646-2652 (2003).

44. Liu, H., Cartwright, A. N., and Basaran, C., "Experimental verification of improvement of phase shifting moiré interferometry using wavelet-based image processing", *Optical Engineering* **43**, 1206-1214 (2004).

45. Livnat, A., and Post, D., "The governing equations for moiré interferometry and their identity to equations of geometrical moiré", *Experimental Mechanics* **25**, 360-366 (1985).

46. Maji, A. K. and Starnes, M. A., "Shape measurement and control of deployable membrane structures", *Experimental Mechanics* **40**, 154-159 (2000).

47. Mauvoisin, G., Bremand, F., and Lagarde, A., "Three-dimensional shape reconstruction by phase-shifting shadow moiré", *Applied Optics* **33**, 2163-2169 (1994).

48. Maystre, D., "Rigorous vector theories of diffraction gratings", in *Progress in optics Vol. XXI*, E. Wolf, eds.(North-Holland, Amsterdam), 1-68 (1989).

49. McKelvie, J., "On moiré interferometry and the level of detail that it may reveal legitimately", *Optics and Lasers in Engineering* **12**, 81-99 (1990).

50. Meadows, D. M., Johnson, W. O., and Allen, J. B., "Generation of surface contours by moiré pattern", *Applied Optics* **9**, 942-947 (1970).

51. Miller, M. R., Mohammed, I., Dai, X., Jiang, N., and Ho, P. S., "Analysis of flip chip packages using high resolution moiré interferometry", *Proceedings of 49th Electronic Components and Technology Conference*, 979-986 (1999).

52. Patorski, K., "The self-imaging phenomenon and its applications", in *Progress in optics Vol. XXVII*, E. Wolf, eds.(North-Holland, Amsterdam), 1-108 (1989).

53. Petriccione, G. J., Ume, I. C., "Warpage studies of HDI test vehicles during various thermal profiling", *IEEE Transactions on Advanced Packaging* **22**, 624-637 (1999).

54. Polsky, Y., Sutherlin, W., and Ume. I. C., "A comparison of PWB warpage due to simulated infrared and wave soldering processes", *IEEE Transactions on Electronics Packaging Manufacturing* **23**, 191-199 (2000).

55. Post, D., Han, B., and Ifju, P., *High Sensitivity Moiré: Experimental Analysis for Mechanics and Materials*, Springer-Verlag, New York (1994).

56. Post, D., Han, B., and Ifju, P., "Moiré methods for engineering and science – moiré interferometry and shadow moiré, Chap. 7" in *Photomechanics*, P. K. Rastogi, eds., Springer-Verlag, New York (2000).

57. Qing, X., Qin, Y., and Dai, F., "Optical fringe multiplication in moiré interferometry", *Applied Optics* **34**, 7291-7294 (1995).

58. Quan, C., Fu, Y., Tay, C. J., "Determination of surface contour by temporal analysis of shadow moiré fringes", *Optics Communications* **230**, 23-33 (2004).

59. Rao, D. B., and Prakash, M., "Effect of substrate warpage on the second level assembly of advanced plastic ball grid array (PBGA) packages", *21st IEEE/CPMT International Electronics Manufacturing Technology Symposium*, 439-446 (1997).

60. Rayleigh, L., *The London, Edinburgh, and Dublin Philosophical Magazine and Journal of Science, Series5*, **11**, 196, (1881).

61. Salbut, L. and Patorski, K., "Polarization phase shifting method for moire interferometry and flatness testing", *Applied Optics* **29**, 1471-1473 (1990).

62. Shield, T. W. and Kim, K.-S., "Diffraction theory of optical interference moiré and a device for production of variable virtual reference gratings: a moiré microscope," *Experimental Mechanics* **31**, 126-134 (1991).

63. Stellrecht, E., Han, B., and Pecht, M., "Measurement of the hygroscopic swelling coefficient in mold compounds using moiré interferometry," *Experimental Techniques* **27 (4)**, 40-44 (2003).

64. Stiteler, M. R., Ume, I. C., and Leutz, B., "In-process board warpage measurement in a lab scale wave soldering oven", *IEEE Transaction on Components, Packaging, and Manufacturing Technology-Part A* **19**, 562-569 (1996).

65. Sutherlin, W., Polsky, Y., and Ume, I. C., "A relative comparison of PWB warpage due to simulated infrared and wave soldering processes", *Proceedings of 48th Electronic Components and Technology Conference*, 807-815 (1998).

66. Takasaki, H., " Moiré Topography", *Applied Optics* **9**, 1467-1472 (1970).

67. Talbot, H.F., *The London and Edinburgh Philosophical Magazine and Journal of Science, Series3*, **9**, 401, (1836).

68. Tay, C. J., Quen, C., Fu, Y., and Huang, Y., "Instantaneous velocity displacement and contour measurement by use of shadow moiré and temporal wavelet analysis", *Applied Optics* **43**, 4164-4171 (2004).

69. Testorf, M., Jahns, J., Khilo, N., and Goncharenko, A., "Talbot effect for oblique angle of light propagation," *Optics Communications* **129**, 167-172 (1996).

70. Tuttle, M.E., "Demonstrating moiré fringes using gratings produced with a laser printer", *Experimental Techniques* **21**, 19-22 (Sep.-Oct., 1997).

71. Tuttle, M.E., Singhatanadgid, P., and Hinds, G., "Buckling of composite panels subjected to biaxial loading", *Experimental Mechanics* **39**, 191-201 (1999).

72. Verma. K., Columbus. D., Han. B., and Chandran. B., "Real-time warpage measurement of electronic components with variable sensitivity", *1998. 48th IEEE Electronic Components and Technology Conference*, 975-980 (1998).

73. Verma. K., Columbus. D., and Han. B. "Development of real time/variable sensitivity warpage measurement technique and its application to plastic ball grid array package", *IEEE Transaction on Electronics Packaging Manufacturing* **22**, 63-70 (1999).

74. Verma. K., Park. S. B., and Han. B. "On the design parameters of flip-chip PBGA package assembly for optimum solder ball reliability", *IEEE Transaction on Components and Packaging Technologies* **24**, 300-307 (2001).

75. Vrinceanu, I. D., and Danyluk, S., "Measurement of residual stress in single crystal silicon wafers", *Proceedings of 8th International Symposium on Advanced Packaging Materials*, 297-301 (2002).

76. Wang. Y., and Hassell. P., "Measurement of thermally induced warpage of BGA packages/substrates using phase-stepping shadow moiré", *Proceedings of the 1997 1st Electronic Packaging Technology Conference*, 283-289 (1997).

77. Wang, Z., "Development and application of computer-aided fringe analysis", Ph.D. dissertation, U. of Maryland College Park (2003).

78. Wei, S., Wu, S., Kao, I., and Chiang, F.P., "Measurement of wafer surface using shadow moiré technique with Talbot effect", *ASME J. Electronic Packaging* **120**, 166-170 (1998).

79. Wu, J. C. L., Shine, H., Wu, S., Hung, M., and Lee, J. J., "Study of rapid cure BGA mold compound on warpage with shadow moiré", *1999 Proceedings of 49th Electronic Components and Technology Conference*, 708-713 (1999).

80. Wu, S.X., Lu, H., Yang, T., and Yeh, C., "Process induced warpage and residual stress in populated ball grid array substrate panel", *Proceedings. 1998 4th International Symposium on Advanced Packaging Materials*, 151-152 (1998).

81. Yeh, C. P., Banerjee, K., Martin, T., Umeagukwu, C., Fulton, R., Stafford, J., Wyatt, K., "Experimental and analytical investigation of thermally induced warpage for printed wiring boards", *Proceedings of 41st Electronic Components and Technology Conference*, 382-387 (1991).

82. Yeh, C., Ume, C., Fulton, R. E., Wyatt, K. W., and Stafford, J. W., "Correlation of analytical and experimental approaches to determine thermally induced PWB warpage", *IEEE Transactions on Components, Hybrids, and Manufacturing Technology* **16**, 986-995 (1993).

83. Yoshizawa, T. and Tomisawa, T., "Shadow moiré topography by means of the phase-shift method", *Optical Engineering* **32**, 1668-1674 (1993).

84. Zhang, J., Ding, H., Baldwin, D.F. and Ume, I. C., "Characterization of in-process substrate warpage of underfilled flip chip assembly", *2003 IEEE/CPMT/SEMI International Electronics Manufacturing Technology Symposium*, 291-297 (2003).

85. Zwemer, D., Bajaj, M., Peak, R., Thurman, T., Brady, K., McCarron, S., Spradling, A., Dickerson, M., Klein, L., Liutkus, G., Messina, J., "PWB warpage analysis and verification using an AP210 standards-based engineering framework and shadow moiré", *Proceedings of the 5th International Conference on Thermal*

and Mechanical Simulation and Experiments in Microelectronics and Microsystems, EuroSimE 2004., 121-131 (2004).